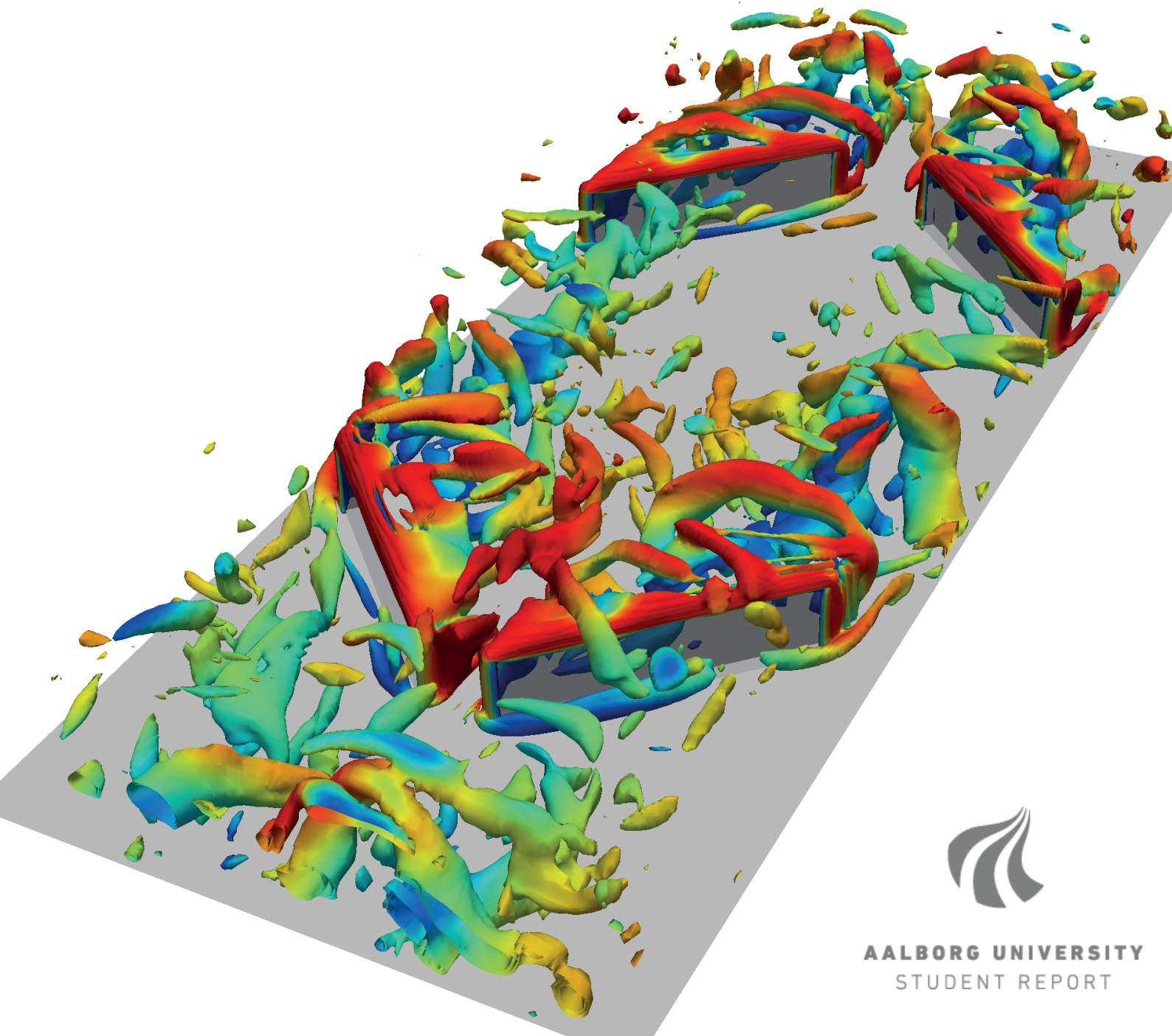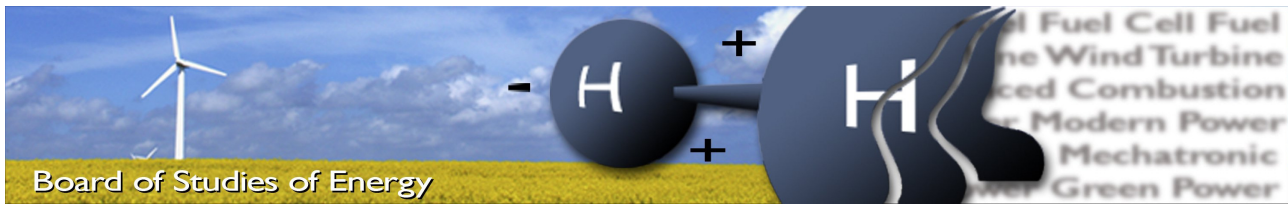# Numerical Investigation of Flow Structures and Their Impact on Heat Transfer Performance in a Staggered Arrangement of Rectangular Winglet Pair Vortex Generators in a Fully Developed Channel Flow

Allan Bjerg and Kristian Christoffersen
Master Thesis Project, June 2018
Thermal Energy and Process Engineering

The front page image show the computational domain with at staggered arrangement of rectangular winglet pairs. The structures around the winglets are iso-contours of the swirling strength, λ, coloured by the magnitude of the instantaneous velocity.

Title:	Numerical Investigation of Flow Structures and Their Impact on Heat Transfer Performance in a Staggered Arrangement of Rectangular Winglet Pair Vortex Generators in a Fully Developed Channel Flow.
Semester:	4th semester of Thermal Energy and Process Engineering
Semester theme:	Master Thesis
Project period:	02/02/2018 to 01/06/2018
ECTS:	30
Supervisor:	Henrik Sørensen & Jakob Hærvig
Project group:	TEPE4-1005

Allan Bjerg

Kristian Christoffersen

Pages, total:	108 consisting of:
	86 pages report
	22 pages formalities
	and blank pages
Appendices:	A - F

SYNOPSIS:

Heat exchangers are used in many practical applications throughout the world. For applications involving liquid-to-gas heat transfer, the gas-side accounts for the vast majority of the thermal resistance. One way of improving the heat transfer is by the use of vortex generators (VGs) such as winglets. VGs generate vortices that interact with the thermal boundary layer and thereby enhance the heat transfer. The present work investigates how variations in winglet height and longitudinal pitch distance affect the flow phenomena and resulting heat transfer and pressure loss for rectangular winglet pair VGs in a staggered periodic arrangement. A Large Eddy Simulation (LES) model to simulate periodic flow and heat transfer is developed for the numerical investigations. To validate the LES model, an experimental setup is developed to facilitate Laser Doppler Anemometry (LDA) measurements. The LDA measurements and LES simulations show good correspondence with a mean deviation of $\approx$ 5 %. The numerical investigations prove the highest performance at a smaller winglet height and larger longitudinal pitch distance, which is attributed to the fact that the generated vortices in this configuration have a good interaction with the thermal boundary layer without causing a significant pressure loss.

By signing this document, each member of the group confirms that all group members have participated in the project work, and thereby all members are collectively liable for the contents of the project. Furthermore, all group members confirm that the project does not include plagiarism.

Executive Summary

In many practical applications throughout the world such as airconditioning, electronics cooling and refrigeration, heat exchangers are of great importance. In general, heat exchangers involving liquid-to-gas heat transfer, the gas-side accounts for the majority of the thermal resistance. Therefore, much work has been devoted into improving the gas-side heat transfer. One way of doing this is by inserting vortex generators (VGs) into the flow field. These VGs generate vortices that interact with the thermal boundary layer and thereby enhance the heat transfer. Due to their interaction with the flow field, the heat transfer enhancement comes with a pressure penalty. An example of the vortices generated by a rectangular winglet pair VG is shown in Figure 1.
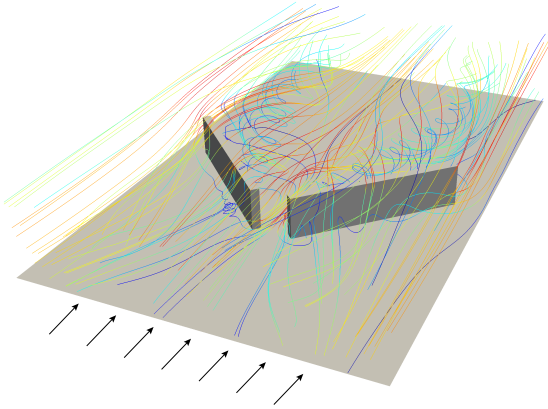

Figure 1. Example of vortices generated by a winglet pair vortex generator. The longitudinal vortices are the main contributors to heat transfer enhancement.
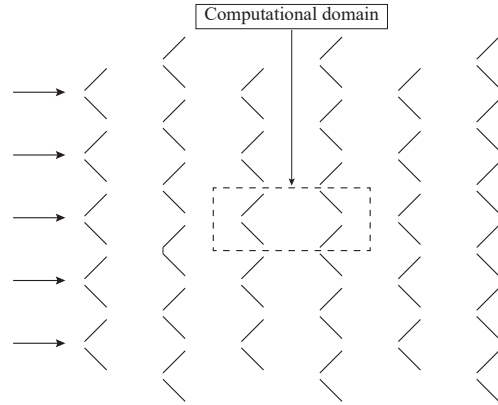
Figure 2. Staggered periodic arrangement of rectangular winglet pairs. The dashed rectangle illustrates the computational domain. L_p is the longitudinal pitch distance.

The winglets can be made in various geometrical shapes and be placed in different arrangements which means that the heat transfer enhancement is very dependent on the specific setup. In the present work, the performance of rectangular winglets in a periodic staggered arrangement is numerically investigated by the use of Large Eddy Simulation (LES). The LES setup is developed to account for both the flow- and temperature field and the simulations are conducted in OpenFOAM. To simulate the periodic staggered arrangement, periodic boundary conditions are deployed on the computational domain which reduces the size of the domain to include only two winglets pairs as shown in Figure 2. To account for periodic flow and heat transfer, additional terms are added to the governing equations which divides the pressure and temperature into a periodic a non-periodic term. This is shown equations (1) and (2), where the second terms on the right hand sides are the periodic terms (Patankar et al., 1977).

$$p\left(x, y\right) = -\beta x + \hat{p}\left(x, y\right) \tag{1}$$

$$T\left(x, y\right) = \gamma x + \hat{T}\left(x, y\right) \tag{2}$$

The LES setup is experimentally validated using velocity measurements on a test channel in a wind tunnel. The measurements are made using the optical measurement method Laser Doppler Anemometry. The experimental results show good correspondence with the LES simulations with a mean deviation of ≈ 5 %. A comparison of velocity and turbulence intensity profiles from the LES simulations and the LDA measurements are shown in Figure 3.
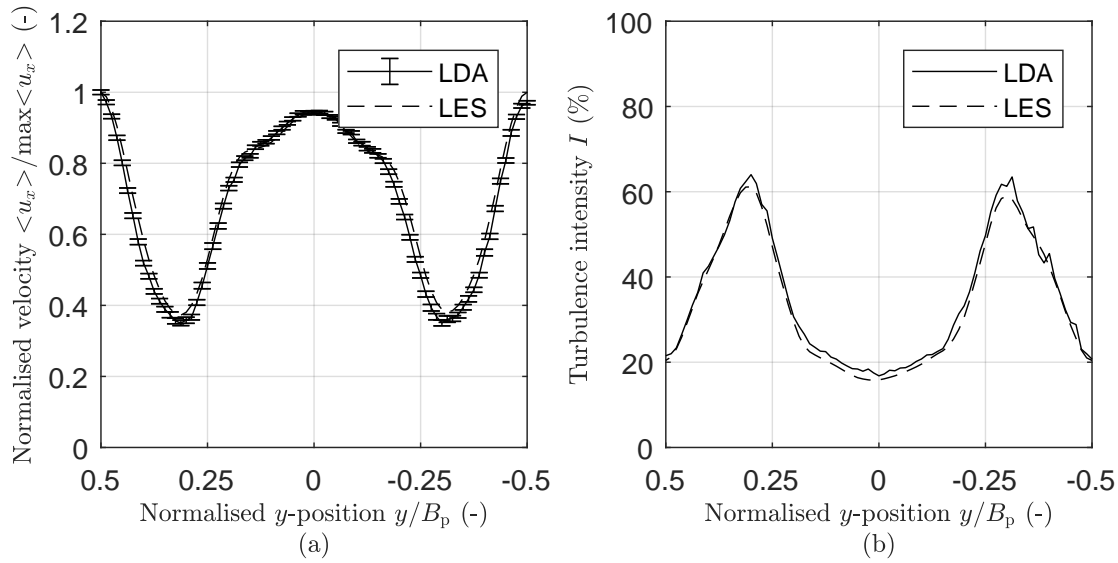

Figure 3. (a) Comparison of velocity profiles from the LES simulations and the LDA measurements. The error bars for the LDA measurements are based on a 95 % confidence interval. (b) Comparison of turbulence intensity profiles from the LES simulation and the LDA measurements. Both comparisons are made for a normalised z-position of $z/H = 0.6$.

The validated LES setup is used for a parametric study where the impact of varying the longitudinal pitch distance and the winglet height is investigated. The Nusselt number, Nu, and loss coefficient, f, are used as measures of the heat transfer and the pressure loss. The parameters are based on the channel height, H, and are given in quation (3).

$$\text{Nu} = -\frac{\mathrm{d}T}{\mathrm{d}n}\frac{H}{\Delta T} \qquad\qquad f = \frac{H}{0.5\rho u_{\text{bulk}}^2}\frac{\mathrm{d}P}{\mathrm{d}x} \tag{3}$$

The results are compared to the results for a simulation of a channel without winglets given as Nu_0 and f_0. To evaluate the heat transfer enhancement relative to the increase in pressure loss a performance parameter, η, based on equal pumping power is used. The performance parameter is given in Equation (4).

$$\eta = \frac{\text{Nu}/\text{Nu}_0}{(f/f_0)^{1/3}} \tag{4}$$

The performance factor for the different simulations are summarised in the contour shown in Figure 4.
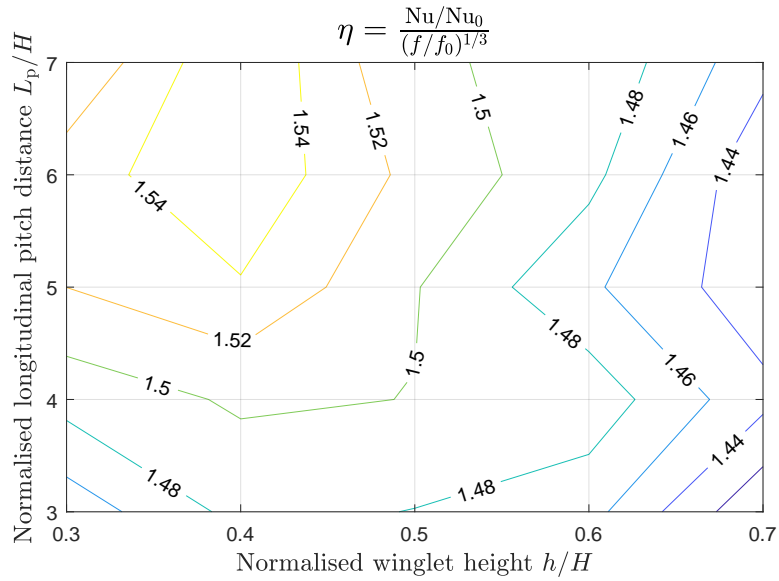
Figure 4. Heat transfer performance as function of normalised winglet height, h/H, and normalised longitudinal pitch distance, L_p/H.

The investigations proved the highest performance at a smaller winglet height and larger longitudinal pitch distance, which was attributed to the fact that the generated vortices in this configuration have a good interaction with the thermal boundary layer without causing a significant pressure loss.

Preface

This Master's Thesis concludes the 4th semester of the M.Sc. in *Thermal Energy and Process Engineering* at the *Department of Energy Technology* at *Aalborg University*. The Thesis was conducted in the period from February 2nd to June 1st 2018. The project concerns a numerical investigation of flow phenomena and resulting heat transfer and pressure loss due to a staggered arrangement of vortex generators in a fully developed channel flow.

Readers guide

Available on page xi-xiii is the *Nomenclature* which serves as an overview and explanation of the general abbreviations, subscripts and symbols used throughout this project. Abbreviations are written the first time they are presented in every chapter after which the abbreviation is used. Variables are written in italic whereas units are written as non-italic. For example, s is seconds and s is standard deviation. The x, y, z Cartesian coordinate system is used throughout the project.

Each chapter is initiated with an introduction in italic which explains the content of the chapter. Figures, tables and equations are numbered according to their chronological placement throughout the project. This means that Figure 3.1 is the first figure of Chapter 3. References are made using the *Harvard method* signifying that any source is marked with the surname of the author followed by the year of publication. If the given reference has more than three authors, the surname of the first author is presented followed by et al. and the year of publication. Additional information about the references can be found in the reference list in the back of the project.

The appendices in the back of the report are denoted as Appendix A, Appendix B etc. These contain relevant information to different parts of the project and are referred to appropriately. The enclosures are attached to the project and contain the mesh generation MATLAB code, OpenFOAM solver and setup and SolidWorks drawings of the test channel.

Acknowledgments

We would like to thank the department workshop under direction of Assistant Engineer Jan Christiansen for the fabrication of our test channel. Furthermore, we greatly appreciate the opportunity to conduct simulations on the ABACUS 2.0 supercomputer at *The University of Southern Denmark* in Odense.

Nomenclature

General abbreviations	Description
AT	Arrival time
BL	Boundary layer
CFD	Computational Fluid Dynamics
DNS	Direct Numerical Simulation
HWA	Hot Wire Anemometry
IA	Interrogation area
LDA	Laser Doppler Anemometry
LES	Large Eddy Simulation
NS	Navier-Stokes
PIV	Particle Image Velocimetry
PISO	Pressure-Implicit with Splitting of Operators
RANS	Reynolds-Averaged Navier-Stokes
RMS	Root Mean Square
SGS	Subgrid-Scale
VG	Vortex generator
WALE	Wall-Adapting Local Eddy-viscosity

Subscripts	Description
0	Reference
i	$x-, y-, z-$component and i'th entry
j	$x-, y-, z-$component and j'th entry
ref	Reference
sim	Simulation
x	x-direction
y	y-direction
z	z-direction

Symbols	Description	Unit
A	Area	m^2
B_p	Transverse pitch distance	m
C	Asymtotic range of convergence	-
CFL	Courant number	-
c_p	Specific heat capacity at constant pressure	J/kg-K
D_h	Hydraulic diameter	m
d_P	Mean particle diameter	m
e	Winglet tip distance	m
E	Energy	J/kg
f	Loss coefficient	-
f'	Fluctuating part of loss coefficient	-
F_s	Safety factor	-
G	Cell expansion ratio	-
GCI	Grid Convergence Index	-
h	Winglet height	m
H	Channel height	m
k	Thermal conductivity	W/m-K
l	Winglet length	m
L	Length of block	m
L_d	Computational domain length	m
L_p	Longitudinal pitch distance	m
M	Total number of inlet faces	-
n	Wall normal distance	m
n	Number of samples	-
N	Number of cells	-
N	Total number of wall faces	-
N_{cl}	Cell density	m^{-1}
Nu	Nusselt number	-
Nu'	Fluctuating part of Nusselt number	-
p	Order of convergence	-
p	Pressure	m^2/s^2
P	Global pressure	m^2/s^2
$\bar{p}$	Filtered pressure	m^2/s^2
$\hat{p}$	Periodic pressure	m^2/s^2
Pr	Prandtl number	-
Pr_t	Turbulent Prandtl number	-
$\dot{q}$	Wall heat flux	W/m^2
r	Grid refinement ratio	-
Re	Reynolds number	-
s	Sample standard deviation	-
t	Time	s
St	Stokes number	-
T	Temperature	K
$\bar{T}$	Filtered temperature	K
$\hat{T}$	Periodic temperature	K

$<T>$	Mean temperature	K
T_p	Flow through time of one period	s
t_w	Winglet thickness	m
t^*	Normalised flow through time	-
u	Velocity	m/s
$\bar{u}$	Filtered velocity	m/s
$<u>$	Mean velocity	m/s
$<x>$	Sample mean	-
Δy_1	Size of wall adjacent cell	m
x_v	Distance from channel edge to winglet leading edge	m
$<\Delta y>$	Mean cell size	m
y^+	Dimensionless wall normal distance	-
$z_{\alpha/2}$	Critical value of normal distribution	-

Greek symbols	Description	Unit
α	Angle of attack	$^\circ$
β	Streamwise pressure gradient	m/s^2
γ	Streamwise temperature gradient	K/m
δ	Kronecker delta	-
Δ	Difference	-
ϵ	Relative error	-
η	Performance parameter	-
λ	Swirling strength	s^{-1}
μ	Dynamic viscosity	kg/m-s
ν	Kinematic viscosity	m^2/s
ν_t	Turbulent kinematic viscosity	m^2/s
ρ	Density	kg/m^3
ρ	Autocorrelation function coefficient	-
τ_ℓ	Integral time scale	s
τ_F	Characteristic flow time	s
τ_P	Particle response time	s

Contents

CHAPTER 1

INTRODUCTION

Heat exchangers are one of the most widely used thermal systems in the world and are used in industrial as well as commercial and domestic applications. Some widespread examples are airconditioning, refrigeration, car radiators, electronics cooling and aerospace applications. In recent decades the energy usage worldwide has been increasing due to the increase in population, industrialisation and urbanisation (Alam and Kim, 2018). The ever increasing demand for efficiency improvements and striving to get more for less, e.g. heat exchangers with smaller area to volume density, has caused research attention towards enhancing the performance of heat exchangers. Different methods can be used to enhance heat transfer and are usually split into two categories; active and passive methods. The difference between active and passive methods is that active methods require external power such as electric fields and mechanical devices, whereas passive methods do not require external power but make use of special geometries or fluid additives. The modifications to the flow induced by either of the two methods are also split into two categories; main flow manipulation and secondary flow enhancement.

Main flow manipulation includes altering of the gross characteristics of the flow through e.g. geometric changes and pressure variations whereas secondary flow enhancement includes introduction of local secondary flow structures such as vortices. Both phenomena can be introduced to the flow actively and passively. The main flow can actively be manipulated by flow pulsations and passively by furrowed channels. Secondary flows can actively be introduced by using electrohydrodynamics to disturb the flow using an electric field and passively be introduced by using surface protuberances and by inserting wings or winglets (Jacobi and Shah, 1995; Alam and Kim, 2018). It has to be kept in mind that these phenomena may be difficult to distinguish between and that they in some cases are coupled or interfere. The examples given above are made to get an idea of the differences but are not necessarily isolated cases.

As passive methods do not require external power and are cheap, reliable and easily applicable to existing as well as new systems, passive methods for heat transfer enhancement are popular across industries (Alam and Kim, 2018). Much attention has been devoted to the performance of liquid-to-air, two-phase-to-air and air-to-air heat exchangers. An example of an air-to-air plate-fin heat exchanger is shown in Figure 1.1.
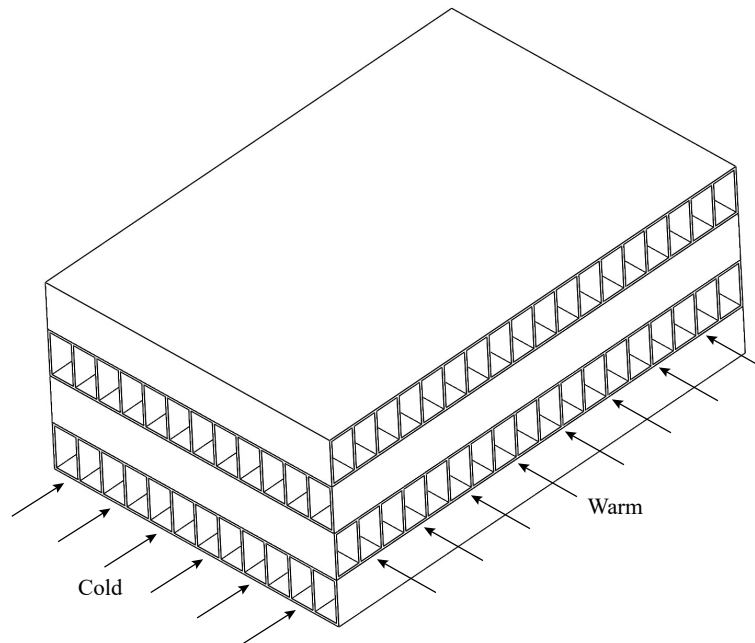
Figure 1.1. Example of an air-to-air plate-fin heat exchanger. This type of heat exchanger is for example used in the environmental control system of an aircraft.

In general, the air-side heat transfer limits the thermal performance due to its high thermal resistance compared to e.g. water. For example, the air side can account for 95 % of the thermal resistance in a condenser for typical refrigeration applications (Admiraal and Bullard, 1995). Similar examples could be drawn from utility, automotive, aerospace and process industries (Jacobi and Shah, 1998). The advantages of passive methods and the attention on heat exchangers involving airflow have lead to an increasing research focus on vortex generators (VGs) such as fins, ribs, twisted tapes, wings and winglets for enhancing heat transfer on the air-side of the heat exchangers (Alam and Kim, 2018; Sohankar and Davidson, 2001).

Vortex generators are special surfaces inserted into the flow field to generate vortices by swirling and destabilising the flow. These vortices have a tendency to last for a long period of time and to have small cores, therefore allowing an influence on heat transfer over long and narrow regions (Fiebig, 1998). The vortex generators can generate longitudinal or transverse vortices depending on their angle of attack and geometry. The transverse vortices, also called spanwise vortices, are perpendicular to the flow field and are generated from flow separation and unstable shear layers. The flow due to transverse vortices may stay two-dimensional meaning that the transverse vortex is stationary with respect to the streamwise direction. The longitudinal vortices, also called streamwise vortices, are induced by the vortex generators which causes the flow to swirl around the main flow axis. These vortices always produce three-dimensional flow. In this regard Sohankar and Davidson (2001) states that longitudinal vortices generally are more efficient for heat transfer enhancement than transverse vortices. Furthermore, according to Fiebig (1998), where rectangular and triangular winglet VGs in channel flows were studied, longitudinal vortices enhance heat transfer locally and globally in steady flow, while the global enhancement from transverse vortices is negligible. It has to be kept in mind that the heat transfer enhancement using VGs comes with a cost in terms of pressure loss.

Vortex generators come in many different shapes depending on the application. It is evident from the comprehensive review of experimental and numerical activities on heat transfer enhancement using VGs conducted by Awais and Bhuiyan (2018) that wing and winglet VGs have been widely investigated over the years due to their performance, applicability and simple design and manufacturing. The four most common wing- and winglet type VGs are shown in Figure 1.2.

Delta wing

Rectangular wing
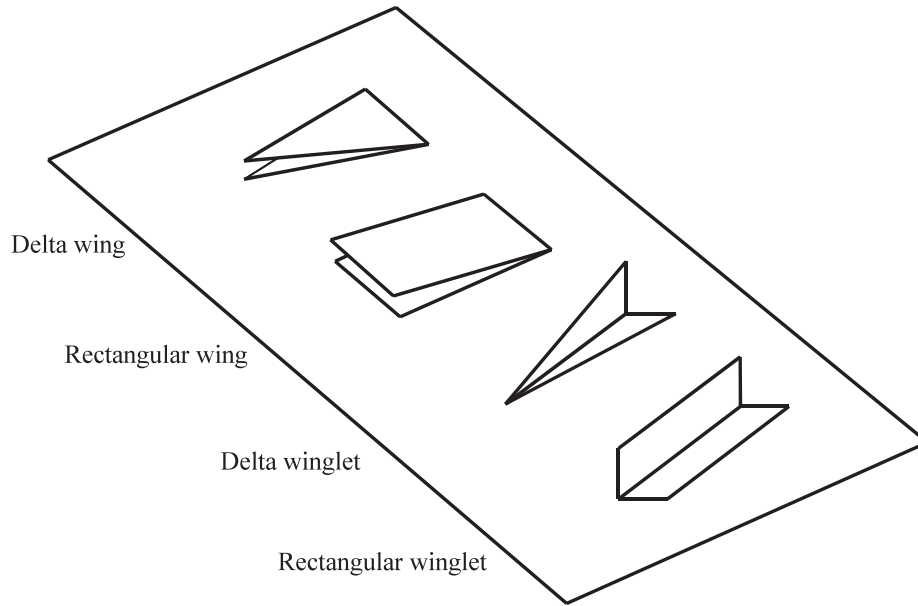
Delta winglet

Rectangular winglet

Figure 1.2. Schematic of the four most common wing- and winglet-type vortex generators.

Based on these four common VG geometries a literature study is conducted focusing on heat transfer enhancement and the flow phenomena that causes it.

1.1 Existing work on vortex generators

In Appendix A the literature study is presented where the field of investigation, the methods used and the main findings are summed up for each of the chosen articles. Figures 1.3 and 1.4 presents the most widely investigated arrangement of VGs in a channel flow.
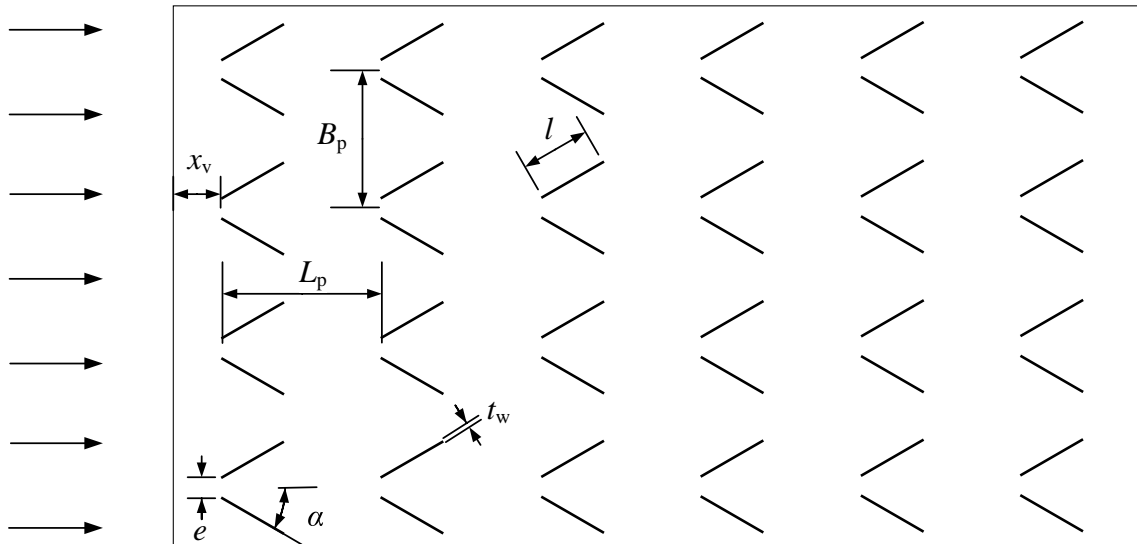

Figure 1.3. Top view of a common flow down configuration of in-line rectangular winglet pairs in a channel. B_p = transverse pitch distance, e = winglet tip distance, L_p = longitudinal pitch distance, t_w = winglet thickness, x_v = distance from channel edge to winglet leading edge, l = winglet length and α = angle of attack.
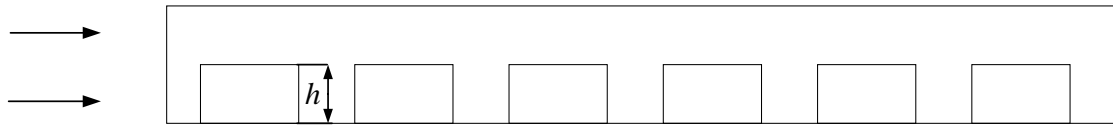
Figure 1.4. Side view of a common flow down configuration of in-line rectangular winglet pairs in a channel. h = winglet height.

From the literature study it is evident that a significant amount of numerical and experimental effort has been devoted to heat transfer enhancement and relating flow phenomena due to the use of the VGs presented in Figure 1.2. However, very limited attention has been devoted towards the staggered arrangement of VGs with the articles by Chen et al. (2000) and Sinha et al. (2013) being the only two found to cover this arrangement. In both studies two rows of staggered delta winglets were investigated. Chen et al. (2000) studied a common flow down arrangement and Sinha et al. (2013) studied a more uncommon arrangement with the winglets having 0 angle of attack relative to the main flow direction. Both studies found that the staggered arrangement performed better in terms of both heat transfer enhancement and pressure loss compared to an in-line configuration.

Beside the aforementioned, common findings for all the studied articles are that VGs do enhance heat transfer and that the enhancement comes with a penalty in the form of a pressure loss. The reason why VGs enhance heat transfer is because they induce different vortex structures in their downstream region. These vortices disrupts the thermal boundary layer and enhance mass transfer across regions with high temperature gradients which leads to a higher heat transfer. Since the enhancement comes with a pressure loss, most authors quantifies the performance of different VG configurations as a relationship between heat transfer enhancement and pressure loss.

To get an overview of the findings in the literature study, concluding statements based on recurring results and tendencies are presented below:

- Winglets are more efficient than wings for heat transfer enhancement.
- The performance of rectangular winglets and delta winglets are similar.
- It is not advantageous to implement vortex generators into an already turbulent flows since the increase in heat transfer is very low compared to the increase in pressure loss.
- Heat transfer enhancement and pressure loss increase with Reynolds number and angle of attack.
- Several different vortex structures are formed downstream of the vortex generators. Longitudinal vortices are most important for the overall heat transfer enhancement.
- Configurations creating counter-rotating vortices e.g. common flow up or common flow down configurations, are more effective for heat transfer enhancement.
- The strength of the generated vortices increase with Reynolds number and decrease in the streamwise direction.
- The most common periodic arrangement is in-line rows of vortex generators.

No apparent answer for the most efficient flow- or geometrical configurations of VGs are found. It is evident that various parameters such as VG height, length, thickness, arrangement, manufacturing technique etc. as well as combinations hereof affect the performance of the VGs differently. An example is drawn from the conclusions of Chen et al. (2000) and Akcayoglu (2011), where not only the winglet configuration but also the resulting distance to the wall affect the performance.

CHAPTER 2

PROBLEM STATEMENT

The literature study proved that a significant amount of work has been devoted to investigating the impact of vortex generators on heat transfer enhancement and the associated flow phenomena in channel flows. However, the amount of work devoted to the staggered arrangement of vortex generators is found to be insufficient, considering that the investigations on the staggered arrangement found this arrangement more efficient than its in-line counterpart. Therefore, this study aims to investigate the staggered arrangement of vortex generators. Several comparisons between the four considered wing- and winglet type vortex generators have been conducted, proving that winglets are superior to wings. The difference in performance between rectangular and delta winglets proved minor for which reason rectangular winglets are studied due to their simpler geometry. Based on this geometry, it is desired to conduct a parametric study to investigate how variations of the winglet height and longitudinal pitch distance affect the flow and how these flow alterations affect the heat transfer and pressure loss in the channel. Computational Fluid Dynamics (CFD) is used to model the flow and heat transfer since it provides large flexibility when conducting a parametric study. It is desired to validate the CFD simulations with an experiment to determine how closely the simulations resemble real life phenomena. This leads to the problem statement:

> **How does the winglet height and longitudinal pitch distance affect the flow and thereby the heat transfer and pressure loss in a fully developed channel flow with a staggered arrangement of rectangular winglet pairs?**

2.1 Problem solving strategy

Before the parametric study can be conducted, several subtasks must be completed. The subtasks are divided into two overall categories; a numerical and an experimental approach. These are combined to validate the numerical setup after which the parametric study can be carried out.

The numerical approach analyses the flow in the channel by the use of CFD-simulations. The simulations are conducted in OpenFOAM which is an open source CFD software. To develop a CFD setup for the present study, the following tasks are addressed:

- Determination of modelling approach suitable for the present study including turbulence modelling, discretization and boundary conditions.
- Development of structured computational grid suitable for the OpenFOAM utility blockMesh.
- Determination of appropriate solution parameters.

- Grid convergence study including mesh refinement.

The first task is to identify which of the three main modelling approaches including Direct Numerical Simulation, Large Eddy Simulation and Reynolds-Averaged Navier-Stokes that is most suitable for the case at hand. Furthermore, appropriate discretization schemes, boundary conditions and turbulence model are determined. The second task concerns the development of a code to generate a structured computational grid suitable for the OpenFOAM utility blockMesh. MATLAB is used as the environment in which the model is developed. The code must be set up to facilitate geometrical changes which are necessary when performing the mesh refinement and parametric study. The third task is to identify appropriate solution parameters which can be used for the comparison of the different configurations in the parametric study. Attention is devoted towards dimensionless parameters due to their comparability and reproduce ability. The fourth task is to conduct a grid convergence study to determine at which mesh size the solution approaches grid independency. The procedure for the grid convergence study is to develop a base mesh and then double the number of cells until a grid independent solution is found. This results in a benchmark CFD setup ready for validation.

The purpose of the experiment is to validate how closely the CFD setup resembles real life flow phenomena. No existing experimental setup exists for the case at hand for which reason a new setup must be designed to perform the validation. The experiments are conducted a in wind tunnel. In order to design the experiment, the following tasks are addressed:

- Determination of measurement method.
- Design of test channel.
- Experimental procedure and considerations.

The first task is to determine which measurement method that suits the case at hand the best. In recent years, significant progress has been made within optical measurement methods such as Particle Image Velocimetry and Laser Doppler Anemometry. These are preferred due to their significantly lower influence on the flow compared to classic measurement methods. The second task is to design a test channel that is suitable for the chosen measurement method. Furthermore, it must be designed to comply with the physical constraints of the wind tunnel in which the experiments are conducted. The third task concerns the experimental procedure and considerations made to assure comparability between the simulations and the experiment. The experimental procedure includes the experimental setup as well as the apparatus and settings used during measurements. The experimental considerations include statistical independence of the measured data, seeding considerations and experimental uncertainties. With this, the validation experiments can be conducted.

Combining the numerical and experimental approach leads to an investigation of the validity of the CFD setup determining how accurately it resembles real life phenomena. Following the validation, the parametric study is conducted. The structure of the report is visually shown in Figure 2.1.
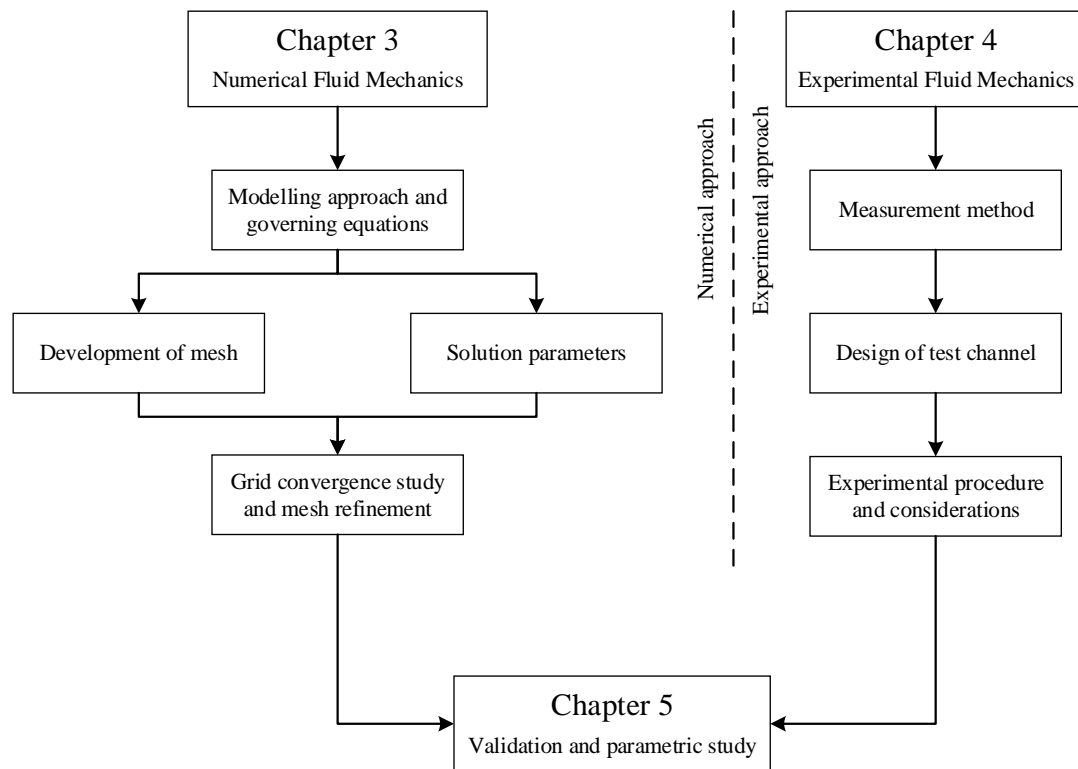
Figure 2.1. Visual overview of the report. The dashed line highlights the two different parts i.e. the numerical approach and experimental approach which are combined in a validation of the numerical approach and parametric study.

CHAPTER 3

NUMERICAL FLUID MECHANICS

In this chapter, the numerical method and computational setup used for simulation of the fluid flow and heat transfer are described. The first part of the chapter comprises of considerations regarding the simulation setup including governing equations and modelling approach. The second part is a description of the considerations that are taken into account when generating the mesh. This is followed by a verification of the Computational Fluid Dynamics (CFD) code that is implemented to account for heat transfer. Finally, a grid convergence study is conducted in order to ensure a mesh independent solution followed by the design of the parametric study.

3.1 Navier-Stokes equations

The governing equations describing the flow of a Newtonian fluid are the Navier-Stokes (NS) equations. The NS equations include the continuity equation, the three momentum equations, the energy equation and the equations of state. For an incompressible flow, the NS equations for continuity, momentum and energy, neglecting body forces and viscous dissipation are given in equations (3.1)-(3.3) in Cartesian tensor form as:

$$\frac{\partial u_i}{\partial x_i} = 0 \tag{3.1}$$

$$\frac{\partial u_i}{\partial t} + u_j \frac{\partial u_i}{\partial x_j} = -\frac{1}{\rho}\frac{\partial p}{\partial x_i} + \nu \frac{\partial^2 u_i}{\partial x_j \partial x_j} \tag{3.2}$$

$$\frac{\partial E}{\partial t} + u_j \frac{\partial E}{\partial x_j} = \frac{1}{\rho}\frac{\partial}{\partial x_j}\left(k \frac{\partial T}{\partial x_j}\right) \tag{3.3}$$

where i and j are indexes denoting the x-, y-, or z-component of the velocity or of the coordinate axes. For clarity, $x_x = x$, $x_y = y$ and $x_z = z$.

3.1.1 Turbulence modelling

In most practical applications the flow is turbulent, which means that it has unsteady velocity fluctuations in most parts of the flow due to the appearance of eddies of various length and time scales. Different numerical methods with different approaches exist with the purpose of capturing the effects of turbulence. The three overall categories for turbulence modelling are Direct Numerical Simulation (DNS), Reynolds-Averaged Navier-Stokes (RANS) and Large Eddy Simulation (LES). A description along with the pros and cons of each category follow.

Direct Numerical Simulation

As the name implies, DNS resolves all parts of the flow, meaning that both the mean flow and all fluctuations are resolved. Therefore, both the time step as well as the grid spacing must be sufficiently small to resolve the eddies of smallest length and time scales. These very small time steps and grid spacing result in huge computational requirements and are therefore rarely used for industrial purposes.

Reynolds-Averaged Navier-Stokes

In RANS, the focus is on the mean flow. The velocity is decomposed into a mean velocity component and a fluctuating component after which the NS-equations are time-averaged. This leads to additional terms in the NS-equations called Reynolds stresses, which are due to the interaction between velocity fluctuations in each direction. These are modelled using a turbulence model. RANS is commonly used in the industry as it gives a reasonably accurate answer to the main parts of the flow at low computational costs.

Large Eddy Simulation

LES resolves the larger eddies of the flow and models the smallest eddies. This is done by solving the space filtered time-dependent NS equations. The space filtering is done by setting a filter cutoff width, which specifies the length scale at which the smaller eddies are not resolved. The cutoff width is usually equal to the given cell size. Similar to RANS, the filtered NS equations result in additional terms called Subgrid-Scale stresses (SGS stresses), which are due to the smaller eddies affecting the resolved flow. The SGS stresses are modelled using an SGS model. In order to capture the motion of the larger eddies, LES requires a smaller grid spacing in comparison with RANS and as unsteady NS equations are solved, this method requires larger computational resources compared to RANS.

Beside the above-mentioned methods, different variations and hybrids of the RANS and LES exist, such as Unsteady RANS (URANS) and Detached Eddy Simulation (DES). However, these are not considered.

Selection of modelling approach

In the present work, the resulting flow phenomena and heat transfer due to vortex generators (VGs) are of interest. To study the effect that both the larger and smaller vortices have on the pressure loss and heat transfer, it is necessary to track the fluid behaviour for different time and length scales. This yields RANS insufficient, since only the main flow structures would be resolved. Therefore, only LES and DNS are considered as valid methods for numerical simulation in the present work. In a study similar to the present work by Sohankar (2007), DNS and LES were compared for numerical simulation of the flow and heat transfer in a rectangular channel with rectangular vortex generators. It was found that LES with a relatively fine grid provided similar results to DNS with a finer grid at lower computational costs. Therefore, LES is chosen as the method for numerical simulation in the present work.

3.1.2 Setup of Large Eddy Simulation

In LES, the time-dependent NS equations are space filtered with a given cutoff width. In the case of incompressible flow, the energy is written as a temperature equation. The space filtered momentum- and temperature equations are given in equations (3.4) and (3.5) (Mirzaei et al., 2014). The overbar indicates spatial filtering.

$$\frac{\partial \bar{u}_i}{\partial t} + \frac{\partial \left(\bar{u}_i \bar{u}_j \right)}{\partial x_j} = -\frac{1}{\rho} \frac{\partial \bar{p}}{\partial x_i} + \frac{\partial}{\partial x_j} \left[(\nu + \nu_{\mathrm{t}}) \frac{\partial \bar{u}_i}{\partial x_j} \right] + \beta \delta_{1i} \tag{3.4}$$

$$\frac{\partial \bar{T}}{\partial t} + \frac{\partial \left(\bar{u}_j \bar{T} \right)}{\partial x_j} = \frac{\partial}{\partial x_j} \left[\left(\frac{\nu}{\mathrm{Pr}} + \frac{\nu_{\mathrm{t}}}{\mathrm{Pr}_{\mathrm{t}}} \right) \frac{\partial \bar{T}}{\partial x_j} \right] - \gamma \bar{u}_1 \tag{3.5}$$

where ν_{t} is the turbulent viscosity modelled through the SGS model and Pr_{t} is the turbulent Prandtl number which is a user-specified value. The variables, β and γ, are the streamwise pressure- and temperature gradients which are used when applying periodic boundary conditions. These are elaborated upon later in this section. As the ability to simulate periodic heat transfer is standard in OpenFOAM, equation (3.5) is manually written into the solver algorithm as suggested by Hærvig (2018). The code can be found in Appendix E. A verification of the code is conducted in Section 3.4.

An SGS model is used to model the stresses caused by the eddies not captured in the LES simulation. In the present work, the SGS model Wall-Adapting Local Eddy-viscosity (WALE) model is used. The WALE model is well suited for wall bounded flow, since the eddy viscosity naturally goes to zero near the wall (Nicoud and Ducros, 1999).

Based on Sohankar (2007), (Sohankar and Davidson, 2001) and (Mirzaei et al., 2014), the Crank-Nicolson scheme with Euler blending is used for time discretization which is an implicit scheme based on central differencing, hence it is second-order accurate. The Euler blending is used to improve the robustness of the simulation. Spatial discretization is based on the second-order central differencing scheme (Mirzaei et al., 2014).

To solve the discretized NS equations, the Pressure-Implicit with Splitting of Operators (PISO) algorithm is used. In general, the algorithm couples pressure and velocity for iterative solution of the NS equations by the use of several pressure-correction steps. The algorithm is described in more detail in (Versteeg and Malalasekera, 2007). The algorithm is run with an adjustable time step based on a maximum value of the Courant number.

As the present work focuses on the fluid flow and heat transfer in a channel with a periodic geometrical arrangement, periodic boundary conditions are applied. Therefore, the flow cross-section will also vary periodically, thus the usual definitions of the thermally developed regime does not apply. This concept was generalised by Patankar et al. (1977) and a brief overview of the concepts that apply in the present work are described in the following.

In Figure 3.1, a schematic of the overall flow domain where VGs are placed in a periodic staggered arrangement in a rectangular channel is shown. For most practical applications, the size of such a domain would require substantial amounts of computational resources to simulate, if well resolved solutions were to be achieved. Therefore, to reduce computational costs, it is assumed that the flow patterns will be subject to a periodic structure. A single period is therefore used as the computational domain, as illustrated in Figure 3.1. The specific placement of the computational domain should only be considered as an example of a period and not an actual placement. Due to the periodic assumption, the fluid interactions with the side walls are not considered.
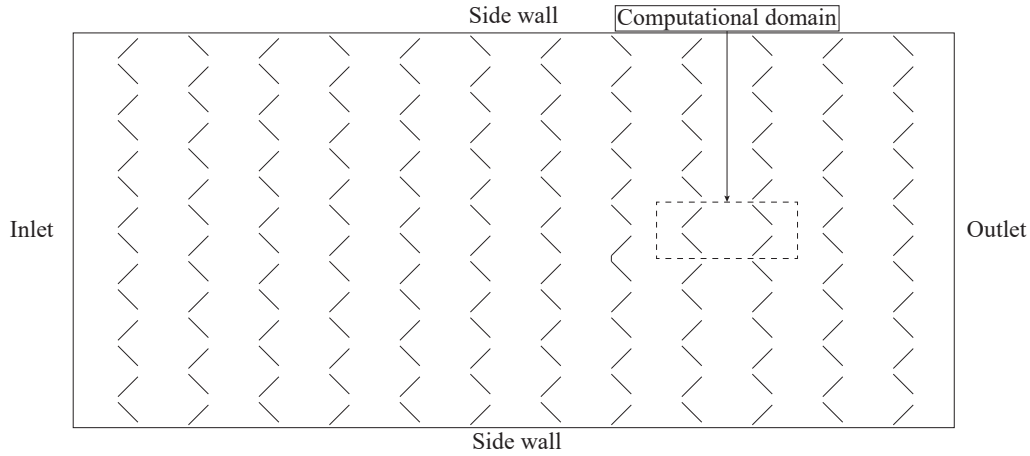
Figure 3.1. Overall flow domain with a periodic arrangement of VGs in a rectangular channel. The inlet, outlet and side walls are illustrated for interpretation. The dashed rectangle illustrates the computational domain.

Based on the assumption regarding periodic flow conditions, additional terms are included in the Navier-Stokes equations as presented in equations (3.4) and (3.5). The pattern of the periodic fully developed temperature field depends on the thermal boundary condition. In the current case, the pattern is based on a constant wall heat flux. Thus, the gradients β and γ are defined as the following (for the two-dimensional case) (Patankar et al., 1977):

$$\beta = \frac{p\left(x, y\right) - p\left(x + L_{\mathrm{d}}, y\right)}{L_{\mathrm{d}}} \tag{3.6}$$

$$\gamma = \frac{T\left(x + L_{\mathrm{d}}, y\right) - T\left(x, y\right)}{L_{\mathrm{d}}} \tag{3.7}$$

where L_{d} is the length of the computational domain. In this case, β is based on the specified bulk velocity and γ is a specified value which can be calculated based on the heat flux as given in equation (3.8).

$$\gamma = \frac{\dot{q}}{H c_{\mathrm{p}} u_{\mathrm{bulk}} \rho} \tag{3.8}$$

By introducing these two parameters, the pressure and temperature can be divided into two components:

$$p\left(x, y\right) = -\beta x + \hat{p}\left(x, y\right) \tag{3.9}$$

$$T\left(x, y\right) = \gamma x + \hat{T}\left(x, y\right) \tag{3.10}$$

where $\hat{p}$ and $\hat{T}$ are the periodic terms. In this way, the pressure and temperature solved in equations (3.4) and (3.5) is the periodic part. The final setup, including the remaining boundary conditions, for the LES simulations are summarised in Table 3.1. The boundary type "Walls" comprise the upper and lower wall of the computational domain as well as the winglets. The other boundaries, which include inlet, outlet, front and back, are specified as "Other".

Simulation method	LES	
SGS model	WALE	
Discretisation scheme		
Temporal	Crank-Nicolson Euler with 0.9 blending	
Spatial	Central difference	
Solver algorithm	PISO	
Boundary conditions	Walls	Other
Velocity	No-slip	Periodic
Pressure	Zero-gradient	Periodic
Temperature	Constant temperature	Periodic
Turbulent viscosity	Zero-gradient	Periodic
Mesh type	Hexahedral	

Table 3.1. Final setup for the LES simulations.

3.2   Mesh considerations

To perform the numerical simulations, a structured mesh of the computational domain, shown in Figure 3.2, must be generated.
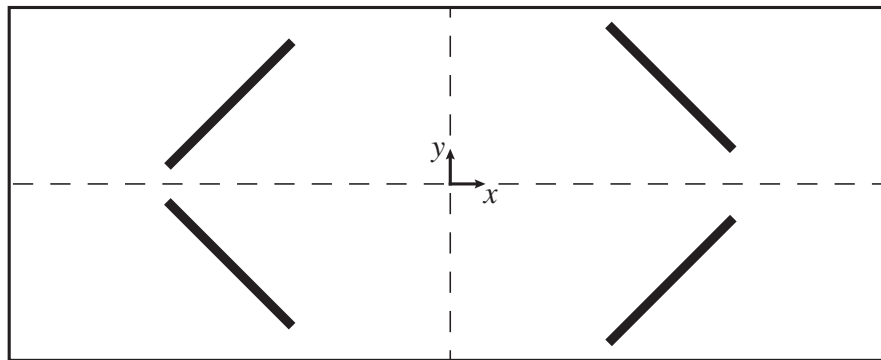
Figure 3.2. Schematic of computational domain illustrating the winglets and x- and y-axes.

The mesh is manually generated in MATLAB and then translated into the OpenFOAM utility called blockMesh, which is used to generate the mesh in OpenFoam (Greenshields, 2017). This is done to have full control of the mesh structure. A thorough description of the meshing routine is described in Appendix B.

In order to reduce the number of discretization errors when doing LES, different consideration made to improve the quality of the mesh. The main ones are listed below. The considerations are mainly based on the discretization errors in LES discussed by Villiers (2006) as well as the guidelines given by ERCOFTAC (2000). Worth noting is that due to some geometrical limitations, the considerations mentioned below can not be applied in all areas of the mesh, but rather wherever it is possible.

- The cells are directed parallel to the expected direction of the flow.
- Wall adjacent blocks have a higher cell density in order to capture the boundary layer flow. Furthermore, the wall normal resolution is made very fine ($y^+ \approx$ 1-2). This is achieved by applying a cell expansion ratio or by refining the mesh near the walls.
- Highly skewed cells are avoided, meaning that all angles of the cells should be around 90 degrees. If this is not possible, a minimum or maximum angle of 40 or 140 degrees, respectively, are desired.

- A high cell aspect ratio are avoided in important regions of the flow. However, near the wall where the gradient in the streamwise direction is much lower than in the wall-normal direction, this restriction can be relaxed.
- A smooth transition between fine and coarse blocks is desired. This is important in an LES simulation, since a sudden change between coarse and fine cells will result in an error due do an inconsistency between the SGS turbulent energy and the SGS length scale (Villiers, 2006). In transitions from coarse cell density blocks to fine cell density blocks, a cell expansion ratio is applied to the coarse block to improve the transition.

In Figure 3.3, a 2D extract of the base mesh with 1.1 million cells is shown. This is the reference mesh used for examining grid convergence.
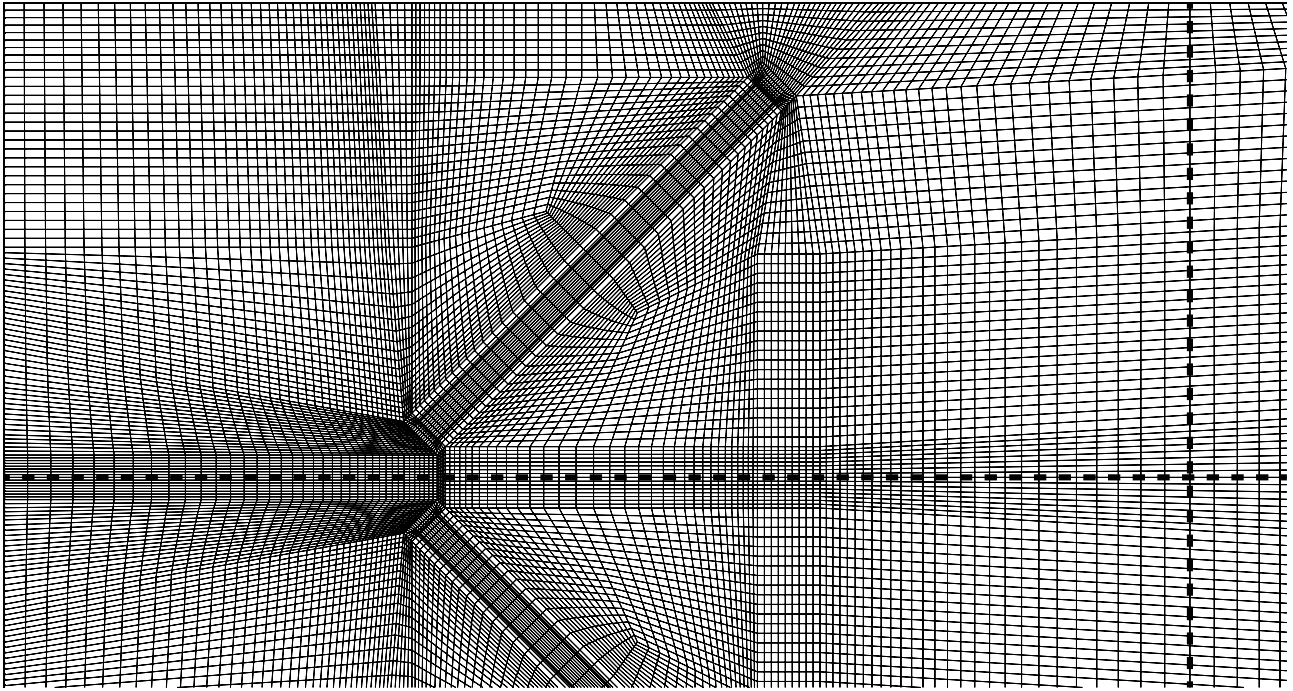

Figure 3.3. Extract of the reference mesh with 1.1 million cells. The x- and y-axes are illustrated by the dotted lines.

3.3 Global solution parameters

As a measure of the heat transfer and the pressure loss, the dimensionless parameters Nusselt number, Nu, and loss coefficient, f, are used. The calculation of these are described in the following. Furthermore, the performance parameter used to evaluate the heat transfer enhancement relative to the pressure loss is defined.

3.3.1 Nusselt number

An expression for the Nusselt number is obtained by combining the general definition of Nusselt number with Newton's law of cooling and Fourier's law of heat conduction. This yields the expression in equation (3.11).

$$\mathrm{Nu} = -\frac{\mathrm{d}T}{\mathrm{d}n}\frac{H}{\Delta T} \tag{3.11}$$

where the height of the duct H is used as the characteristic length. To compute the global Nusselt number in the LES simulation, the wall normal temperature gradient and the overall temperature difference must be obtained.

The wall normal temperature gradient is computed as an area-averaged value over all of the boundary walls:

$$\frac{\mathrm{d}T}{\mathrm{d}n} = \frac{\sum\limits_{i=1}^{N} \frac{\mathrm{d}T}{\mathrm{d}n} A_i}{\sum\limits_{i=1}^{N} A_i} \tag{3.12}$$

where i is the the wall face number and N is the total number of wall faces.

Similarly, the overall temperature difference is obtained by computing the bulk temperature as a streamwise velocity-averaged value over the inlet of the domain:

$$\Delta T = T_{\mathrm{wall}} - T_{\mathrm{bulk}} = T_{\mathrm{wall}} - \frac{\sum\limits_{j=1}^{M} T_j u_{1j} A_j}{\sum\limits_{j=1}^{M} u_{1j} A_j} \tag{3.13}$$

where j is the inlet face number and M is the total number of inlet faces. The subscript 1 indicates the streamwise velocity component.

3.3.2 Loss coefficient

A common way of the defining the loss coefficient is given in Equation 3.14, which is the definition used in the present work (Esmaeilzadeh et al., 2017).

$$f = \frac{H}{0.5 \rho u_{\mathrm{bulk}}^2} \frac{\mathrm{d}P}{\mathrm{d}x} \tag{3.14}$$

where u_{bulk} is the bulk velocity and $\mathrm{d}P/\mathrm{d}x$ is the global streamwise pressure gradient.

3.3.3 Performance parameter

In order to evaluate the heat transfer enhancement relative to the increase in pressure loss a performance parameter, η, which is based on equal pumping power, is used (Webb and Eckert, 1972). The performance parameter is given as:

$$\eta = \frac{\mathrm{Nu}/\mathrm{Nu}_0}{(f/f_0)^{1/3}} \tag{3.15}$$

where Nu_0 and f_0 are the Nusselt number and the loss coefficient, respectively, for the channel flow of the same geometry but without winglets. These are described in Section 3.6.

3.4 Verification of the implemented heat transfer code

In order to verify the implemented heat transfer code, a test simulation for a conventional rectangular channel with an aspect ratio of 4 is conducted and the Nusselt number is evaluated. For the test simulation, the hydraulic diameter is used as the characteristic length.

The test simulation is run at the same setup as all other simulations. Therefore, the general setup is given in the following.

Beside the numerical setup in Table 3.1, different flow and heat transfer properties are specified and given in Table 3.2. The simulations are conducted at a Reynolds number of 700, based the channel height, H. The

kinematic viscosity and Prandtl number are given at the initial fluid temperature. As mentioned earlier, the time step is adjusted according to the maximum allowed Courant number, CFL. A Courant number of 0.85 is chosen as suggested by Mirzaei et al. (2014). The temperature gradient, γ, is chosen arbitrarily, since the Nusselt number is strictly flow dependent in the current case. This is possible since γ is strictly related to the heat flux, which is not of interest. Furthermore, the specific values of the boundary temperatures have no effect on the solution, since the thermodynamic properties are assumed to be independent of temperature, which is a valid assumption within the given temperature range. Also, the Nusselt number is independent of the specific value of the temperatures.

Parameter	Description	Value	Unit
Re	Reynolds number	700	-
u_{bulk}	Streamwise bulk velocity	1.054	m/s
T_{fluid}	Initial fluid temperature	20	°C
T_{wall}	Wall temperature	50	°C
ν	Kinematic viscosity	1.505e-5	m^2/s
Pr	Prandtl number	0.71	-
Pr_t	Turbulent Prandtl number	0.85*	-
γ	Streamwise temperature gradient	100	°C/m
CFL	Maximum Courant number	0.85	-

Table 3.2. Flow and heat transfer properties used throughout the simulations. *(ANSYS, 2018)

As the test simulation is a simple laminar case, the turbulent properties go toward zero, which simplifies the flow computations significantly. Therefore, a coarse mesh resolution is sufficient. In Table 3.3, the result from the simulation is compared to the literature. In the laminar flow regime, the Nusselt number is independent of Reynolds number, which justifies the comparison (Cengel et al., 2012).

Parameter	Description	Value
	Dimensions	
H	Height of channel	10 mm
B_p	Channel width	$4H$
D_h	Hydraulic diameter	16 mm
B_p/H	Channel aspect ratio	4
	Results	
Nu_{sim}	Nusselt number from simulation	5.32
Nu_{ref}	Nusselt number from literature*	5.33

Table 3.3. Hydraulic dimensions and resulting Nusselt number from test simulation and from literature. *Cengel et al. (2012).

The relative deviation is $\sim$0.2 % for which reason the implemented heat transfer code is considered verified. Based on this, the entire setup for the LES simulations is complete and the grid convergence can be conducted.

3.5 Grid convergence study

In order to reduce the errors due to coarseness of the grid, a grid convergence study is conducted. This is done by examining the results from a refinement of the mesh.

3.5.1 Periodicity

Due to the assumption about periodicity of the flow, a study to determine the time until the flow is periodic is conducted. This is done by running a simulation with the reference mesh of 1.1 million cells. For convenience, a dimensionless flow through time, t^*, is defined, which is normalised with the flow through time of one period T_p. The flow through time is given from the bulk velocity and the length of the domain:

$$T_p = \frac{L_d}{u_{bulk}} \tag{3.16}$$

The normalised flow through time is then given as:

$$t^* = \frac{t}{T_p} \tag{3.17}$$

This means that for example $t^* = 2$ corresponds to two periods i.e. that the flow has passed through the domain two times. In Table 3.4, the dimensions of the computational domain are given. All dimensions are scaled relative to the channel height, H.

Parameter	Description	Value
H	Channel height	10 mm
L_d	Length of domain	$10H$
B_d	Width of domain	$4H$
α	Angle of attack	$45°$
h	Winglet height	$0.5H$
e	Winglet tip distance	$0.4H$
t_w	Winglet thickness	$0.1H$
l	Winglet length	$2H$
B_p	Transverse pitch distance	$4H$
L_p	Longitudinal pitch distance	$5H$

Table 3.4. Dimensions of computational domain.

The periodicity simulation is run for ten periods after which the loss coefficient and Nusselt number are evaluated. The fluctuating part of the Nusselt number and the loss coefficient as a function of the normalised flow through time are shown in Figure 3.4. It is seen that after approximately four periods, the signals stabilise. An additional period is included and thus the flow is assumed to be periodic after five periods.
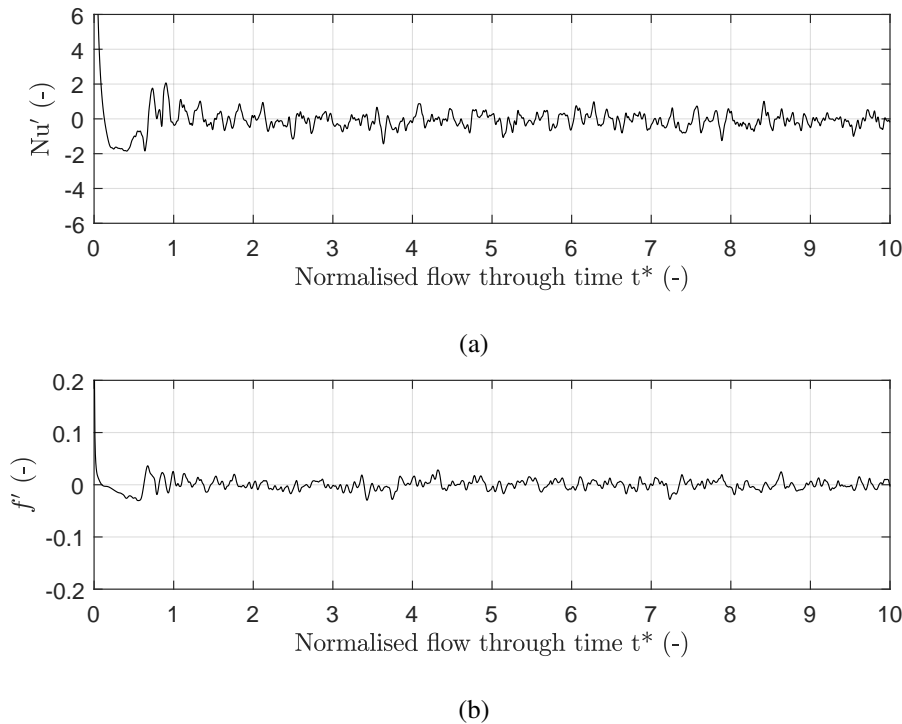
(a)

(b)

Figure 3.4. Fluctuating part of (a) the Nusselt number and (b) the loss coefficient as function of the normalised flow through time t^*.

3.5.2   Mesh refinement

The grid convergence study is based on the method presented by Roache (1994), who proposed a general method for determining grid convergence, based on the use of Richardson's extrapolation. A brief description of the method is presented in Appendix B. The Nusselt number and loss coefficient are used to determine grid convergence.

For the grid convergence study, three different mesh sizes are used and these are 1.1, 2.2 and 4.4 million cells. The three meshes are in the following referred to as "coarse", "medium" and "fine". The maximum number of cells is limited to achieve a reasonable computational time. As the time step is adjusted with the Courant number, a decrease in cell size will result in a smaller time step, which leads to a substantial increase in computational time when refining the mesh. During the mesh refinement, the overall structure is kept the same e.g. y^+ is kept constant as described in Appendix B. In order to reduce computational time, the last time step, from the simulation used for studying the periodicity, is used as the starting point for the three simulations. For the medium and fine meshes, the OpenFOAM function *mapFields* is used to map the flow and temperature fields onto the new meshes containing additional number of cells.

From the simulations, the Nusselt number and loss coefficient for each time step are given and an average value for each parameter is computed. To reduce the dependence on the fluctuations, as shown in Figure 3.4, the simulations are run for 45 periods. Ideally, the average values should be calculated from uncorrelated data, which means that the time between samples should be twice the integral time-scale of the flow. This is used and described in the experimental Chapter 4.3. However, as this would require a substantial amount of computational time to get the required number of samples, an average over all time steps are used.

In Figure 3.5 and 3.6, the loss coefficient and Nusselt number as function of grid size are shown along with the extrapolated exact solution. A summary of the resulting grid convergence parameters are shown in Table 3.5.
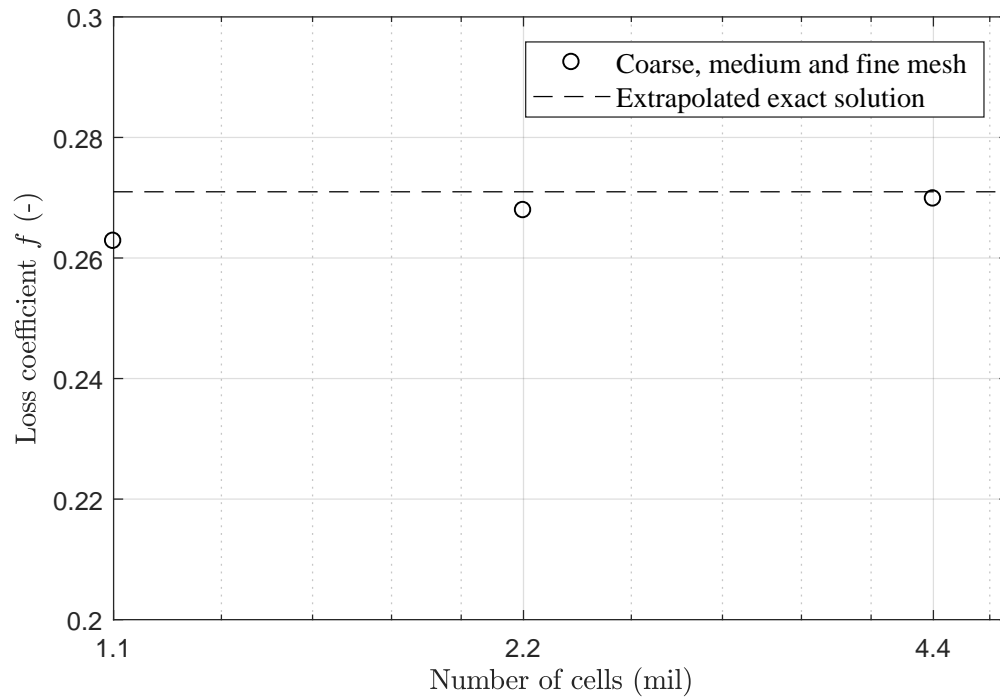
Figure 3.5. Loss coefficient as a function of grid size. The extrapolated exact solution is shown with a dashed line.
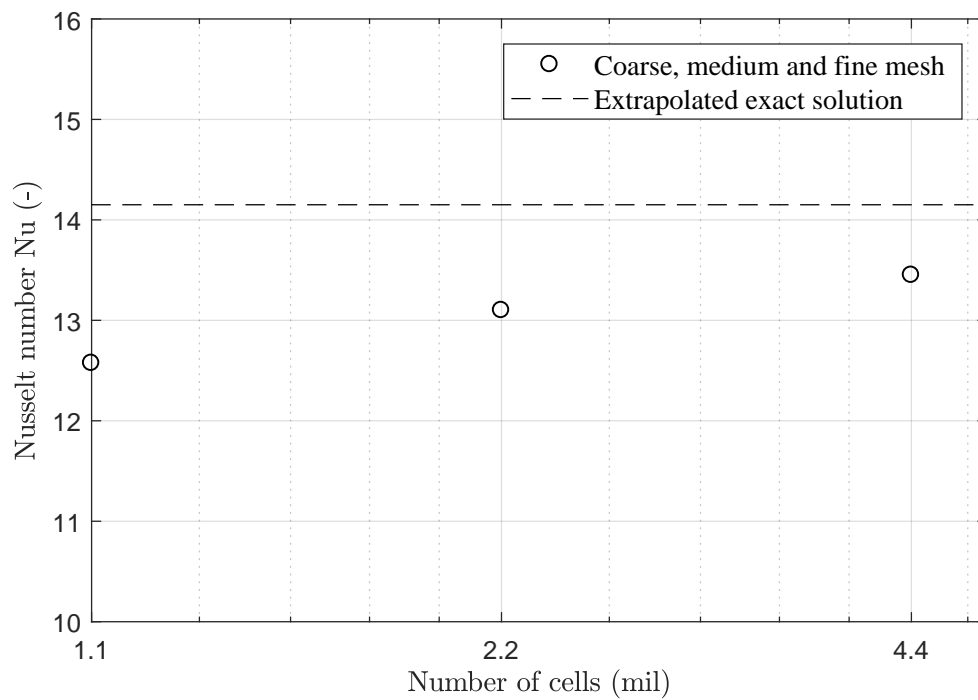

Figure 3.6. Nusselt number as a function of grid size. The extrapolated exact solution is shown with a dashed line.

Parameter	Description	Value			
r	Grid refinement ratio				$\sqrt[3]{2}$
F_s	Safety factor				1.25
Nusselt number					
		Coarse	Medium	Fine	Exact
Nu	Nusselt number	12.57	13.10	13.45	14.15
p	Order of convergence				1.75
		Value		Ideal	
GCI_fine	Grid convergence index for fine and medium grid	0.07		0	
GCI_coarse	Grid convergence index for medium and coarse grid	0.10		0	
C	Asymptotic range of convergence	1.03		1	
Loss coefficient					
f	Loss coefficient	2.63	2.68	2.70	2.71
p	Order of convergence				4.21
		Value		Ideal	
GCI_fine	Grid convergence index for fine and medium grid	0.01		0	
GCI_coarse	Grid convergence index for medium and coarse grid	0.01		0	
C	Asymptotic range of convergence	1.01		1	

Table 3.5. Summary of grid convergence parameters as described in Appendix B.

The loss coefficient yields a high order of convergence, p, as well as solutions well within the asymptotic range of convergence. Going from the coarse to the medium grid yields a solution close to the extrapolated exact solution, which is indicated by the low grid convergence index (GCI). The relative change in loss coefficient is 1.9 % between the coarse and the medium grid and 0.7 % between the medium and the fine grid.

The Nusselt number has a lower order of convergence, which evidenced from Figure 3.6, with an extrapolated exact solution approximately 5 % above the fine grid. Looking at the relative change between the grids, the change is 4.0 % between the coarse and the medium grid and 2.6 % between the medium and the fine grid. The lower convergence in Nusselt number could indicate that the smaller eddies, which are resolved when decreasing the grid spacing, have a significant impact on the surface heat transfer. Therefore, a simulation with a very small grid spacing would be required to see a possible convergence of the Nusselt number below the one computed using extrapolation.

Due to the small relative changes between the different grid spacings as well as the fact that the loss coefficient does converge, the medium mesh with 2.2 million cells is chosen as the final mesh for the present work. The mesh is shown in Figure B.4 in Appendix B.

3.6 Design of parametric study

Prior to defining the simulations for the parametric study presented in Chapter 5 some initial simulations are conducted.

To compare the numerical results to that of a channel without VGs, a reference case is simulated. The reference simulation is run with the same settings as described in Section 3.4 for the same geometry, but without the winglets. As this is a pure laminar case, the Nusselt number and loss coefficient converge for which reason the last values are sufficient as results. The simulation yields a Nusselt number of $\mathrm{Nu}_0 = 4.11$ and a loss coefficient of $f_0 = 0.028$.

For the present work, the height of the winglets, h, and the longitudinal pitch distance, L_p, are varied to

investigate the effect on the heat transfer and pressure loss. The dimensions for the benchmark case is the same as the ones used for the grid convergence study and are given in Table 3.4. Both geometrical parameters are varied +-40 % relative to the benchmark with an increment of 20 %. The resulting values for winglet height and longitudinal pitch distance are given in Table 3.6.

Winglet height (h/H)	Longitudinal pitch distance (L_p/H)
0.3	3
0.4	4
0.5*	5*
0.6	6
0.7	7

Table 3.6. Dimensions for winglet height and longitudinal pitch given as a function of channel height H. *Benchmark value.

As the resulting tendencies might be dependent on the value of the parameter that is kept constant, all possible combinations are simulated. This results in 5x5 = 25 simulations. Each simulation is initially run for five periods ($t^* = 5$), where the flow is assumed to be periodic. Then, each simulation is run for a given number of periods after which average values are computed. The number of periods are chosen based on when the change in the average velocity profile is minor. To reduce the computational time, a minimum number of periods are desired. To determine this, the simulation used for the convergence study, is used. In Figure 3.7, the average spanwise velocity profile located at ($x/L_p = 0, h/H = 0$) after ten periods is shown. In Figure 3.8 the mean of the absolute difference for different periods relative to the one after ten periods are shown.
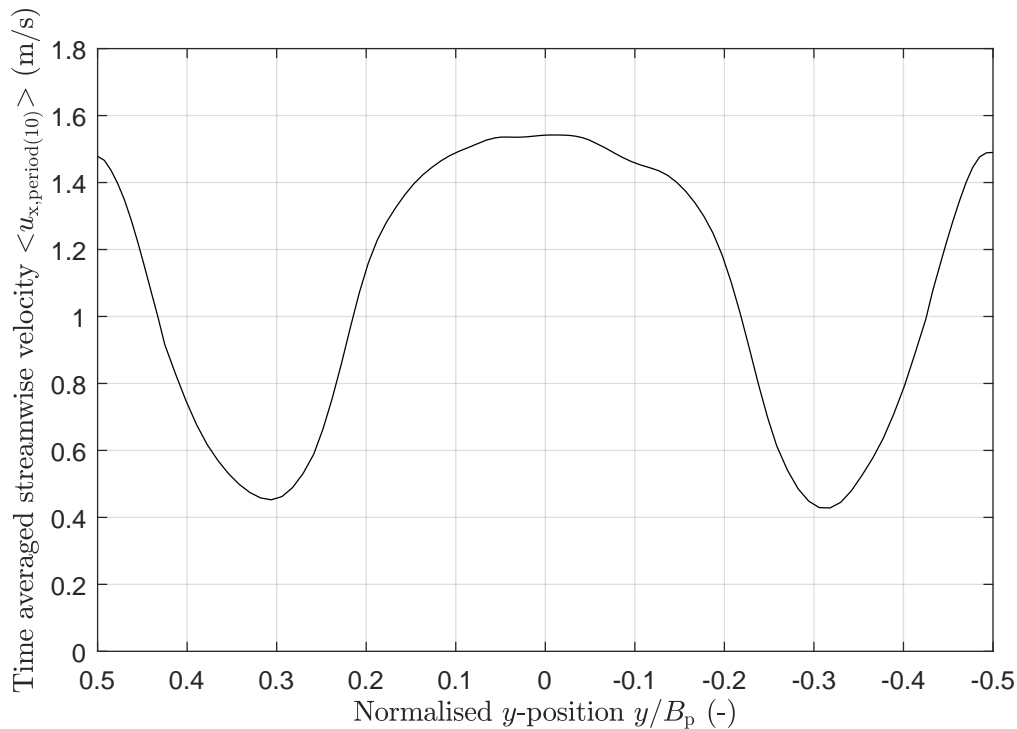

Figure 3.7. Time averaged spanwise velocity profile located at normalised x- and z-position $x/L_d = 0, z/H = 0.5$ after ten periods.
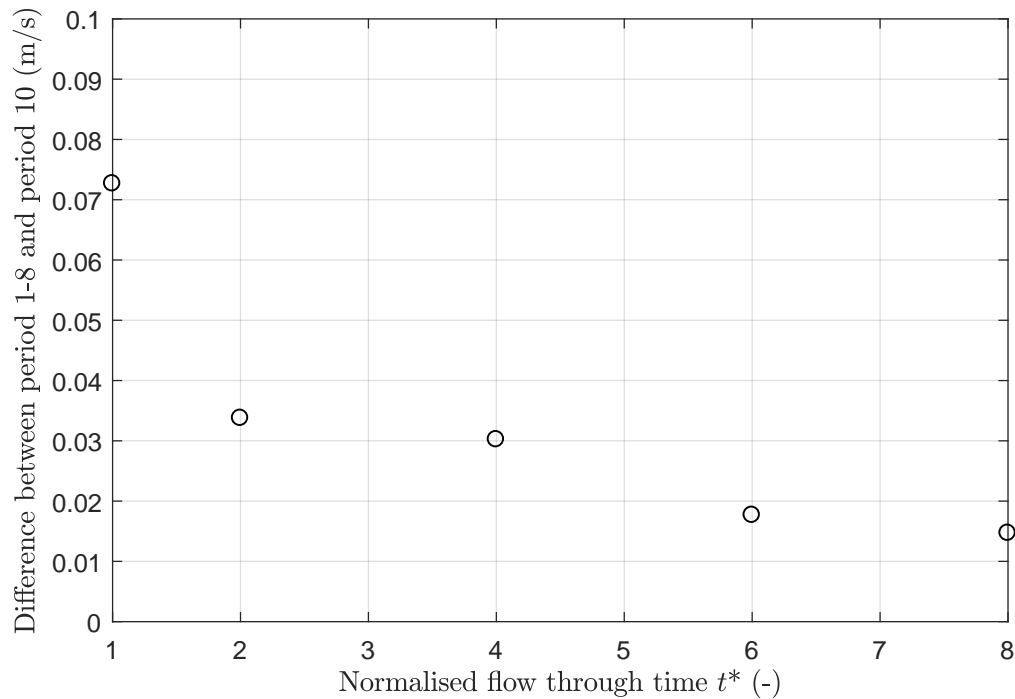
Figure 3.8. Mean of the absolute difference for each velocity profile at each period relative to period number ten.

It is seen that after six periods, the relative change is no longer significant. Therefore, a simulation time of six periods ($t^* = 6$) is chosen for determining average values. As the variation in longitudinal pitch distance affects the period length, the flow through time varies for the different simulations. A table containing the number of cells, flow through time, time to periodicity, total simulation time and results for each simulation is shown in Table D.1 in Appendix D.

CHAPTER 4

EXPERIMENTAL FLUID MECHANICS

This chapter comprise of the selection of measurement method and the associated procedures and considerations made to design the experiment used validate the Large Eddy Simulation setup. The first part of the chapter concerns the determination of the most suitable measurement method. This lays the ground for the second part of the chapter where the design of the test channel is presented based on the requirements of the chosen measurement method. Finally, the experimental setup and procedure, including statistical considerations and preliminary experiments, are presented which form the basis for the final experiments used for validation.

The experiment is used as a tool to investigate how closely the LES setup resembles real life flow phenomena. The validation is based on the flow in the channel with focus on the streamwise velocity. Referring to the problem statement, a fully developed channel flow with a staggered periodic arrangement of rectangular winglets pairs is investigated. The experiment is conducted in a WT241 wind tunnel by Baltic Windtunnel GmbH. Therefore, a suitable experimental method must be found to suit this application. As seen in the literature study in Appendix A, several experimental methods exist. Hot Wire Anemometry (HWA) has shown popularity among several authors in earlier investigations, however, more recent experimental investigations such as the ones by Dupont et al. (2003) and Akcayoglu (2011) have used optical experimental methods such as Laser Doppler Anemometry (LDA) and Particle Image Velocimetry (PIV). This is because LDA and PIV are non-intrusive measurement methods meaning that no physical interaction between the area of interest and the measurement equipment is necessary. This means that no modifications to the test section are necessary in comparison to HWA where entrances into the test section would be required. This leads to less disturbances of the flow during measurements for which reason more attention is devoted to LDA and PIV to determine which method that suits the case at hand.

4.1 Characteristics of Laser Doppler Anemometry and Particle Image Velocimetry

PIV and LDA are both non-intrusive optical measurement techniques and are therefore immediately well-suited for this application. However, there are differences between the methods and these are elaborated upon in this section. A brief description of the methods and their characteristics will follow.

4.1.1 Laser Doppler Anemometry

LDA is a point measurement technique that offers high accuracy for single point measurements. The principle of backscattering LDA is that a single laser beam is split into two and set to cross at a desired location. The crossed laser beams create a small measuring volume with a well defined fringe pattern, see Figure 4.1. When a particle crosses the measuring volume it scatters light back to a receiver. The scattered light fluctuates in intensity as it passes the fringes yielding a frequency proportional to the velocity of the particle.
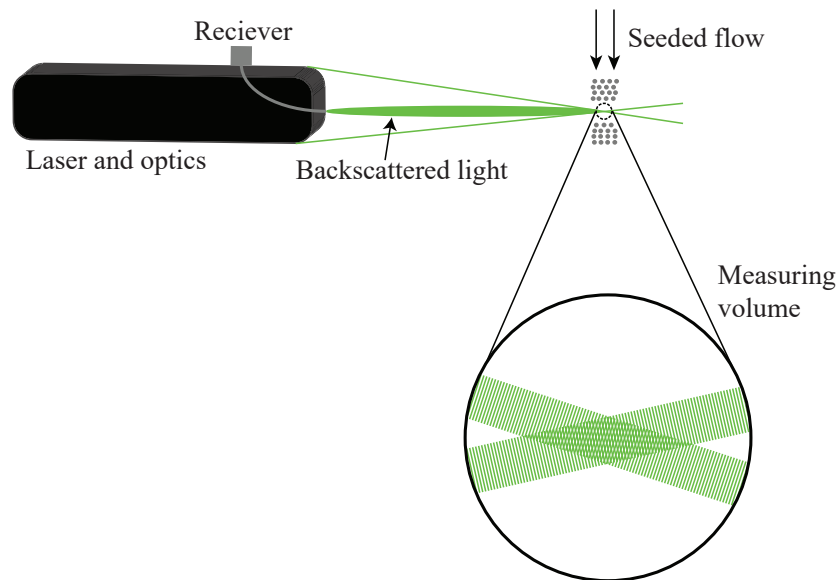
Figure 4.1. General principle of one-dimensional LDA.

LDA systems can achieve an accuracy in the order of 0.1 % when appropriately calibrated and without calibration, LDA systems can achieve an accuracy in the order of 1 % (Dues and Neuer, 2016). Additionally, due to its high spatial and temporal resolution, LDA is ideal for measurements of both time-independent flow statistics such as moments of velocity as well as time-dependent flow statistics such a flow spectra and correlation functions at a point (Jensen, 2004). The high spatial resolution of LDA is due to the small measuring volume formed by the laser beams. Typical dimensions of the measuring volume are in the order of 100 µm in diameter and 1 mm in length (Jensen, 2004). The high temporal resolution of LDA is due to the high frequency response of commercial signal processors which are able to deal with data rates in the hundreds of kHz range (Jensen, 2004). The main disadvantage of LDA is that it is time consuming e.g. when having lots of measurement points.

4.1.2 Particle Image Velocimetry

PIV is a field measurement technique that offers an instantaneous image of the flow field at a given time. The principle of PIV is that tracer particles in the fluid are illuminated by a light sheet created by a pulsating laser. The laser is pulsating with a known time interval which controls a camera to be recording at these times. For evaluation, the images are divided into smaller so-called interrogation areas (IAs) where the local displacement of particles between the first and second illumination is determined for each IA by means of statistical methods. This yields the instantaneous velocity field of the flow. The general principle of two-dimensional PIV is presented in Figure 4.2.
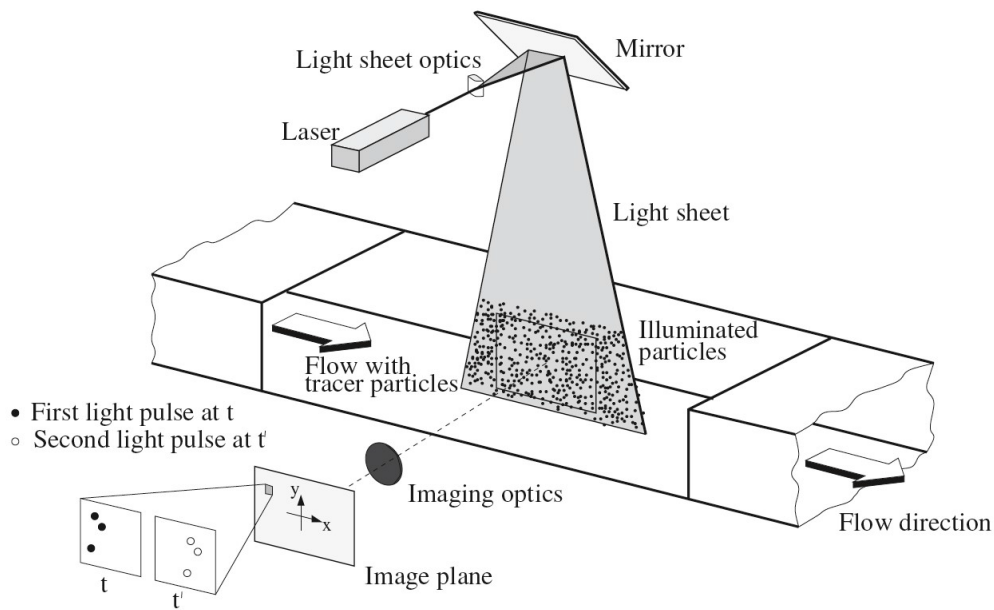
Figure 4.2. General principle of two-dimensional PIV (Raffel et al., 2007).

To achieve high accuracy with PIV, the spatial and temporal resolution should be as high as possible. The spatial resolution is limited by the IA size relative to the resolution of the camera. Typical IA sizes are 32x32 pixels and 64x64 pixels (Jensen, 2004). The temporal resolution is dependent on the pulsing frequency of the laser and on the camera frame rate, with the latter often being the limiting factor. When conducting PIV experiments it is usually necessary to make a trade-off, due to equipment constraints, between camera frame rate and resolution and laser light intensity and repetition rate to ensure coherence between temporal and spatial resolution. Another limiting factor for the precision of PIV is calibration. The particle displacement and velocity are calculated from the recorded images and therefore it is necessary to know the magnification factor to relate image pixels to physical distance.

4.1.3 Selection of experimental method

With a brief description of LDA and PIV a comparison between the two is made to determine which method that suits the needs of the experiment the best. Table 4.1 states the characteristics of both methods.

	LDA	PIV
Characteristics	Non-intrusive Point measurement method Accuracy: - 0.5...0.1 % with calibration - No need for calibration for uncertainties above 1 % High cost system	Non-intrusive Whole field method Accuracy dependent on: - Equipment specifications - Calibration High cost system
Spatial Resolution	High, due to small measuring volume. Typically 100 µm x 1 mm.	Dependent on: - IA size - Image resolution - Image magnification
Temporal Resolution	High, due to fast signal processing.	Dependent on: - Camera frame rate - Laser repetition rate

Table 4.1. Characteristics of LDA and PIV.

From Table 4.1, it is evident that there are significant differences between the two methods. The most obvious difference is that LDA is a point measurement method while PIV is a field measurement method. Furthermore, LDA can generally achieve a higher accuracy than PIV and PIV systems are more reliant on state-of-the-art equipment to achieve reasonably high spatial and temporal resolution compared to LDA.

Since the main purpose of the experiment is to validate the LES setup, LDA is desired due to its high accuracy, spatial and temporal resolution. Another practical advantage of using LDA for this experiment is that it has less strict seeding requirements compared to PIV (Melling, 1997).

4.2   Test channel

With LDA chosen as the experimental method the test channel can be designed. The main purpose of the test channel is to facilitate LDA measurements which requires optical access into the channel. Furthermore, periodic flow conditions in the streamwise and spanwise direction is investigated through the LES simulations for which reason the test channel should be designed to obey these conditions. The experiments are conducted in a WT241 wind tunnel for which the test section is enclosed by windows as seen in Figure 4.3. The channelis attached to the base plate in the test section and the LDA probe is placed normal to the front window. This means that optical access is already ensured into the test section of the wind tunnel.
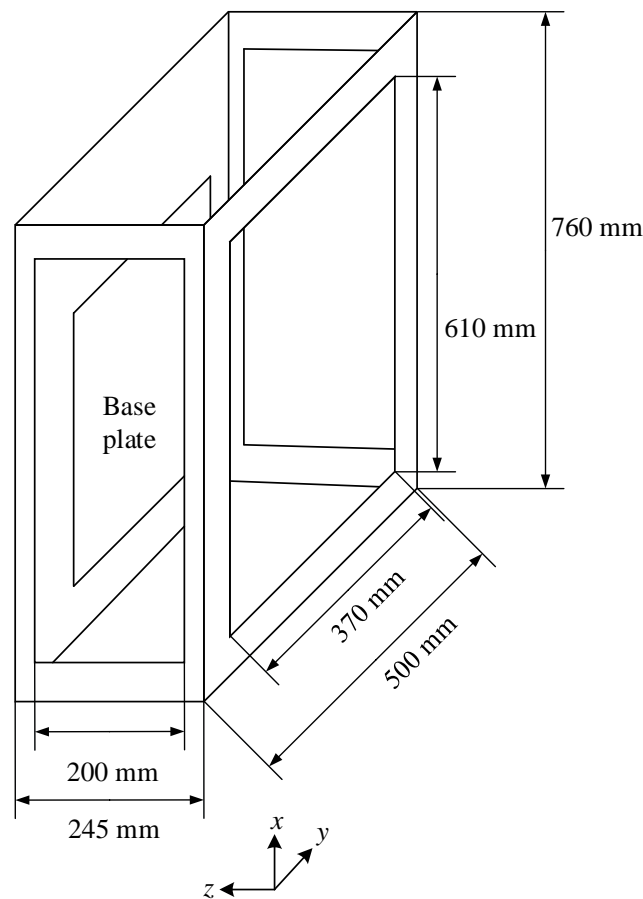

Figure 4.3. Schematic of the wind tunnel test section.

Besides optical access, seeding access must also be ensured into the wind tunnel test section in order to perform LDA measurements. Furthermore, it is desired that the test channel lies within the dimensions of the windows enclosing the test section. It has to be noted that a miniature channel is not desired due to the size of the LDA

measuring volume and manufacturing. A large LDA measuring volume relative to the test channel may yield uncertainties and as the measuring volume approaches the walls. Past experience has proven that difficulties occur because of high noise levels due to scattering (Romano, 1992).

The requirements to the test channel are summed up below:

- Optical access into the test channel must be ensured.
- Periodic flow conditions in the streamwise and spanwise direction must be approached.
- Seeding access into the test section of the wind tunnel must be ensured.
- The dimensions of the test channel must be considered relative to the dimensions of the windows enclosing the wind tunnel test section and the LDA measuring volume.

4.2.1 Design of test channel

The design of the test channel is inspired by the experimental investigations by Tiggelbeck et al. (1992, 1993, 1994). All dimensions are scaled with the height of the channel, H, which is set to 10 mm. The bottom panel of the channel with periodic staggered rectangular winglet pairs is presented in Figure 4.4.
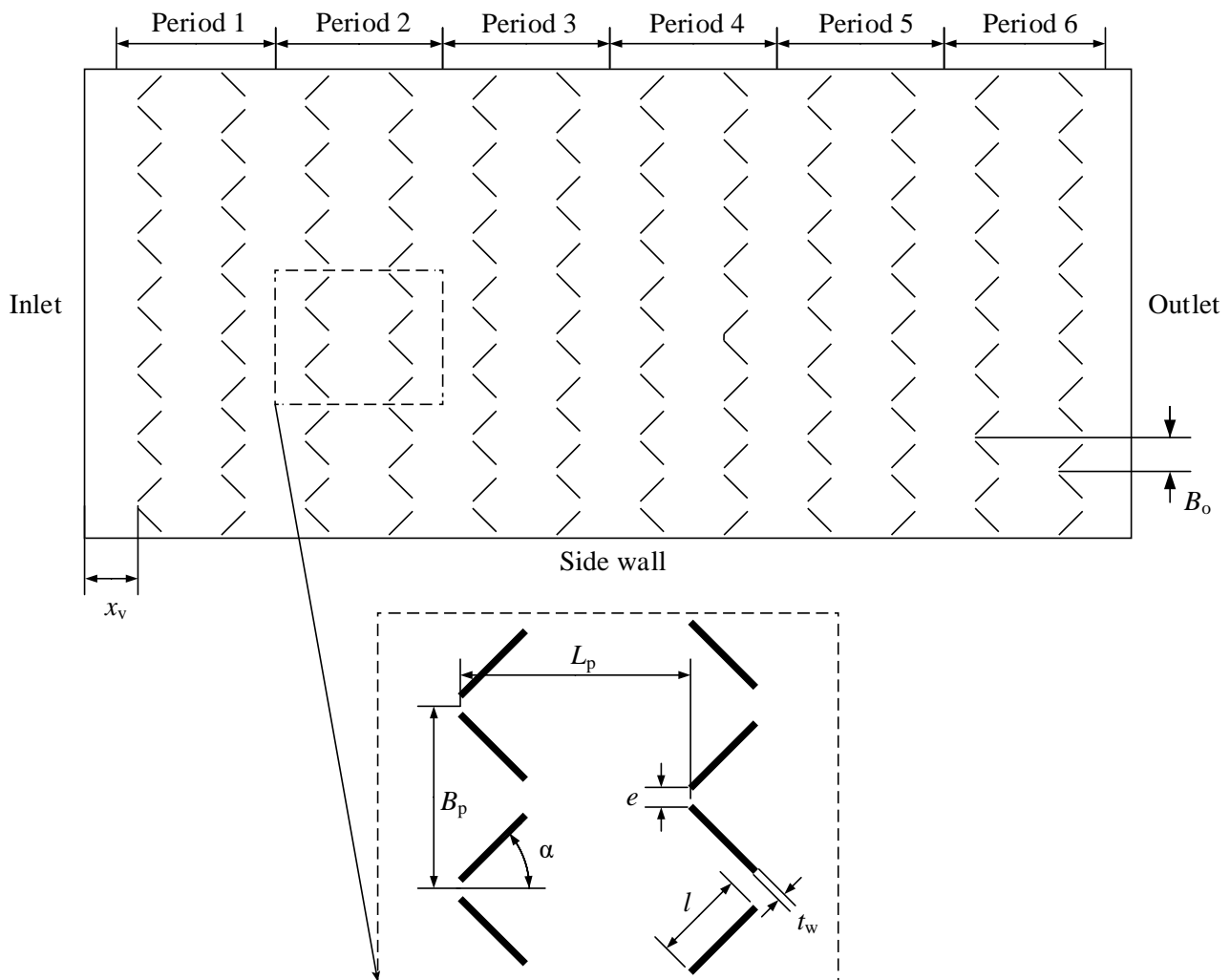

Figure 4.4. The bottom panel of the test channel with periodic staggered rectangular winglet pairs. The span of each period is shown.

The panel consists of 6 periods in the streamwise direction where each period covers two rows of winglet pairs.

In the spanwise direction, seven columns of winglet pairs are made. This configuration is made to approach periodicity in both directions within the dimensions of the wind tunnel test section. Furthermore, the winglet pairs are set in a common flow down configuration. The dimensions are given in Table 4.2.

Parameter	Description	Value
	Channel configuration	
H	Channel height	10 mm
L	Channel length	$62.5H$
B	Channel width	$28H$
	Winglet geometry	
α	Angle of attack	$45°$
h	Winglet height	$0.5H$
x_{v}	Distance from channel edge to winglet leading edge	$3H$
e	Winglet tip distance	$0.4H$
t_{w}	Winglet thickness	$0.1H$
l	Winglet length	$2H$
B_{p}	Transverse pitch distance	$4H$
L_{p}	Longitudinal pitch distance	$5H$
B_{o}	Staggered offset	$2H$

Table 4.2. Geometrical dimensions of channel and winglets.

The bottom panel is made from a 10 mm aluminium panel where the 5 mm high winglets are milled directly out of the panel. The top and side panels of the channel are made from 5 mm polycarbonate panels to make the channel optical accessible and to make all sides of the channel of equal thickness. Comparing the channel width and length (280x625 mm) to that of the front window of the wind tunnel test section (370x610 mm) shows that the channel width is within that of the window, however, the length is not. Therefore, it is necessary to make the channel adjustable in the streamwise direction to conduct measurements between all winglet periods. Since the wind tunnel continues beneath the floor it is possible to make the test channel even longer, however, the channel length is kept roughly within the height of the test section. This is to avoid that the test channel reaches into the converging and diverging parts on either side of the test section to minimise disturbances of the flow and thereby achieve an as uniform flow into the channel as possible. Furthermore, the edges of the channel are chamfered at a $45°$ angle to avoid an abrupt stoppage of the flow which might cause vortices to stand across the inlet. With the chamfered edges the excess flow should be guided around the channel leaving a uniform flow in the channel inlet. The finished channel is presented in Figure 4.5.
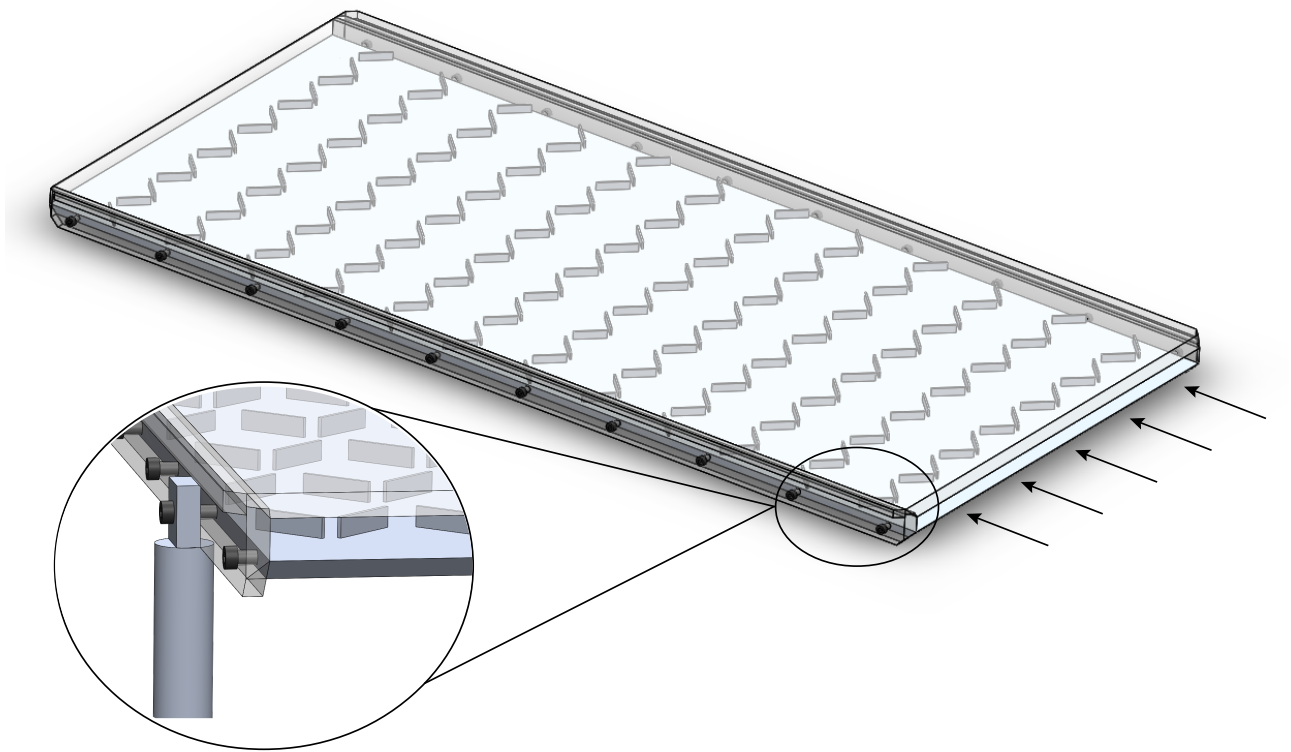
Figure 4.5. 3D drawing of the finished channel with periodic staggered rectangular winglet pairs. The zoomed view shows the chamfered edges and an example of where one of the 'legs', used to attach the channel to the test section base plate, could be placed.

The length of the legs are equal to half the test section width meaning that the test channel is suspended in the middle region of the test section which makes it independent of the boundary layer forming on the sides of the wind tunnel test section.

4.3   Experimental procedure and considerations

Following the preliminary work, i.e determination of experimental method and design of test channel, experiments can be conducted. The experimental setup is shown in Figure 4.6.

x
y
z

Laser probe
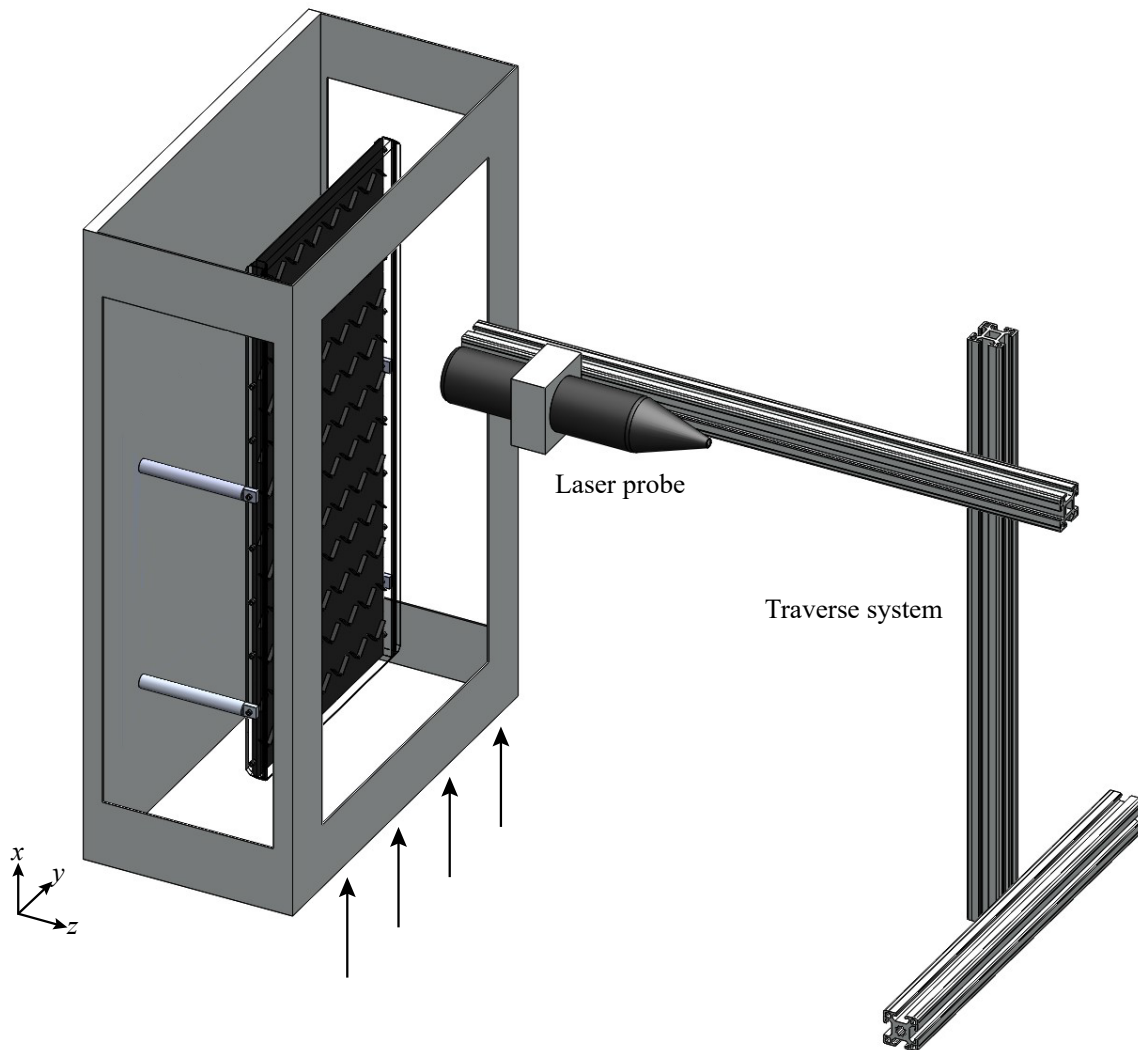
Traverse system

Figure 4.6. Schematic of the experimental setup with the channel inserted in the wind tunnel test section, the LDA laser probe and the traverse system.

4.3.1   Apparatus and components

The apparatus and components used in the experiment as well as their specifications are presented in Table 4.3.

Apparatus	Specification
Ion Laser Technology Model 5500A Laser	Output power range: 10 - 500 mW Wavelength range: 457 - 514.5 nm
Dantec Dynamics FiberFlow transmitter and 2D probe Dantec Dynamics FVA processor and BSA flow software Dantec Dynamics traverse system	160 mm lens on the probe Wavelengths of beam pairs: - 488 nm (blue) - 514.5 nm (green)
Smoke machine for seeding (unknown manufacturer)	Smoke fluid: Ondina oil
WT241 wind tunnel by Baltic Windtunnel GmbH	Wind speed range: 3.5 - 70 m/s

Table 4.3. Overview of the apparatus used in the experiments.

4.3.2 Statistical considerations

Due to the time dependent random motion of the fluid because of turbulence, statistical considerations are made to quantify the dispersion relative to the mean in each measurement. Based on a normal distribution, due to a large number of samples in each point (n>30), and 95 % confidence interval the limits of the mean are determined from equation (4.1) (Walpole et al., 2014).

$$<x> \pm z_{\alpha/2} \frac{s}{\sqrt{n}} \tag{4.1}$$

where s is the sample standard deviation, $<x>$ is the sample mean, n is the number of samples and $z_{\alpha/2}$ is the critical value for 95 % confidence interval for a normal distribution meaning that $\alpha = 1 - 0.95 = 0.05$ and $z_{\alpha/2} = 1.96$. The sample mean and sample standard deviation are calculated from equations (4.2) and (4.3) (Walpole et al., 2014).

$$<x> = \sum_{i=1}^{n} \frac{x_i}{n} \tag{4.2}$$

$$s = \sqrt{\sum_{i=1}^{n} \frac{(x_i - <x>)^2}{n-1}} \tag{4.3}$$

Beside the above mentioned, velocity bias must also be considered when using mean values. Velocity bias in a turbulent flow becomes significant if the sampling rate is considerably larger than the mean frequency of fluctuations (Zhang, 2010). This means that velocities with a large magnitude are sampled more frequently than velocities with a small magnitude. Thereby, the time between samples are not equidistant and the arithmetical mean will be biased i.e. reach a higher value than a mean velocity based on equidistant time intervals. This is also referred to as correlated samples. To avoid velocity bias and to ensure statistically independent samples, the integral time scale, τ_ℓ, of the flow is calculated based on the LES simulations. It is calculated from the LES simulations since it is not possible to achieve sufficiently high data rates during the experiment to resolve the flow. The integral time scale is found by integrating the area under the autocorrelation function as shown in equation (4.4).

$$\rho(s) = \frac{<u'(t)u'(t+s)>}{<u'(t)^2>}$$
$$\tau_\ell = \int_0^\infty \rho(s)ds \tag{4.4}$$

where s is the time lag, ρ is the autocorrelation function coefficient and τ_ℓ is the integral time scale (Pope, 2000).

Since the time step in the simulation is based on the Courant number, it is not equidistant throughout. Therefore, to calculate the autocorrelation function, the time and velocity vectors are converted to be equally spaced using interpolation. Data from the grid convergence simulation with 2.2 million cells (Section 3.5) are used to find the integral time scale of the flow. The autocorrelation function is calculated for each of the probe locations with Figure 4.7 showing the autocorrelation function at an arbitrary probe location.
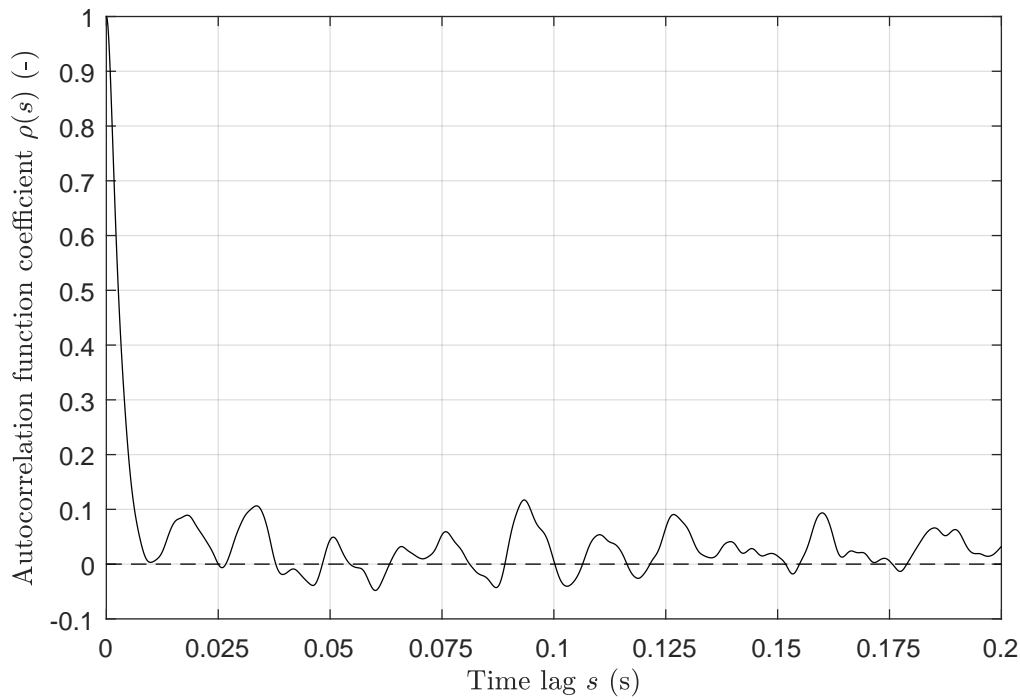
Figure 4.7. Autocorrelation function at an arbitrary location as function of time equal to two flow throughs of the domain.

As seen from Figure 4.7, the autocorrelation function decreases rapidly and then continues to oscillate around the zero axis. The oscillations is a consequence of repeating flow structures due to turbulence. There is a significant peak approximately at a time lag of 0.1 s which is attributed to the periodic boundary conditions. The periodic boundary conditions cause the flow structures leaving the domain to re-enter the domain from the upstream side and thus a peak occur in the time correlations. The integral time scale is, as stated in equation 4.4, the area under the autocorrelation function curve, however, the signal is biased due to the periodic boundary conditions. A common way to account for the biasing effect is to truncate the integral at the first minimum of the curve (Quadrio and Luchini, 2003). This yields an integral time scale of $\tau_\ell = 0.0032$ s = 3.2 ms. To ensure statistically independent samples the time between samples must be at least two times the integral time scale, $2 \cdot \tau_\ell = 6.4$ ms, as stated by Dantec Measurement Technology (2000). Based on this, the time between samples in the experiments is set to 8 ms.

4.3.3 Seeding considerations

For the accuracy of LDA experiments it is important that the seeding particles are able to follow the flow accurately. This means that the particle response time must be low compared to the characteristic time of the flow. This is usually quantified by the Stokes number which is defined in equation (4.5). If St « 1, the particle response time is significantly less than the characteristic time of the flow. In this case the particles will have ample time to react to changes in the flow for which reason the particle and fluid velocities will be nearly equal. If St » 1, the particles do essentially have no time to react to fluid velocity changes and will therefore only be affected a little by a change in fluid velocity.

$$\text{St} = \frac{\tau_P}{\tau_F} \tag{4.5}$$

τ_P is the particle response time and τ_F is the characteristic time of the flow (Michaelides et al., 2016). The particle response time is the time required for the particle to accelerate from zero velocity up to 63.2 % of the

fluid flow velocity and is given in equation (4.6) (Novotný and Manoch, 2012).

$$\tau_P = \frac{\rho_P d_P^2}{18\mu_F} \tag{4.6}$$

where d_P is the particle diameter, ρ_P is the particle density and μ_F is the fluid dynamic viscosity. The properties are all determined at 20°C. The average size of the seeding particles generated by the smoke machine is unknown for which reason an approximation is made. Ondina oil have been used to generate smoke as gas flow seeding by both Greated et al. (2002) and Vestøl et al. (2018). The average particle diameter was in both cases 2 μm. Therefore, to make sure that the particle size is not underestimated, an average particle diameter of 4 μm is assumed. Furthermore, an even distribution of particles in the channel is assumed. The density of the particles is set equal to the Shell Ondina Oil 917 used by Vestøl et al. (2018) and it is 854 kg/m³. This yields a particle response time of $\tau_P \approx 42$ μs. The integral time scale determined previously is used as the characteristic time of the flow. This yields a Stokes number of St = 0.013. A Stokes number of 0.2 is chosen as the limit for when the particles can follow the flow (Jebakumar et al., 2016). The particles used in the experiment can therefore follow flow structures with a characteristic flow time of approximately 15 times lower than the integral time scale.

4.3.4 Presentation of experimental uncertainties

This section serves to present the different sources of uncertainties encountered in the experiments. The uncertainties are divided into two parts namely general uncertainties encountered in LDA experiments and specific uncertainties for the experiments conducted in this study.

General uncertainties for LDA experiments

In Section 4.3 the general definition of velocity bias was introduced in relation to sampling and this is accounted for using a time between samples of more than twice the integral time scale. However, local velocity bias can occur if velocity gradients are present along the length of the LDA measuring volume (Zhang, 2010). This phenomenon is illustrated in 4.8.
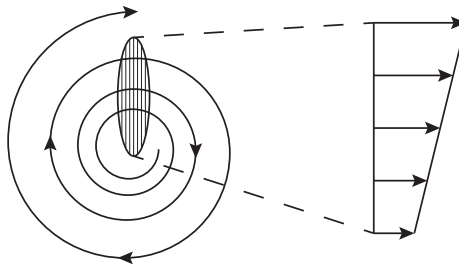

Figure 4.8. Spatial velocity gradient across LDA measuring volume.

It is evident from Figure 4.8 that there is a spatial velocity gradient across the LDA measuring volume. This leads to a non-uniform particle arrival rate and thus to a non-uniform distribution of velocity events along the measuring volume. Therefore, the time average of the velocities might be slightly shifted.

Over the course of LDA experiments temperature changes may occur resulting in changes of fluid and particle densities. This may be due to changing characteristics of the surroundings or because the laser heats up the fluid during measurements. Furthermore, the seeding concentration over time and distribution hereof as well as the size and shape distribution of particles may affect the measurements. The larger particles scatter light with higher intensity than the smaller particles but do not respond to changes in the flow as rapidly as the

smaller particles. This may lead to larger particles, that not following the flow as well, getting counted as a valid measurement and thereby bias the overall impression. In this regard, it is generally desired to have thin glass surrounding the area of interest due to its low absorption coefficient. If the absorption gets too high, some smaller particles may be sorted out due to their lower scattering intensity. This may have an increased significance due to the combined effect of the LDA system used being a back-scattering system and that the particles scatter the most light in the forward direction i.e. in the direction away from the incoming light.

Specific uncertainties for the present experiment

During the experiments it has been noticed that an oil film coating the channel top panel and the wind tunnel front window affected the percentage of validated samples. Furthermore, as these panels have been extensively polished and cleaned for oil, scratches have occurred. A combination of these are assumed to have affected the scattered light of the particles for which reason some of the attempted samples have been rejected instead of validated. It has not been possible to determine the specific circumstances for the formation of the oil film, but it is assumed that it is a combination of seeding concentration and measurement time. The measurement time is therefore limited to 90 seconds per measurement point. Furthermore, the measurement section in the experiment is surrounded by approximately 10 mm polycarbonate which may lead to problems with acquiring signals from smaller particles with lower intensity scattering.

4.4 Investigation of flow periodicity through the channel

Velocity measurements behind the middle winglet pair in each period as seen in Figure 4.9 are conducted to investigate when the flow in the test channel approaches a periodic behaviour. This is to determine where the final measurements used to validate the LES setup are to be conducted.
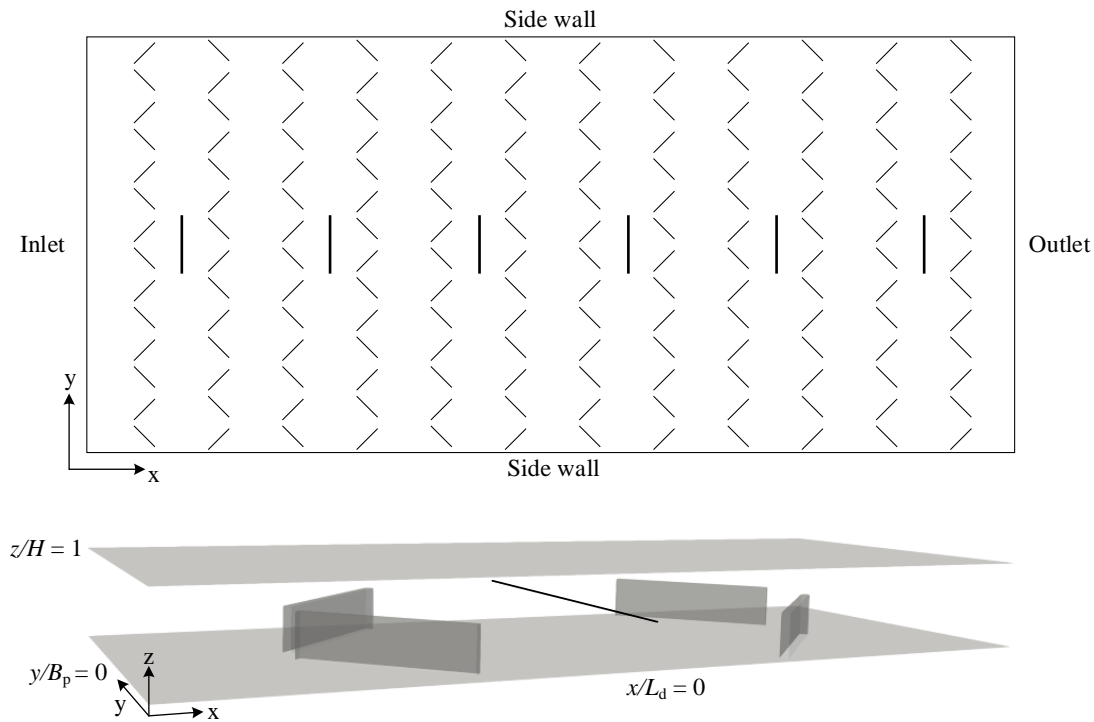

Figure 4.9. Measurements are conducted along the highlighted line in each of the six periods to determine when the flow approaches a periodic behaviour. The location of the measurement section is $x/L_{\mathrm{d}} = 0$ and $z/H = 0.5$. Measurements are conducted across the y-direction over a span of $y/B_{\mathrm{p}} = \pm 0.5$.

Prior to the measurements, preliminary experiments have been conducted to determine the settings for the LDA system, to adjust the position of the LDA probe measuring volume in the channel and to determine a stable freestream velocity in the wind tunnel. It was found that the bottom panel of the channel had to be painted black due to reflections. Furthermore, a stable freestream velocity of 4 m/s was determined for the wind tunnel. The settings used for the experiments are listed in Table 4.4. Further elaboration of the results can be found in Appendix C.

Settings	Value
High voltage	On, 1500 V
Signal-to-noise validation	On, -3 dB
Burst detector bandwidth	80,000 Hz
Transit time resolution	7 µs/bit
Range/Gain of velocity 1. Bandwidth 2. Frequency shift 3. Signal Gain	1. 4.00 MHz 2. 40 MHz 3. High
Laser intensity	High

Table 4.4. LDA specific settings used in the experiments.

The velocity measurements are beside the settings presented in Table 4.4 conducted using *burst mode* and with a measurement interval of 30 seconds. The time averaged velocity profiles for each period are shown in Figure 4.10. Since the velocity measurements are conducted in *burst mode*, which means that a sample is taken every time the system detects a signal, some of the data might be correlated. Therefore, the particle arrival times (AT) and corresponding velocities for each point are sorted with the condition that $AT \geq 8$ ms. This results in data sets that are statistically independent.
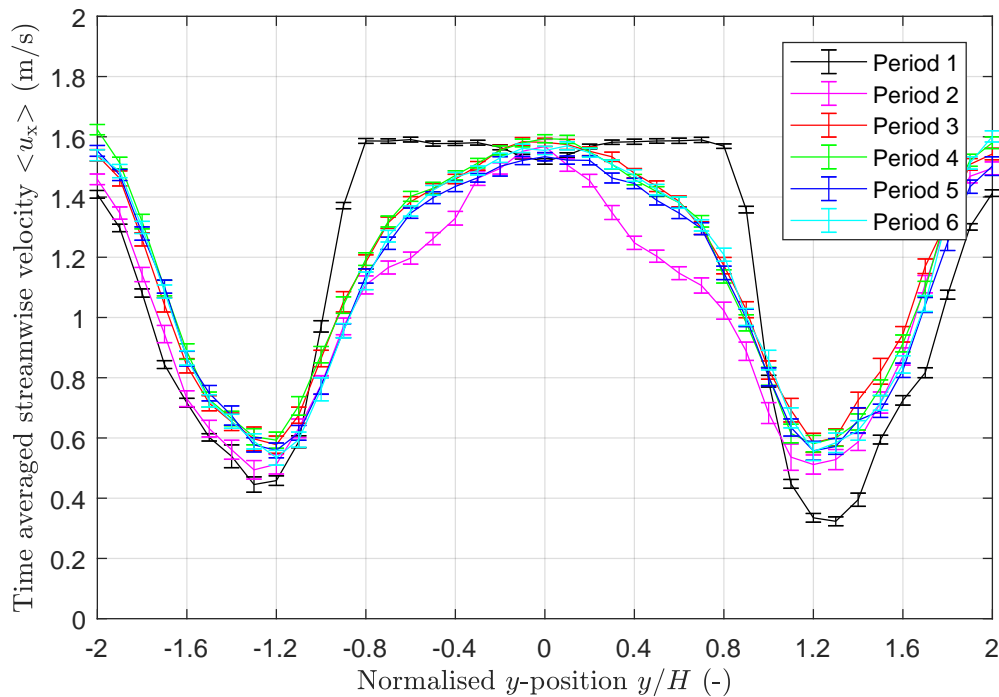

Figure 4.10. Time averaged streamwise velocity as function of channel normalised y-position for period 1 through period 6. The error bars are based on a 95 % confidence interval.

It is seen from Figure 4.10 that the time averaged streamwise velocity profiles of period 1 and 2 deviate significantly from the others. However, the velocity profiles of period 3 through 6 show a similar tendency. To quantify the development of the streamwise flow down the channel, the time averaged velocity profile of period 6 is subtracted from the time averaged velocity profiles in each of the previous periods. The result is shown in Figure 4.11.
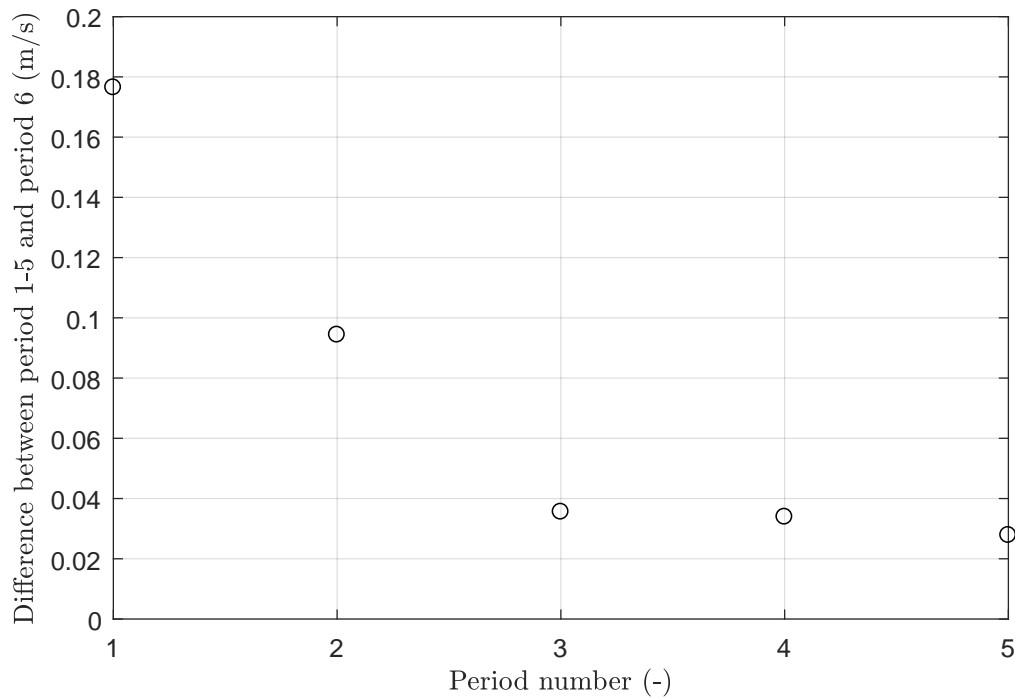

Figure 4.11. Absolute difference between the time averaged streamwise velocity profile of period 1 to 5 and the time averaged streamwise velocity profile of period 6.

Figure 4.11 supports the fact that the absolute differences of period 1 and 2 are significantly larger compared to that of period 3 through 5. Even though the absolute difference between period 3, 4 and 5 is small, it is decreasing suggesting that the flow is getting increasingly more periodic down the channel. Since period 6 is the last period in the channel and that the difference between period 5 and period 6 is relatively small, period 6 is chosen as the location for which the validation experiments are conducted and the flow is considered to be periodic. The final experimental setup is presented in Figure 4.12. The only changes to the measurement settings for the validation experiments are that *Deadtime mode* with a deadtime of 8 ms is used instead of *burst mode* and the measurement interval is raised to 90 seconds. *Deadtime mode* means that every time a sample is registered, there is a time delay of 8 ms before another sample can be registered. Thereby, statistically independence is assured for all the obtained data.
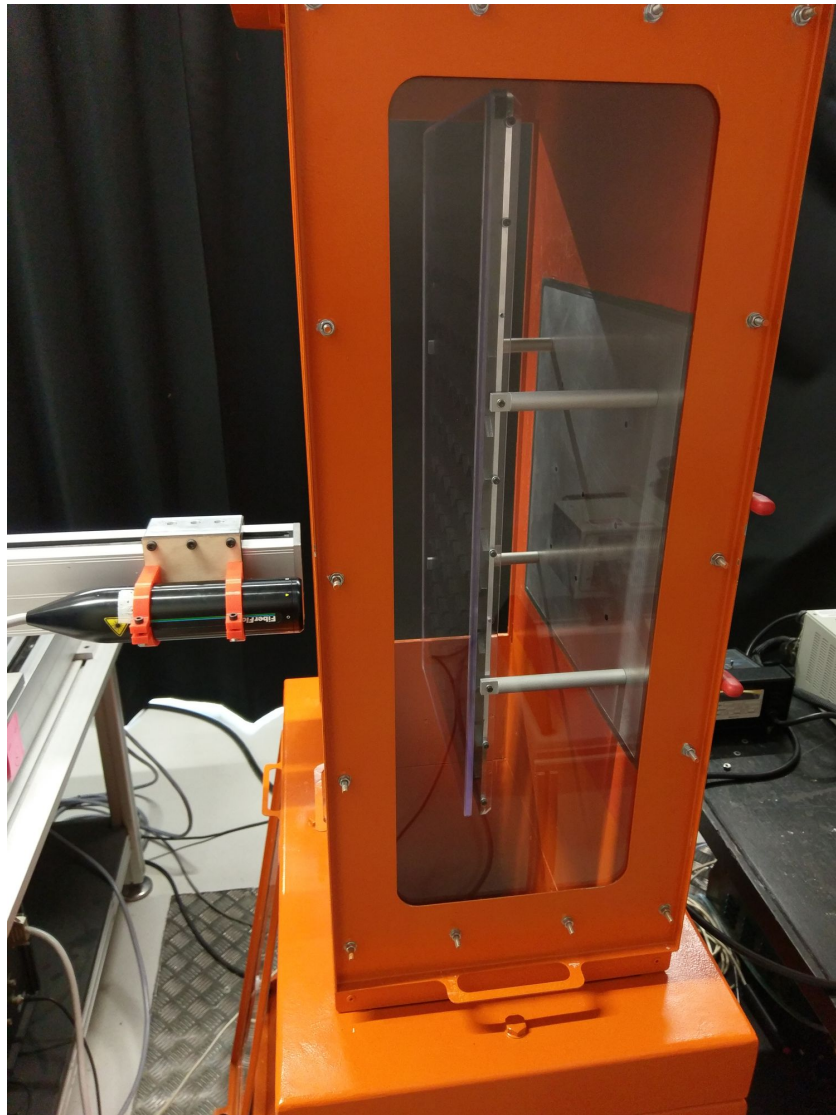
Figure 4.12. Actual experimental setup used to conduct measurements.

EXPERIMENTAL VALIDATION AND NUMERICAL PARAMETRIC STUDY

In this chapter the experimental validation of the Large Eddy Simulation (LES) setup is presented followed by the results from the numerical parametric study. Five different longitudinal pitch distances and winglet heights form the basis for the parametric study resulting in a total of 25 different configurations. The flow phenomena resulting from the geometrical changes are studied to determine their influence on heat transfer enhancement and pressure loss. The chapter is terminated with a presentation of the overall heat transfer performance for the different configurations resulting in an optimum configuration and a discussion of the parametric study results.

5.1 Experimental validation of the LES setup

The time averaged velocity profiles and turbulence intensity profiles across the spanwise direction at two different locations are compared. The simulation profiles are extracted from the grid convergence simulation with 2.2 million cells (see Section 3.5). The two different locations are presented in Figure 5.1.
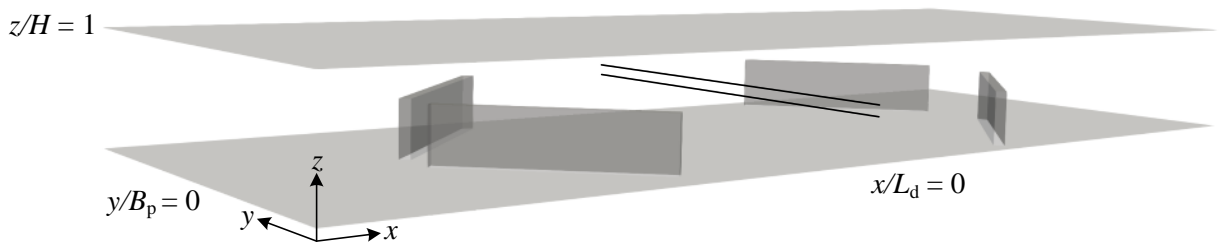

Figure 5.1. The two different locations for which the experimental and numerical spanwise time averaged streamwise velocity and turbulence intensity profiles are compared. The upper line has the following normalised position: $x/L_d = 0$, $y/B_p = \pm 0.5$, $z/H = 0.6$. The lower line has the following normalised position: $x/L_d = 0$, $y/B_p = \pm 0.5$, $z/H = 0.5$.

It has not been possible to determine the exact channel bulk velocity in the experiments, however, the obtained velocity data indicates that the bulk velocity in the experiment is within 5 % of the simulation bulk velocity. The Reynolds number used in the simulations is 700 and therefore the Reynolds number in the experiments lies in the range between 665-735. The flow structures within this range are considered to be similar and thus the velocity profiles from the experiments and simulations are normalised with the maximum velocity in each

case. The velocity and turbulence intensity profiles as function of the normalised y-position are presented in Figures 5.2-5.5.
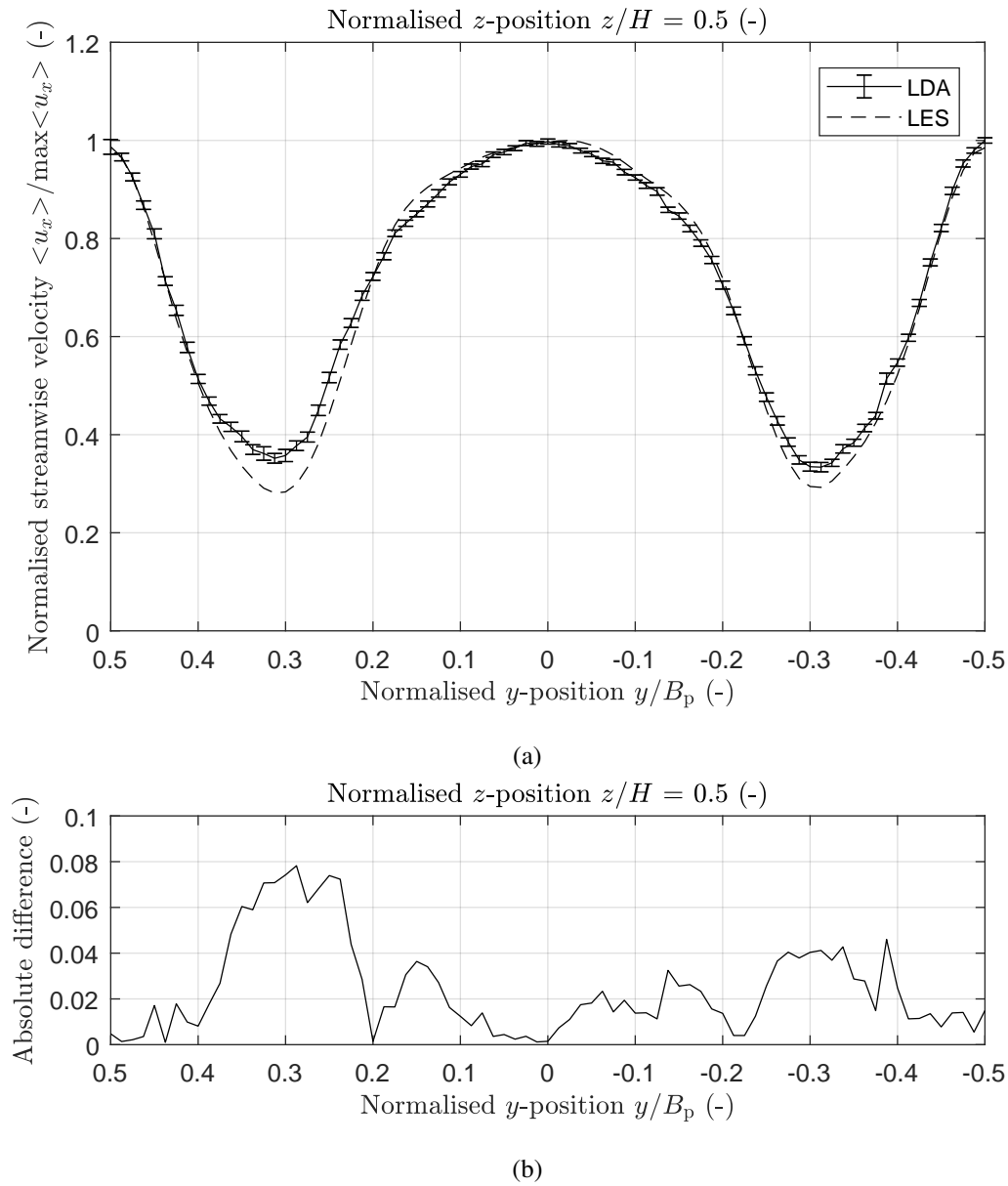

(a)

(b)

Figure 5.2. (a) Normalised time averaged streamwise velocity as function of normalised y-position at $z/H = 0.5$. The error bars are based on a 95 % confidence interval. (b) Nbsolute difference between the LDA and LES velocity profiles as function of normalised y-position at $z/H = 0.5$. Error bars are omitted for readability.
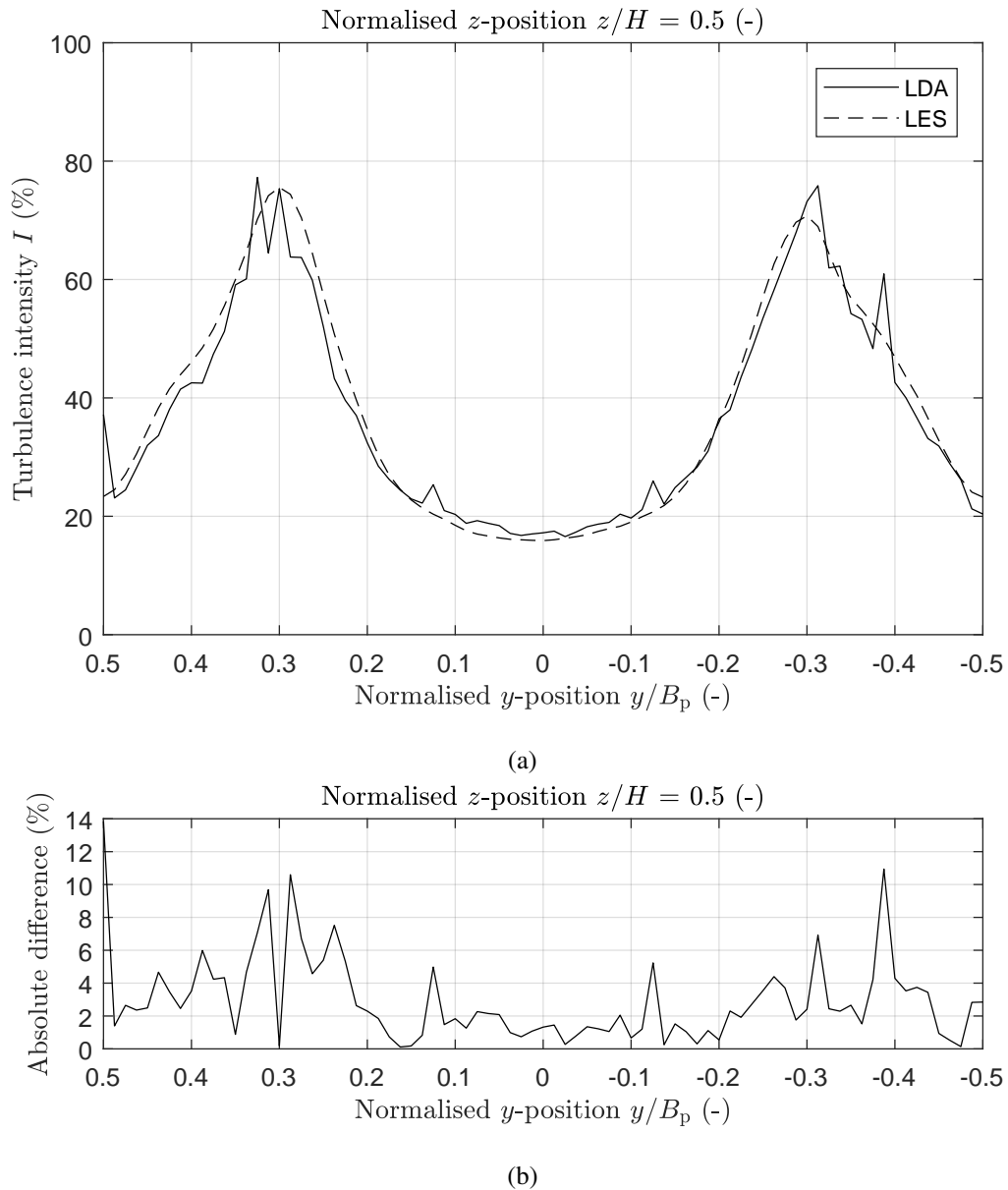
(a)

(b)

Figure 5.3. (a) Turbulence intensity as function of normalised y-position at $z/H = 0.5$. (b) Tbsolute difference between the LDA and LES turbulence intensity profiles as function of normalised y-position at $z/H = 0.5$.
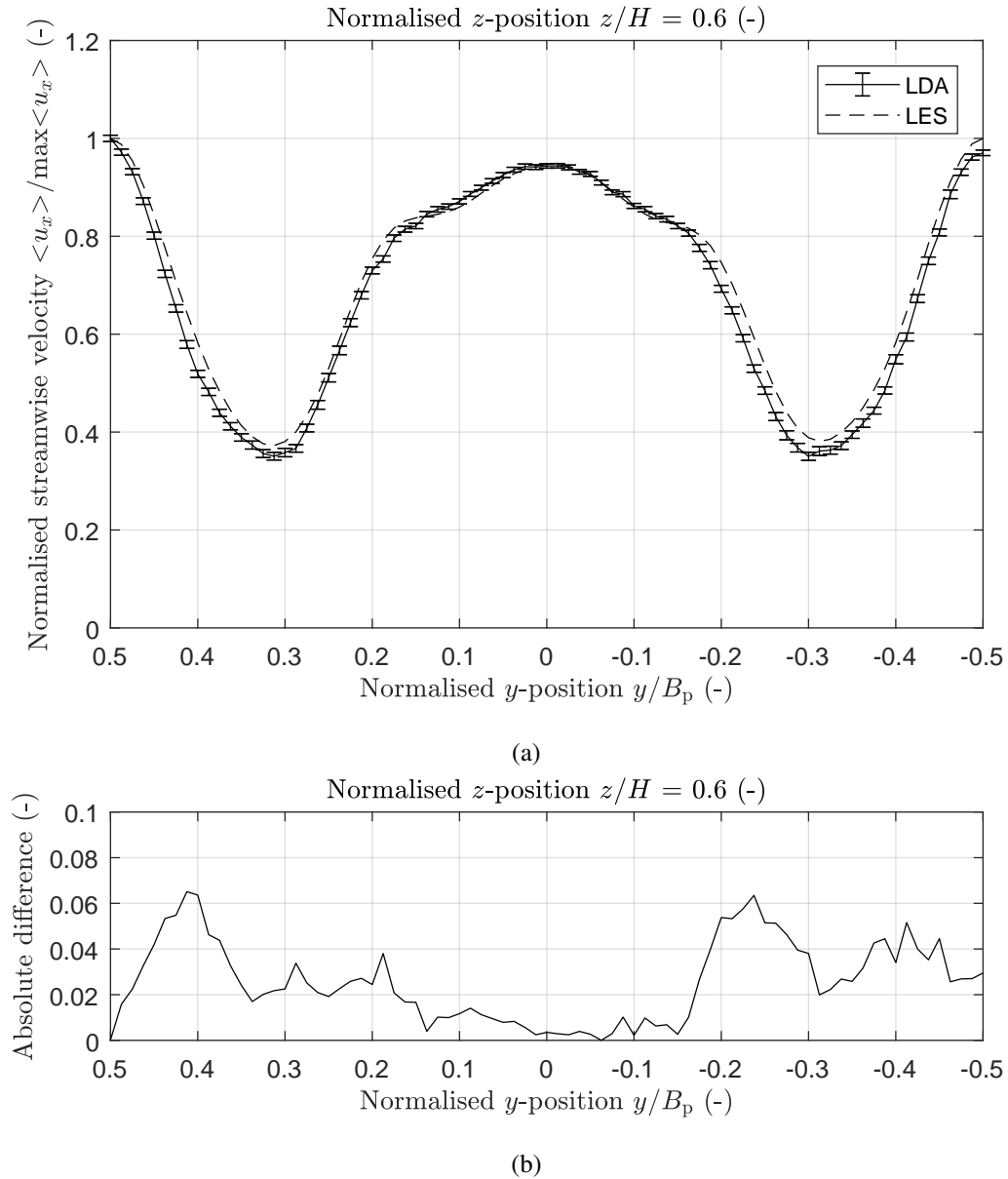
(a)

(b)

Figure 5.4. (a) Normalised time averaged streamwise velocity as function of normalised y-position at $z/H = 0.6$. The error bars are based on a 95 % confidence interval. (b) Absolute difference between the LDA and LES velocity profiles as function of normalised y-position at $z/H = 0.6$. Error bars are omitted for readability.
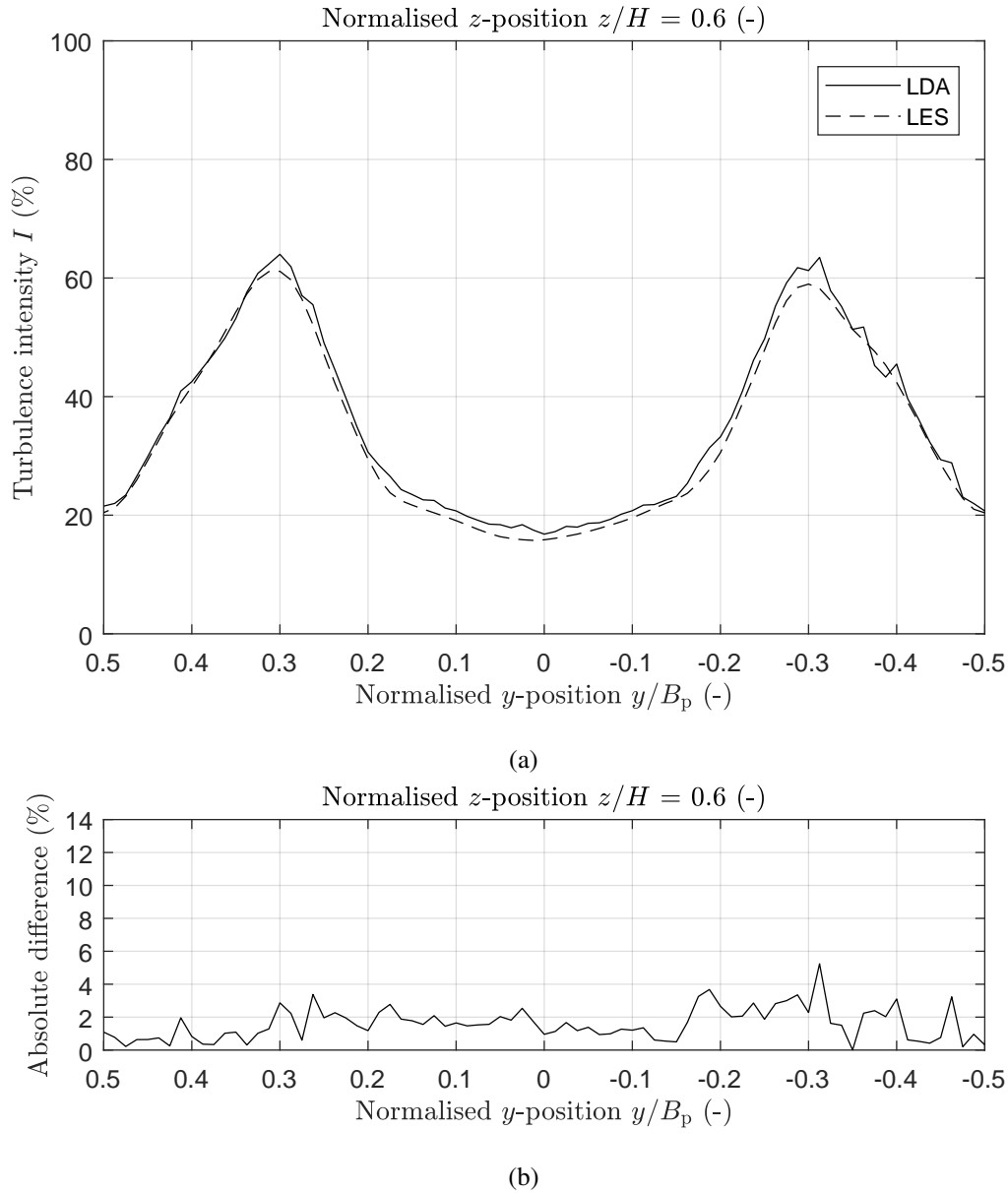
(a)

(b)

Figure 5.5. (a) Turbulence intensity as function of normalised y-position at $z/H = 0.6$. (b) Absolute difference between the LDA and LES turbulence intensity profiles as function of normalised y-position at $z/H = 0.6$.

Figures 5.2-5.5 show an overall good correspondence between the experiments and the LES simulations. To quantity the results, the largest and mean deviations for the velocity profiles in Figures 5.2 and 5.4 are presented in Table 5.1.

Parameter	Normalised z-position $z/H = 0.5$	Normalised z-position $z/H = 0.6$
Maximum deviation in percent	20.8 %	12.3 %
Mean deviation in percent	4.9 %	4.6 %

Table 5.1. Maximum and mean percentage deviation of the normalised streamwise velocity profiles from the LES simulations relative to the experiments. For $z/H = 0.5$ the maximum deviation is at $y/B_p = 0.3$. For $z/H = 0.6$ the maximum deviation is at $y/B_p = 0.4$.

The positions with the highest deviations are found to be in areas with high turbulence intensity. An area with high turbulence intensity is characterised by large velocity fluctuations. Furthermore, in this case the area with

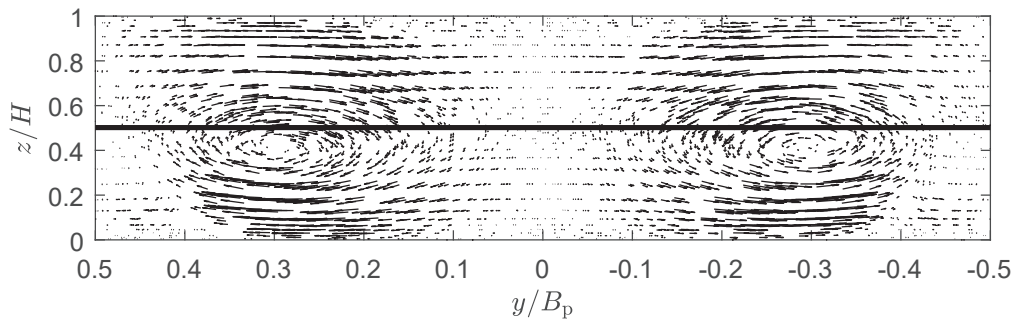high turbulence intensity is near the centres of the two main longitudinal vortices as seen in Figure 5.6.

Figure 5.6. Time averaged velocity vectors from LES in the y-z plane at $x/L_\mathrm{d} = 0$. The highlighted line shows one of the measurements profiles from the experiment.

In these areas there is a significant spatial velocity gradient resulting in a larger dispersion of velocities. Furthermore, due to the size of the LDA measuring volume, these areas are more likely to be affected by local velocity bias which is considered to be the main reason for the higher discrepancy. Additionally, the accuracy of the LDA system is also considered to affect the results. The system has not been calibrated recently for which reason the accuracy is considered to be in the order of 1 % (Dues and Neuer, 2016). The experimental uncertainties mentioned in Section 4.3 are considered to affect the results slightly, but since both the velocity and turbulent intensity profiles at two different positions show good correspondence, the LES setup is considered to resemble the flow phenomena in the channel. Therefore, the LES setup is used to conduct the parametric study where variations in longitudinal pitch distance and winglet height are investigated.

5.2   Numerical investigation of flow phenomena, heat transfer enhancement and pressure loss

In this section the influence on flow phenomena, heat transfer enhancement and pressure loss, due to variations in the longitudinal pitch distance and winglet height, are presented. The section is divided into four subsections with the first three subsections focusing on flow phenomena, heat transfer enhancement and pressure loss caused by the winglet pairs. The fourth part is a coupling between heat transfer enhancement and pressure loss in terms of performance resulting in an optimum configuration for the present study. The simulations are conducted on the ABACUS 2.0 supercomputer at *The University of Southern Denmark* in Odense. The supercomputer comprise of 584 nodes with a total of 14.016 CPU-cores yielding a theoretical maximum performance of 766 teraflop/s. The average simulation time for a single flow through of the domain, for the reference simulation with 2.2 million cells, a winglet height of $h/H = 0.5$, longitudinal pitch distance L_p/H = 5 and run on 48 CPU-cores, is 10070 seconds equal to 2 hours and 48 minutes. In general, 24 CPU-cores are allocated per million cells.

Throughout this chapter, a variety of cross sections are shown. The locations are shown in Figure 5.7 for reference.
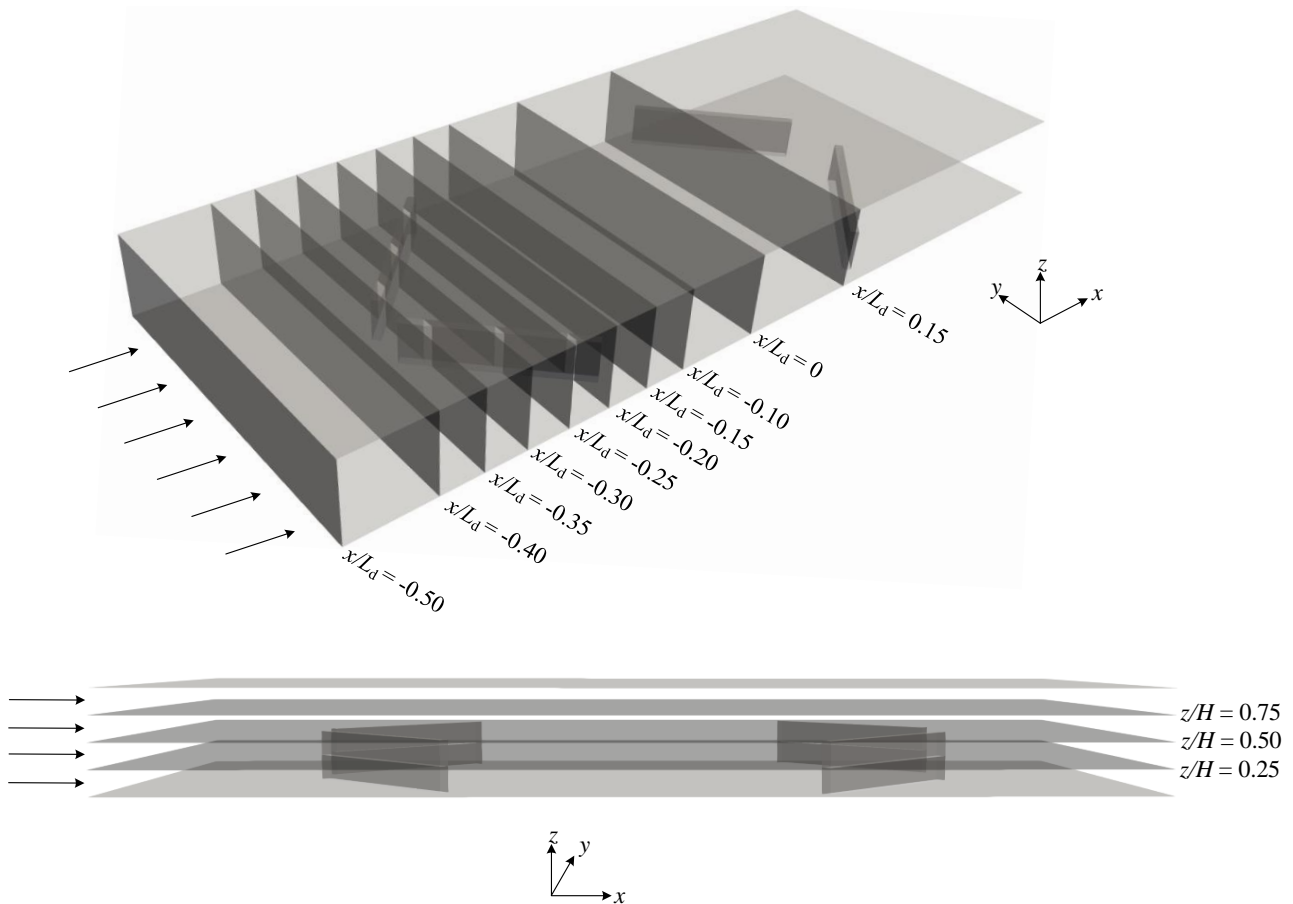
Figure 5.7. Locations of the different cross sections shown throughout this chapter. The upper figure show the y-z cross sections and the bottom figure show the y-z cross sections. The arrows indicate flow direction.

5.2.1 Flow characteristics

To understand the resulting heat transfer and pressure losses caused by the winglet pairs, the overall flow characteristics are described. These characteristics are extracted from the LES simulation with 2.2 million cells chosen in the grid convergence study in Chapter 3.5 which was experimentally validated in Section 5.1 above. The main flow phenomena of interest are the different kinds of vortex structures created by the winglets pairs. Generally, three different kinds of vortex structures; main longitudinal vortices, corner vortices and induced vortices are used for distinction.

The main mechanism for the generation of vortices is an adverse pressure gradient across the top of the winglet leading to flow separation and subsequent interaction with the main flow which is driven by a favourable pressure gradient. To illustrate the vortices generated by the winglets, iso-contours of the swirling strength, λ, are shown in Figure 5.8. The swirling strength is defined as the inverse of the time for the fluid to rotate once about its rotational axis. This means that $\lambda = 0$ corresponds to no circular motion and thus $\lambda > 0$ corresponds to eddy motion (Adrian et al., 2000).
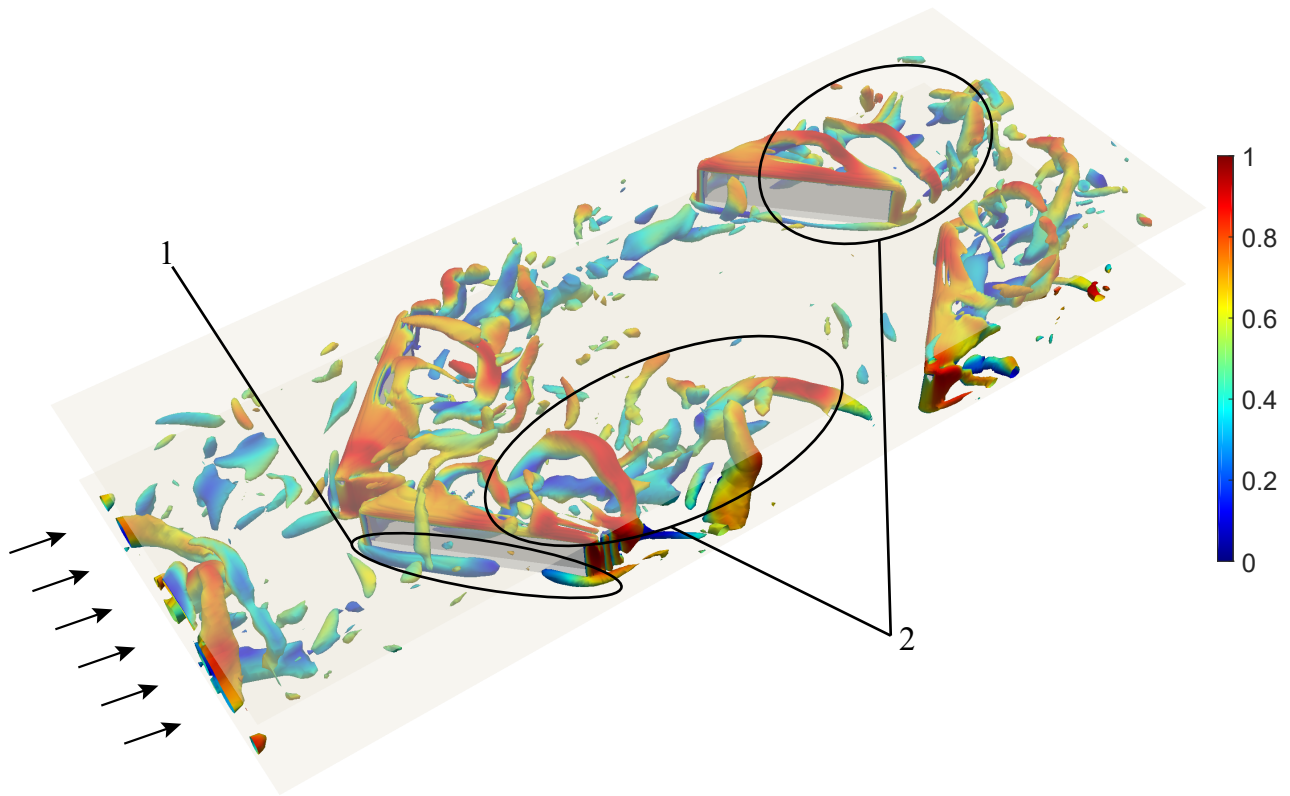
Figure 5.8. 3D iso-contours of the swirling strength λ, coloured with the normalised instantaneous velocity magnitude. The domain configuration is with a normalised winglet height of $z/H = 0.5$ and a normalised longitudinal pitch distance of $L_{\mathrm{p}}/H = 5$. The normalisation is done relative to the maximum value in the domain as $|u|/\max|u|$. The iso-contours with a small swirling strength are not shown.

To show the different kinds of vortices, different regions in Figure 5.8 are marked. Marking number 1 shows the formation of corner vortices, which are vortices created in the lower region along the wall of the winglet. Corner vortices form because a pressure gradient occur towards the bottom of the channel. As the fluid approaches stagnation near the winglet it slows down and the pressure increases. Since the velocity closer to the bottom wall is lower, the pressure increase is lower in this region compared to a region just above it. Thus this pressure gradient causes a flow towards the bottom wall which interacts with the main flow. Consequently the fluid rolls up forming vortices which are swept around the winglet base and carried downstream.

Marking number 2 shows a larger vortex structure that originates from the flow separation over the winglets. Immediately behind the winglets a larger intercoiling vortex structure is formed. This structure forms the basis for the main longitudinal vortex which continues in the downstream region of the winglets and thus is the main contributor to global heat transfer enhancement in the channel. To further visualise the creation and downstream movement of the main longitudinal vortices, a 3D view with the average velocity streamlines showing the fluid movement throughout the domain is presented in Figure 5.9. It is observed how the fluid move over and around the winglets which creates the two main longitudinal vortices. A closer look from behind the first winglet pair is shown in Figure 5.10.
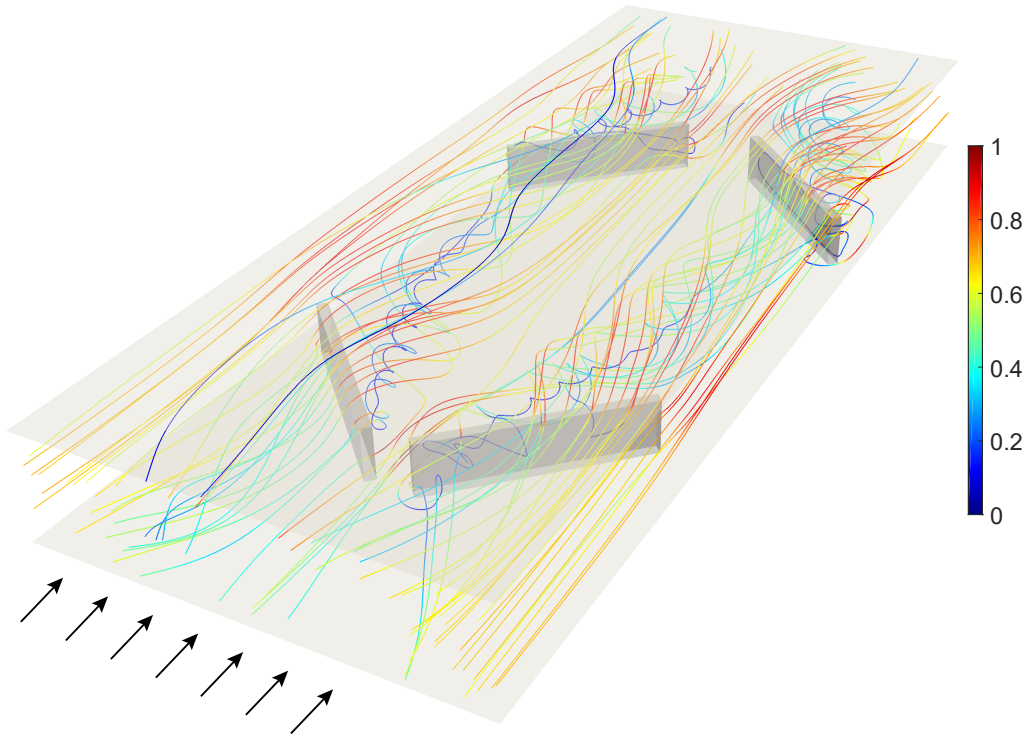
Figure 5.9. Time averaged normalised velocity streamlines throughout the computational domain. The domain configuration is with a normalised winglet height of $z/H = 0.5$ and a normalised longitudinal pitch distance of $L_\mathrm{p}/H = 5$. The normalisation of the velocity is done relative to the maximum value in the domain as $<|u|>/\mathrm{max}<|u|>$.
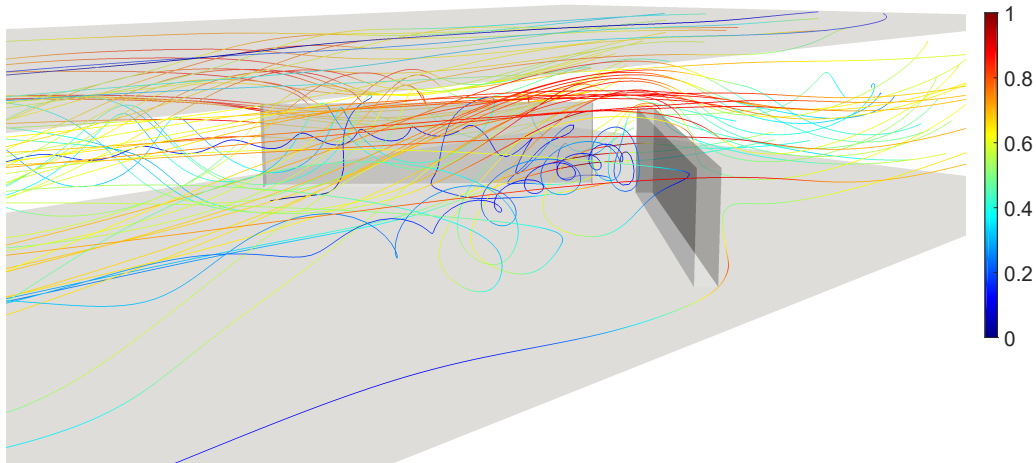

Figure 5.10. Time averaged normalised velocity streamlines seen from behind the first winglet pair showing the longitudinal vortex generated by the winglet. The domain configuration is with a normalised winglet height of $z/H = 0.5$ and a normalised longitudinal pitch distance of $L_\mathrm{p}/H = 5$. The normalisation of the velocity is done relative to the maximum value in the domain as $<|u|>/\mathrm{max}<|u|>$.

To understand the mechanisms associated with the vortex structures, shown in the above figures, velocity, pressure and temperature contours are shown in Figure 5.11 and 5.12 for different z-positions. For reference, the positions are illustrated in Figure 5.7. In Figure 5.11, time averaged contours for the velocity magnitude, pressure and temperature are shown. In Figure 5.12, RMS contours for the streamwise (x), spanwise (y) and vertical (z) velocities are shown. Each of the parameters are normalised with the corresponding maximum global value in the domain.
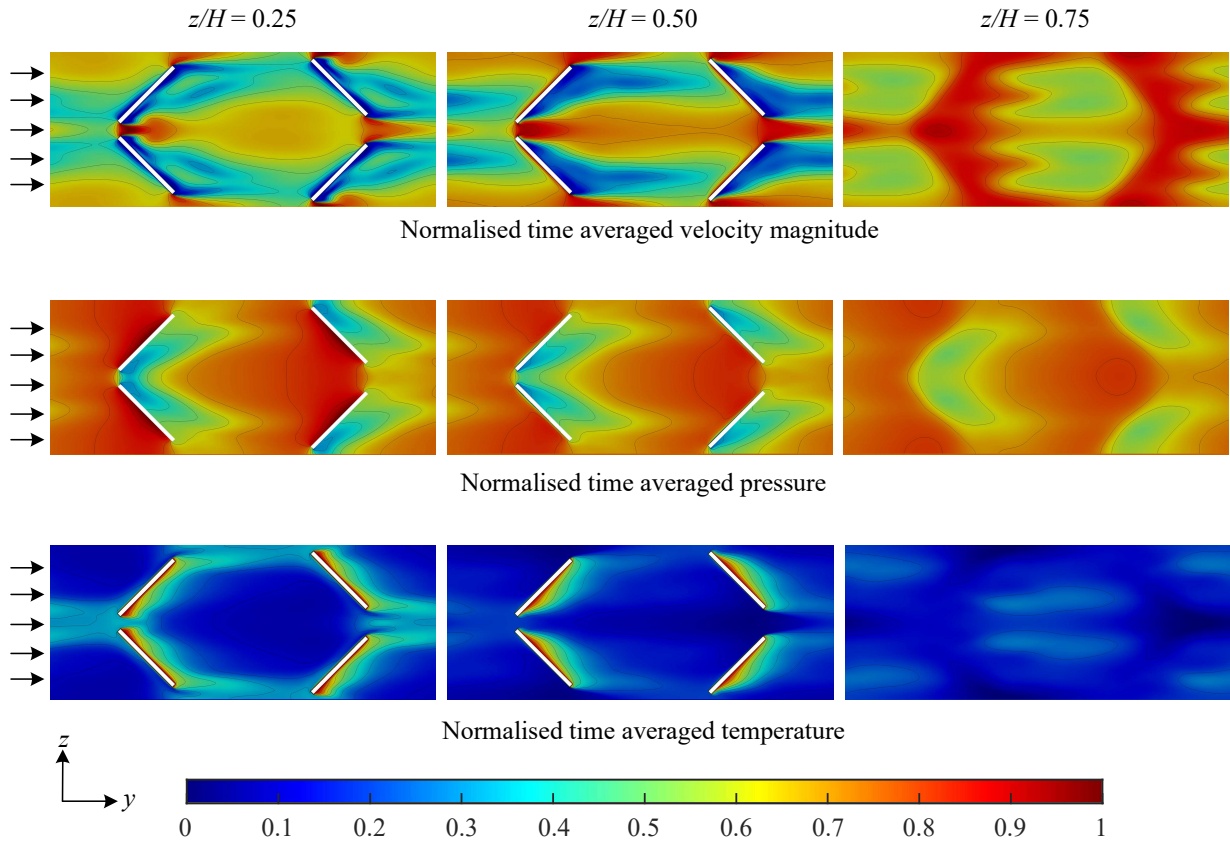
Figure 5.11. Normalised time averaged velocity magnitude, pressure and temperature. The domain configuration is with a normalised winglet height of $z/H = 0.5$ and a normalised longitudinal pitch distance of $L_{\mathrm{p}}/H = 5$. All parameters are normalised with the global maximum values of the domain. The normalisation is as follows: $<|u|>/\mathrm{max}<|u|>$ for velocity, $<p>/\mathrm{max}<p>$ for pressure and $<T>/\mathrm{max}<T>$ for temperature. Contour lines are displayed with an interval of 0.1.

It is evident that the velocity downstream of the winglets is lower at $z/H = 0.50$ than at $z/H = 0.25$. This is in agreement with the fact that separation occurs at the top of the winglet. At this point the pressure is high, resulting in the flow moving towards the low pressure regions above and behind the winglets. The flow moving above the winglets is accelerated, then decelerated in the free stream region and accelerated again across the second winglet pair. This is in agreement with the pressure contour. Furthermore, this indicates a lower degree of turbulence which explains the lower temperature in the upper region of the channel. The pressure behind the winglets is lower at $z/H = 0.25$ compared to $z/H = 0.50$. This indicates that the flow is moving towards the lower wall explaining the vortex structures formed in Figures 5.9 and 5.10. Consequently, the temperature is higher in the lower part of the channel due to the wall normal mass transport of higher temperature fluid.

The RMS velocities shown in Figure 5.12 indicate the location of the main longitudinal vortices and the corner vortices. Looking at the first winglet pair, there are regions with larger velocity fluctuations immediately behind the winglets and around the winglets toward the sides of the domain. The smaller fluctuation regions around the winglets suggest the formation of corner vortices, mainly in the lower part of the channel. The larger fluctuation regions behind the winglets indicate the formation of the main longitudinal vortices. The magnitude of the fluctuations are higher in the $z/H = 0.50$ plane indicating that the cores of the vortices are located in close proximity of this area. Furthermore, the fluctuations persist all the way down to the second winglet pair after which the same tendencies recur.
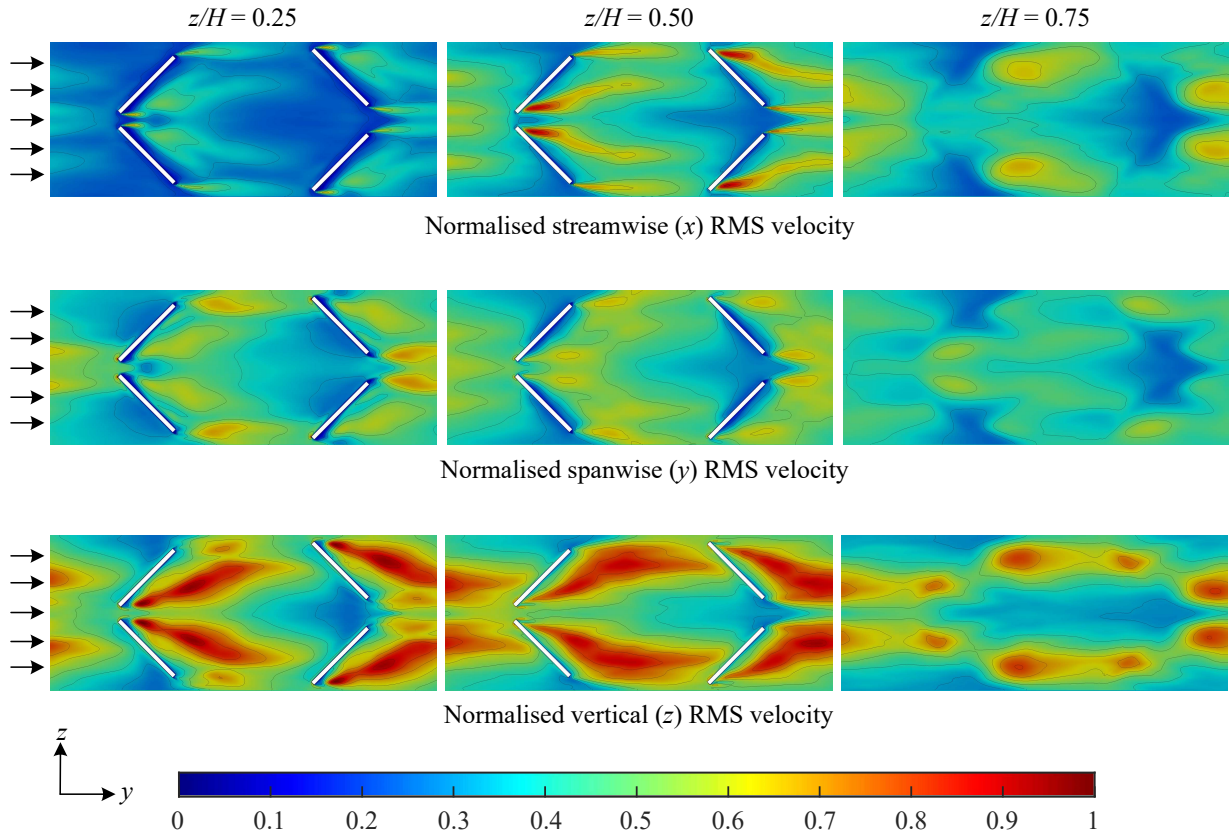
$z/H = 0.25$ $z/H = 0.50$ $z/H = 0.75$

Normalised streamwise (x) RMS velocity

Normalised spanwise (y) RMS velocity

Normalised vertical (z) RMS velocity

Figure 5.12. Normalised RMS velocity in the streamwise (x), spanwise (y) and vertical (z) direction. The domain configuration is with a normalised winglet height of $z/H = 0.5$ and a normalised longitudinal pitch distance of $L_\mathrm{p}/H = 5$. All parameters are normalised with the global maximum values of the domain. The normalisation is as follows: $u_{x,\mathrm{RMS}}/\mathrm{max}(u_{x,\mathrm{RMS}})$ for x-direction, $u_{y,\mathrm{RMS}}/\mathrm{max}(u_{y,\mathrm{RMS}})$ for y-direction and $u_{z,\mathrm{RMS}}/\mathrm{max}(u_{z,\mathrm{RMS}})$ for z-direction. Contour lines are displayed with an interval of 0.1.

Streamlines in the y-z plane for different x-positions starting from the inlet to the middle of the domain are shown in Figure 5.13. The locations are the first nine cross sections highlighted in Figure 5.7. The development of the flow from the inlet, across the winglets and to the middle of the domain is shown. The planes are coloured with the magnitude of the normalised time averaged y-z velocities. Generally it is seen that as the flow crosses the winglets, the initial vortices are broken down. Afterwards, their rotational direction are reversed, forming a new pair of counter rotating longitudinal and corner vortices immediately downstream of the winglets. The main longitudinal vortices occupy most of the domain width and their cores are located in close proximity of the middle z-position of the channel, $z/H = 0.50$. Furthermore, the vortices move towards the sides of the domain downstream of the winglets and their strength decrease in the streamwise direction. However, the vortices do persist all the way to the following winglet pair. These observations are all in agreement with the above figures and discussions.
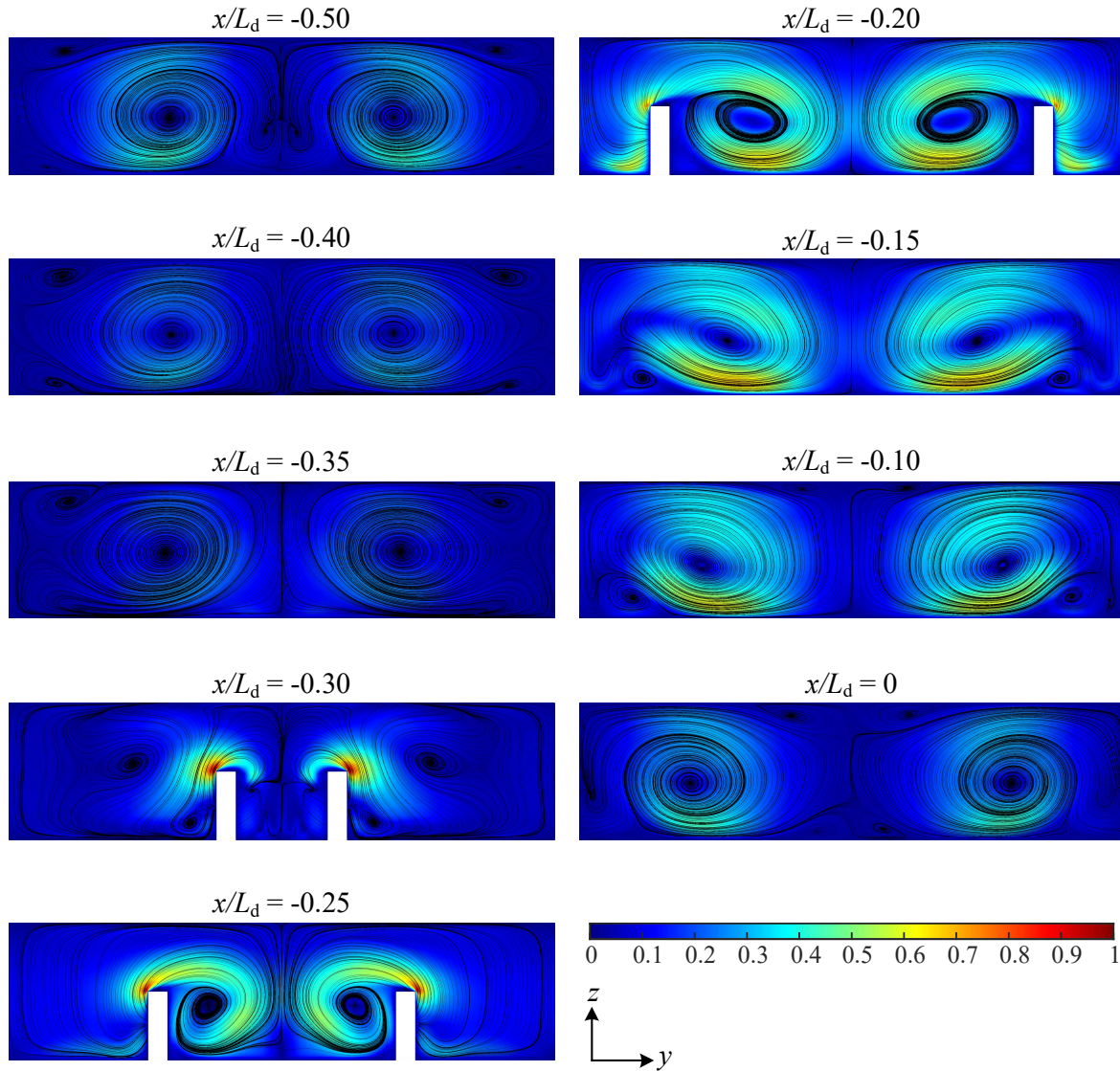
Figure 5.13. Normalised time averaged y-z velocity streamlines showing the development of the flow going from the inlet of the domain down to the middle of the domain. The domain configuration is with a normalised winglet height of $z/H = 0.5$ and a normalised longitudinal pitch distance of $L_p/H = 5$. The cross sections are coloured with the magnitude of the normalised time averaged y-z velocities. The normalisation is made relative to the maximum value in the domain as $<|u_y+u_z|>/\max<|u_y+u_z|>$. The contours are shown in larger format in Appendix F.

5.2.2 Heat transfer enhancement

The heat transfer enhancement from the various simulations are summed up in Figure 5.14 which shows Nusselt number enhancement contours as function of the normalised winglet height and longitudinal pitch. The Nusselt number is calculated as in equation (3.11) which is restated below.

$$\mathrm{Nu} = -\frac{\mathrm{d}T}{\mathrm{d}n}\frac{H}{\Delta T}$$

The reference Nusselt number, $\mathrm{Nu_0}$, is calculated using the domain shown in Figure 5.1 without winglets but with periodic boundary conditions in the streamwise and spanwise direction.
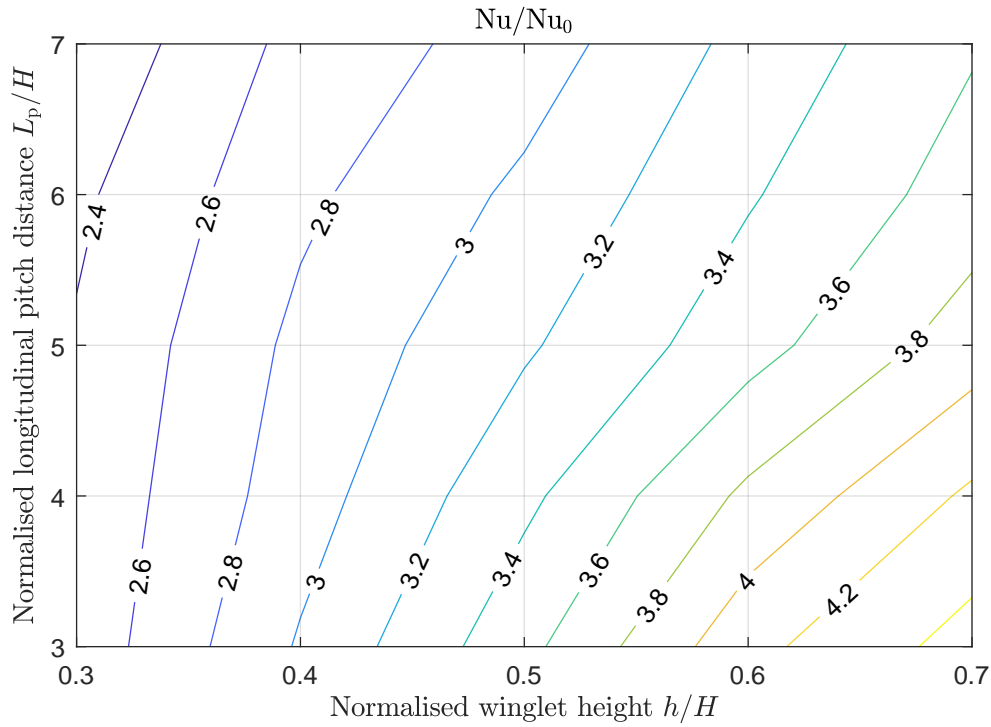
Figure 5.14. Heat transfer enhancement as function of normalised longitudinal pitch distance L_p/H, and normalised winglet height h/H.

It is evident that the heat transfer enhancement decreases with longitudinal pitch and increases with winglet height. As expected, the heat transfer enhancement approaches 1 as the normalised winglet height approaches 0 and as the normalised longitudinal pitch distance approaches infinity. An increase in winglet height shows to have the largest effect on the heat transfer enhancement. Furthermore, the slope of the contour lines decrease with increasing winglet height suggesting that the longitudinal pitch has a larger effect on the heat transfer enhancement with a high winglet height. These tendencies are further examined by the use of Figure 5.15 where time averaged wall normal temperature gradients are shown for two different configurations. The first configuration is with the largest longitudinal pitch and lowest winglet height and the second configuration is with the largest longitudinal pitch and highest winglet height. The wall normal temperature gradients are shown for both the lower and upper wall.
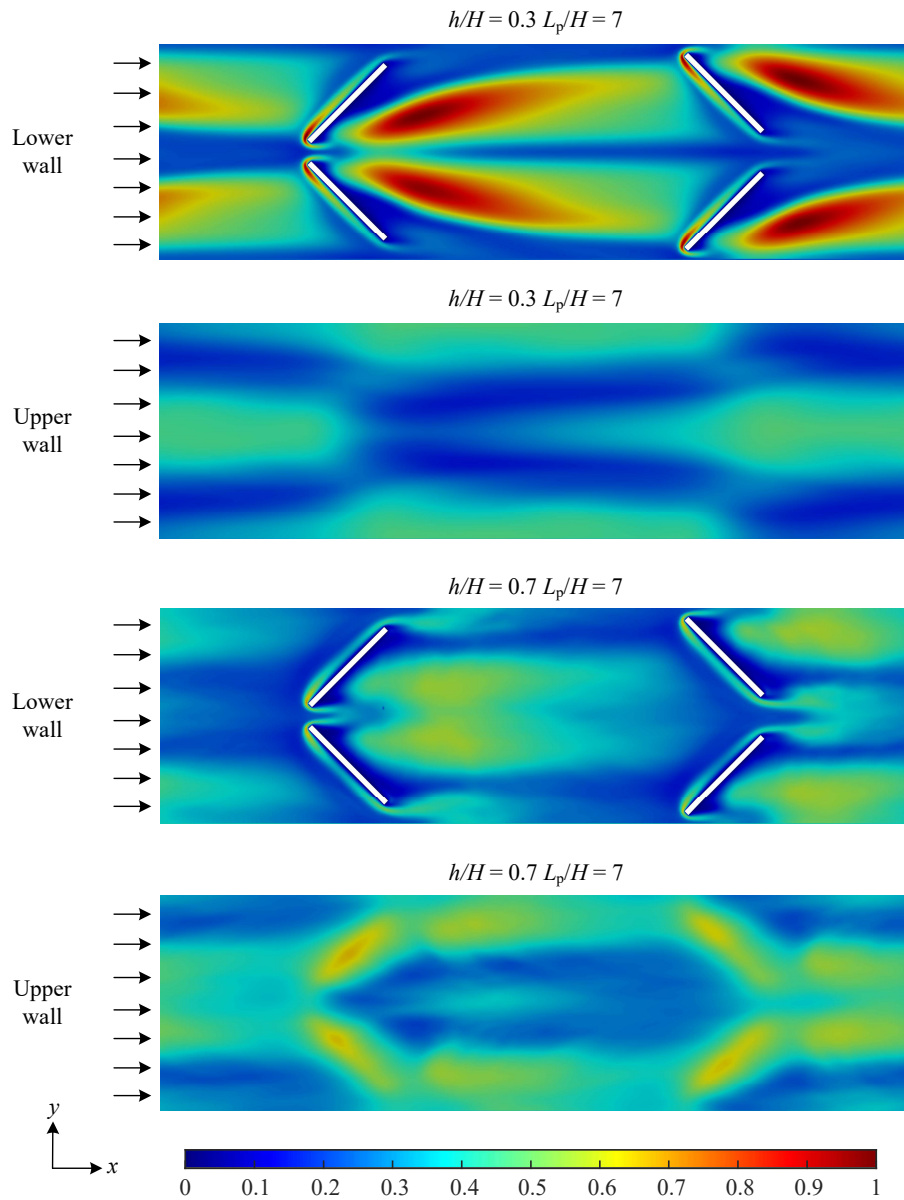
Figure 5.15. Normalised time averaged wall normal temperature gradient for the lower and upper wall. The first two contours are for a normalised winglet height and longitudinal pitch distance of $h/H = 0.3$ and $L_p/H = 7$, respectively. The two last contours are for a normalised winglet height and longitudinal pitch distance of $h/H = 0.7$ and $L_p/H = 7$, respectively. The normalisation is done relative to the maximum value of the upper and lower wall as $<\mathrm{d}T/\mathrm{d}n>/\max<\mathrm{d}T/\mathrm{d}n>$.

In each of the lower wall contours, a high temperature gradient is observed along the upstream side of the winglet which is where the corner vortices occur. The most significant gradients are observed in the regions of the main longitudinal vortices downstream of the winglets. Furthermore, the case of the low winglet height shows a higher gradient along the lower wall and a lower gradient along the upper wall. This indicates that the main longitudinal vortices are located closer to the lower wall. For the high winglet case the gradient is more evenly distributed between the lower and upper wall. This indicates that the main longitudinal vortices are located closer to the middle of the channel. To examine the flow structure and temperature fields associated with the temperature gradients, time averaged streamlines, velocity vectors and temperature contours are shown for both cases at different positions downstream of the winglets. The positions are shown in Figure 5.7.
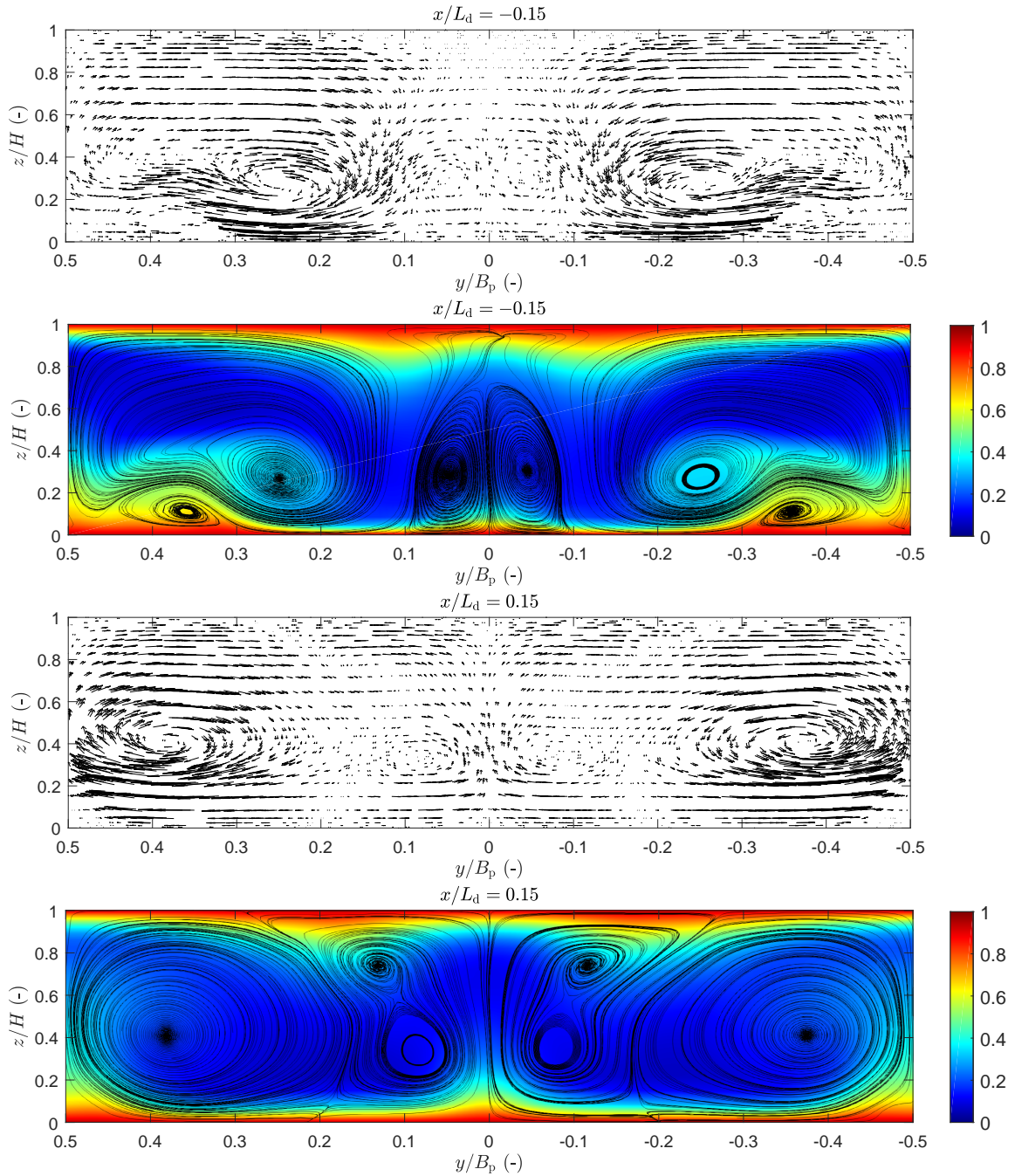
Figure 5.16. Normalised time averaged velocity vector field and streamlines with normalised temperature contours at normalised streamwise position $x/L_\mathrm{d} = \pm 0.15$ in the y-z-plane. The domain configuration is with a normalised winglet height and longitudinal pitch distance of $h/H = 0.3$ and $L_\mathrm{p}/H = 7$, respectively. The normalisation is done relative to the maximum value in the domain as $<|u_y+u_z|>/\mathrm{max}<|u_y+u_z|>$ and $<T>/\mathrm{max}<T>$.

For the low winglet height shown in Figure 5.16, which is the case with the lowest heat transfer enhancement, it is evident that the main longitudinal vortices do not show a high degree of interaction with the thermal boundary layer in the upper channel wall region. This means that the thermal boundary layer at the upper channel wall remain as the flow is moving downstream. Furthermore, the figures indicate that the main longitudinal vortices and induced vortices have the biggest impact on heat transfer enhancement due to mixing between the core flow and the thermal boundary layer region. The vector fields indicate that the corner and induced vortices

are of small magnitude compared to the main longitudinal vortex. As the flow moves downstream the main longitudinal vortices move outwards and away from the bottom channel wall and the corner vortices gets dissipated due to viscous forces. This causes a greater boundary layer to core flow mixing in the lower wall region and thus a higher heat transfer enhancement. Furthermore, the main longitudinal vortices maintain their magnitude downstream which comply with the fact that at the lower winglet height the heat transfer enhancement is relatively insensitive to the longitudinal pitch as seen in Figure 5.14.
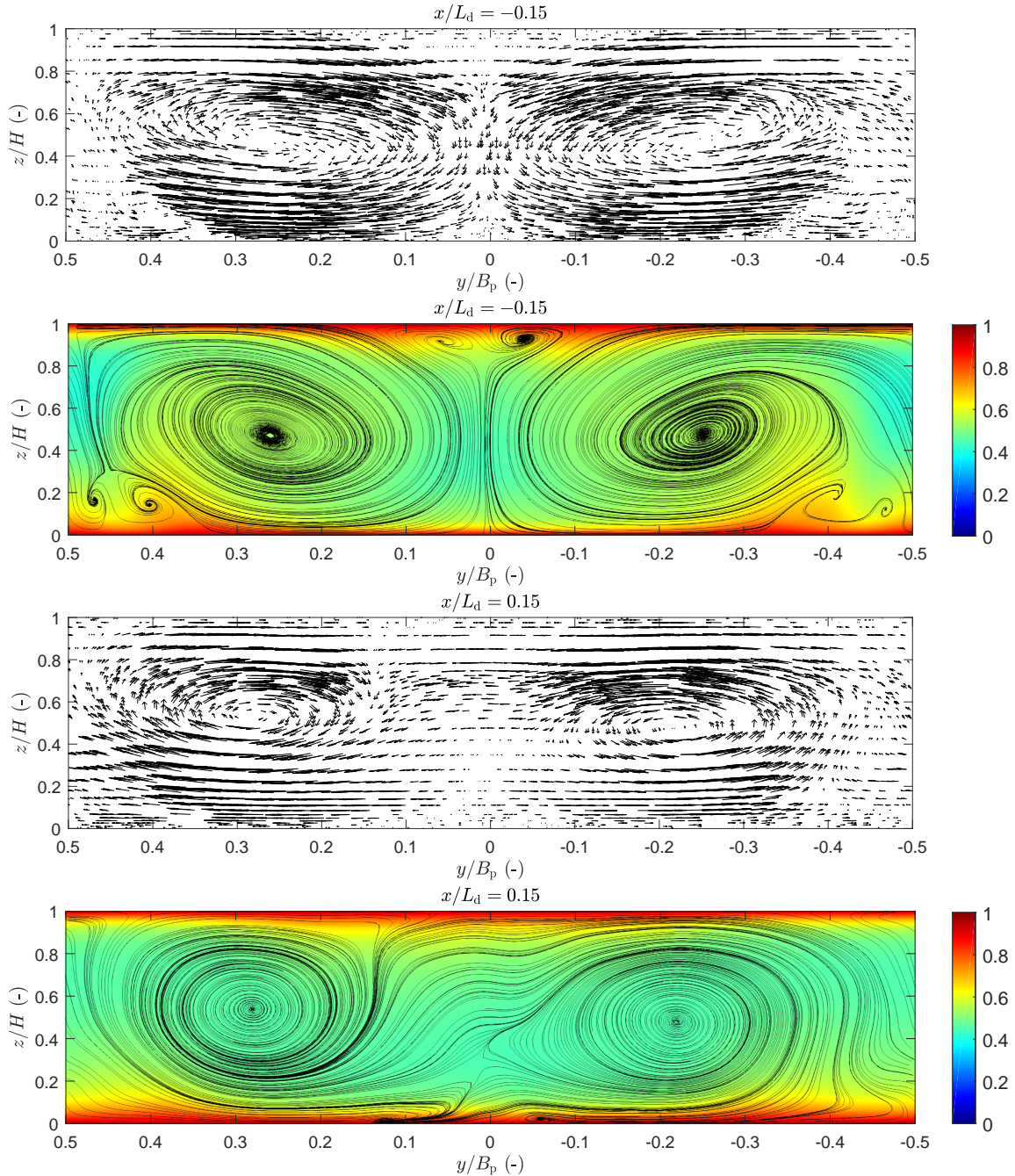
Figure 5.17. Normalised time averaged velocity vector field and streamlines with normalised temperature contours at normalised streamwise position $x/L_\mathrm{d} = \pm 0.15$ in the y-z-plane. The domain configuration is with a normalised winglet height and longitudinal pitch distance of $h/H = 0.7$ and $L_\mathrm{p}/H = 7$, respectively. The normalisation is done relative to the maximum value in the domain as $<|u_y+u_z|>/\max<|u_y+u_z|>$ and $<T>/\max<T>$.

For the high winglet height shown in Figure 5.17, it is evident that the main longitudinal vortices show a high degree of interaction with the lower and upper thermal boundary layers, and thus yield a high heat transfer enhancement. Due to the higher degree of mixing the bulk temperature is higher, compared to the low winglet case. The corner vortices and the induced vortices are of low significance, since none of them are present in the latter position. The magnitude of the main longitudinal vortices decrease significantly in the streamwise direction due to the interaction with the upper and lower wall. This comply with the fact that the heat transfer enhancement is highly dependent on the longitudinal pitch at a high winglet height as seen in Figure 5.14.

5.2.3 Pressure loss

The pressure loss from the various simulations are summed up in Figure 5.18 which shows contours for the increase in loss coefficient as function of the normalised winglet height and longitudinal pitch. The loss coefficient is calculated as in equation (3.14) which is restated below.

$$f = \frac{H}{0.5\rho u_{\text{bulk}}^2} \frac{\mathrm{d}P}{\mathrm{d}x}$$

The reference loss coefficient, f_0, is calculated using the domain shown in Figure 5.1 without winglets but with periodic boundary conditions in the streamwise and spanwise direction.
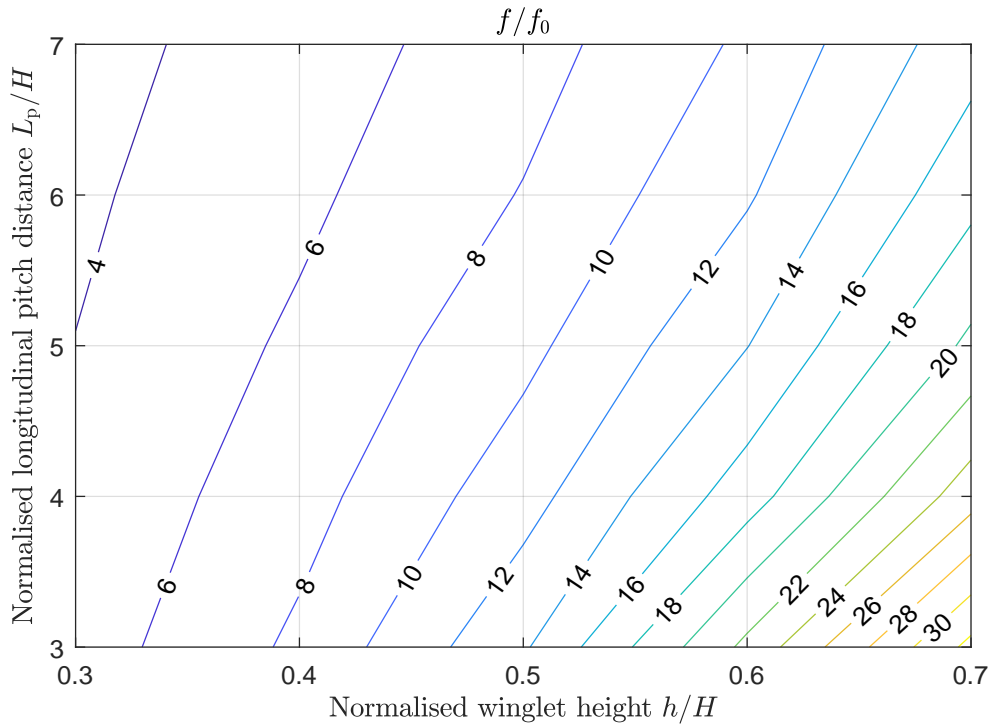

Figure 5.18. Increase in loss coefficient as a function of normalised longitudinal pitch distance L_{p}/H and normalised winglet height h/H.

As expected, the loss coefficient ratio approaches 1 as the normalised winglet height approaches 0 and as the normalised longitudinal pitch distance approaches infinity. The increase in loss coefficient shows a similar tendency to the heat transfer enhancement in Figure 5.14, where the loss coefficient is highest at a large winglet height and small longitudinal pitch. Similarly, it is seen that the dependency on longitudinal pitch is highest at large winglet heights. This is due to the higher pressure drag caused by the larger winglet area and resulting wake region. The wake regions behind two different configurations with the same longitudinal pitch and different winglet heights are shown in Figure 5.19.

$h/H = 0.3, L_\mathrm{p}/H = 7$
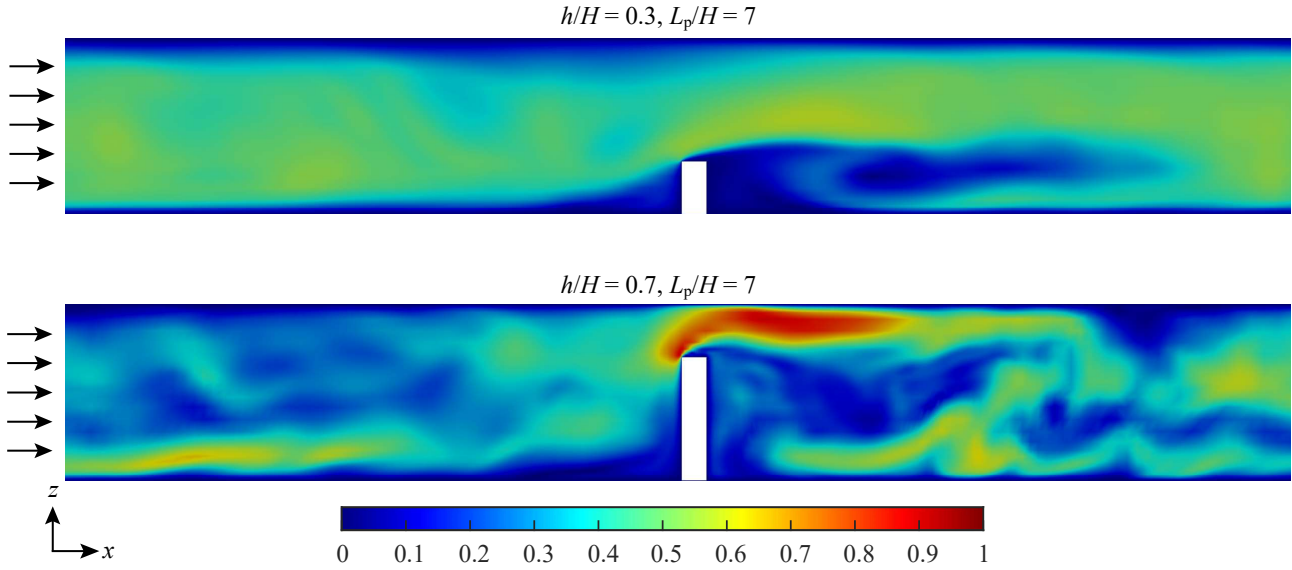

$h/H = 0.7, L_\mathrm{p}/H = 7$

Figure 5.19. Normalised instantaneous velocity magnitude of the flow across the lowest ($h/H = 0.3$) and the highest winglet ($h/H = 0.7$) for a longitudinal pitch distance of $L_\mathrm{p}/H = 7$. The cross sections show a side view of the first half of the channel at the middle part of the winglet at $y/B_\mathrm{p} = -0.25$. The normalisation is done relative to the maximum value in the domain as $<|u|>/\mathrm{max}<|u|>$.

It is seen from Figure 5.19 that a larger wake region with a higher degree of turbulence is formed behind the high winglet. This complies with the fact that the pressure drag is significantly larger for the higher wing compared to the lower wing. Furthermore, the larger vortex structures in the wake region of the higher winglet diminishes downstream, indicating that the degree of turbulence at the next winglet pair is highly dependent on the longitudinal distance. This is further examined by the use of Figures 5.20 and 5.21 which show the swirling strength for two configurations with the same winglet height but with different longitudinal pitch. At a small longitudinal pitch, the vortices formed by the first winglet pair are present all the way down to the second winglet pair. This increases the degree of turbulence in front of the second winglet pair. Due to the staggered arrangement, the rotational direction is reversed across the winglets resulting in increased fluid mixing and consequently leading to a higher degree of turbulence in the wake region of the second winglet pair. It is evident from Figure 5.21, that the opposite is true for the longer longitudinal pitch i.e. the vortex structures created by the first winglet pair are diminished before reaching the second winglet pair.

Figure 5.20. Iso-contours of the swirling strength λ, coloured with the normalised instantaneous velocity magnitude. The normalisation is done relative to the maximum value in the domain as $|u|/\mathrm{max}|u|$. The domain configuration is with a normalised winglet height of $z/H = 0.7$ and a normalised longitudinal pitch distance of $L_\mathrm{p}/H = 4$. The iso-contours with a small swirling strength are not shown.
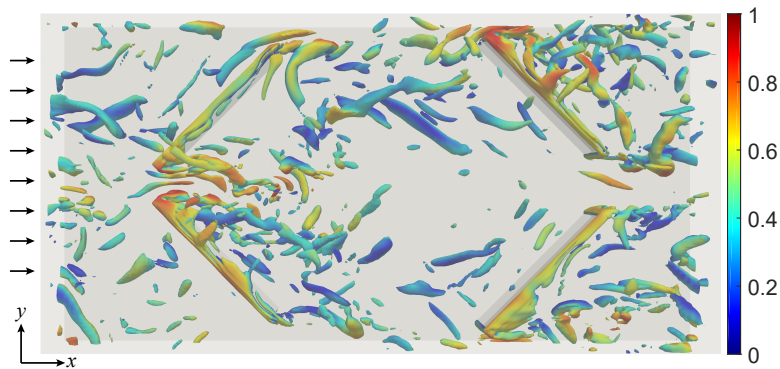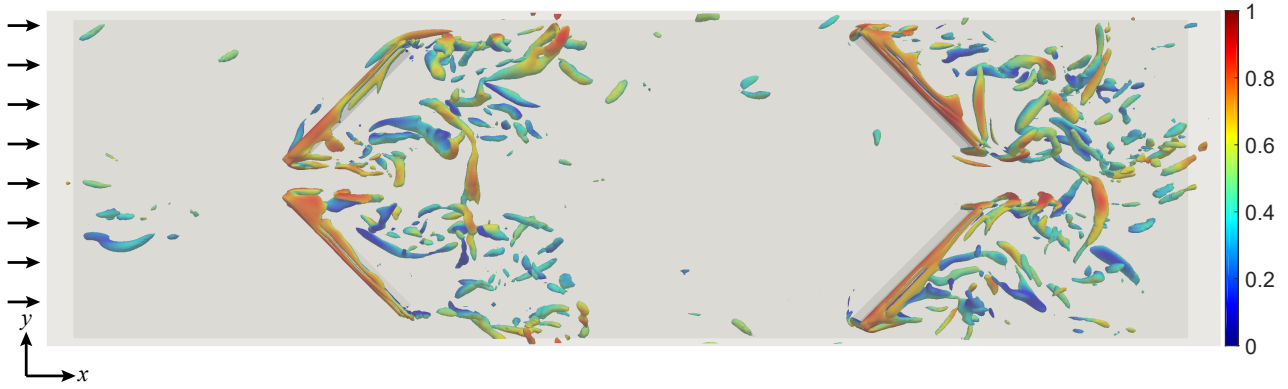
Figure 5.21. Iso-contours of the swirling strength λ, coloured with the normalised instantaneous velocity magnitude. The normalisation is done relative to the maximum value in the domain as $|u|/\max|u|$. The domain configuration is with a normalised winglet height of $z/H = 0.7$ and a normalised longitudinal pitch distance of $L_{\mathrm{p}}/H = 7$. The iso-contours with a small swirling strength are not shown.

The aforementioned phenomena are additionally supported by the pressure distributions across the first pair of winglets shown in Figure 5.22. The figures show the time averaged pressure distribution around the first winglet pair for the configurations shown in Figures 5.20 and 5.21. According to the discussion above, the pressure difference should be higher across the winglet pair in the short longitudinal pitch configuration compared to the long longitudinal pitch. This is evidenced by the fact that the pressure difference across the winglet pair in the short pitch distance configuration is approximately double relative to the pressure difference in the long pitch distance configuration.
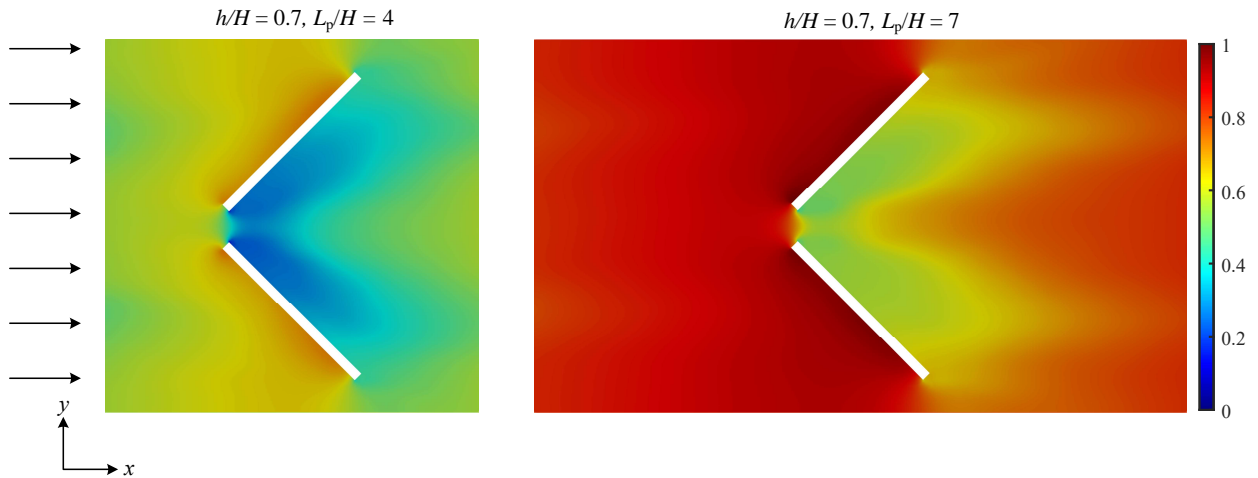
Figure 5.22. Normalised time averaged pressure distribution around the first winglet pair for the configurations shown in Figures 5.20 and 5.21. The normalised winglet heights are equal at $h/H = 0.7$ and the normalised longitudinal pitch distances are $L_{\mathrm{p}}/H = 4$ and $L_{\mathrm{p}}/H = 7$, respectively. The cross sections depict the first half of the domain at half the channel height, $z/H = 0.5$. The normalisation is done relative to the maximum value in the domain as $<p>/\max<p>$.

5.2.4 Heat transfer performance

For evaluating the heat transfer performance, the performance parameter, η, is used. The performance parameter is used as a measure of how well each configuration performs in terms of heat transfer enhancement relative to pressure loss and is calculated as in equation (3.15) which is restated below.

$$\eta = \frac{\mathrm{Nu}/\mathrm{Nu_0}}{(f/f_0)^{1/3}}$$

The heat transfer performance as a function of normalised winglet height and longitudinal pitch distance is shown as contour regions in Figure 5.23.
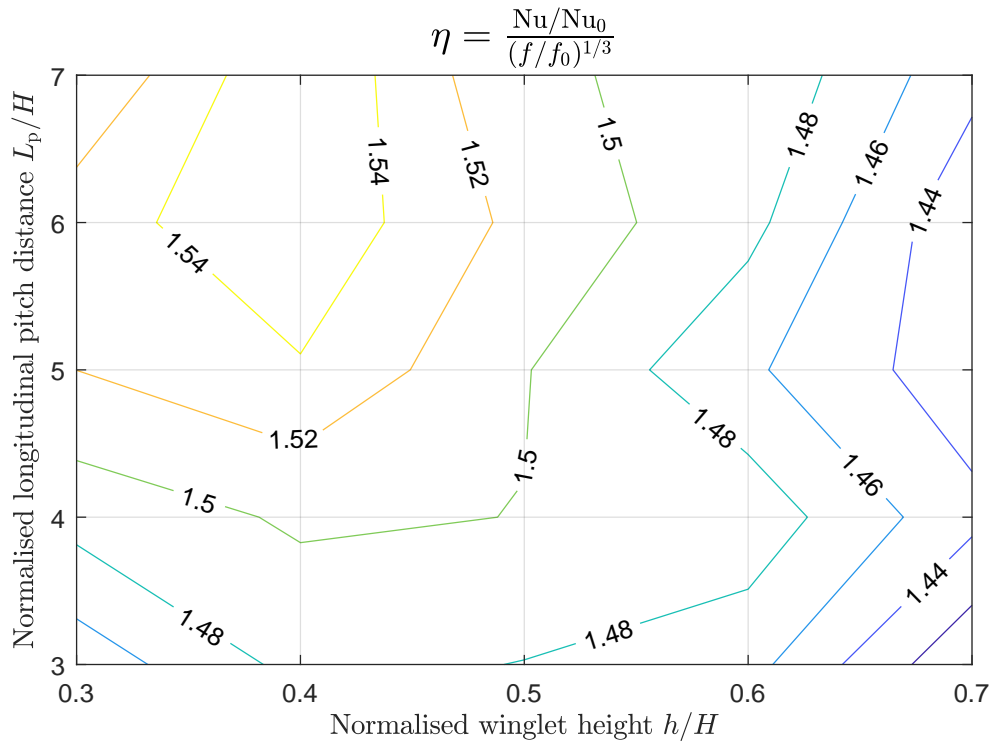

Figure 5.23. Heat transfer performance as function of normalised longitudinal pitch and winglet height.

For the present study, the configuration with a winglet height of $h/H = 0.4$ and a longitudinal pitch of $L_p/H = 7$ shows the highest heat transfer performance. The lower winglet height and high longitudinal pitch suggest a low pressure drag across the winglets resulting in a smaller wake region behind the winglets. This implies that the formed vortices diminishes in strength downstream to a point in which their affect on the flow across the following winglet pair is low. Furthermore, this configuration indicates that the main longitudinal vortices do have a good interaction with the thermal boundary layer resulting in a high degree of mixing with the core flow and thereby a stable heat transfer enhancement through the domain. Further discussion of the results are conducted in the following section.

5.3 Summary and discussion of the results

Through the numerical investigations it is evident that by introducing winglet vortex generators into a fully developed channel flow, different kinds of vortex structures are generated. Three different types of vortices, namely corner, induced and main vortices are distinguished. The corner vortices are generated at the lower wall on the upstream side of the winglets due to a stagnation of the at the winglets resulting in a downwards pressure gradient. These vortices move along the winglet and into the downstream longitudinal direction and are dissipated further downstream due to viscous interaction. The main longitudinal vortices are generated due to flow separation over the winglets. These vortices are large in structure and persistent well downstream of the winglets.

All of the three types of vortices show to interact with the thermal boundary layer, which results in enhanced heat transfer. This is due to an increased degree of mixing of the thermal boundary layer with the core flow. The degree of mixing is highly dependent on the size and location of the vortex, which causes the larger main

longitudinal vortex structures to have a higher boundary layer to core flow mixing. As the corner and induced vortices due not span from boundary layer to core flow, the effect on heat transfer is smaller compared to that of the larger vortices.

The size and persistence of the generated vortices are much affected by the height of the winglets. At small winglet heights the main longitudinal vortices are of smaller size and strength and have a smaller degree of boundary layer interaction. Due to the smaller size and strength, the corner and induced vortices have a higher relative impact on the heat transfer enhancement. At large winglet heights the main longitudinal vortices are larger in size and strength and are the dominant ones as they cause a faster dissipation of the smaller vortices. The higher degree of boundary layer interaction results in the vortices being less persistent downstream. Thereby, the larger vortices created by the large winglets are more affected by the longitudinal distance between the winglet rows. This is not the case for the small vortices created by the small winglets, as they are more persistent downstream.

In regards to the heat transfer enhancement, the grid convergence study showed an extrapolated exact solution for the Nusselt number of approximately 8 % above the simulated solution. This should be taken into account when evaluating the exact values for the heat transfer enhancements. Furthermore, this could in fact influence the optimum as the Nusselt number discrepancy might not be exactly 8 % for all the simulated cases.

As expected, the larger winglet heights introduce a larger wake region behind the winglets which increases the pressure loss significantly. At the large winglet heights the pressure loss shows a significant dependence on the longitudinal distance, where a smaller distance causes a higher degree of turbulence in the domain. Furthermore, due to the staggered arrangement of the winglets the vortices are forced to reverse their rotational direction when interacting with the following winglet pair, which increases the pressure loss.

The highest overall heat transfer performance is shown to be at a smaller winglet height and at larger longitudinal pitch. This indicates that, despite the main longitudinal vortices being smaller in size and strength, this configuration yields a high degree of mixing between the thermal boundary layer and core flow relative to the induced pressure loss. However, the optimum configuration is dependent on the choice of performance parameter, or more specifically the practical application. In general, a significant heat transfer enhancement can be achieved at a low pressure penalty, but if a higher heat transfer is desired, it comes with a significantly higher pressure penalty. Therefore, the performance could in practice be evaluated based the savings due to enhanced heat transfer relative to the expenses due to the pressure loss.

The chosen values for the geometrical parameters also affect the final results. One important parameter is the effect of the staggered arrangement. In the present work, the effect of the staggered arrangement is an increase in turbulence due to a shift in the rotational direction of the vortices. This is due to the second winglet row being placed nearly inline of the first row but with a shift in angle of attack. The placement of the second winglet row is dependent on both the staggered offset as well as the transverse winglet pair distance. If investigations were conducted at a larger transverse distance, the transverse interaction between vortices might have a higher significance to the resulting flow characteristics.

<div align="center">

CHAPTER 6

CLOSURE

</div>

6.1 Conclusion

In this work, the impact of rectangular winglet pair vortex generators on flow phenomena, heat transfer and pressure loss in a fully developed channel flow has been investigated. The vortex generators were placed in a staggered arrangement. A Large Eddy Simulation (LES) model was developed in OpenFOAM and validated by the use of Laser Doppler Anemometry (LDA) in a wind tunnel. A meshing routine was developed in MATLAB for generating the computational grid based on geometrical parameters of the computational domain. To simulate the effect of the staggered arrangement, a single period consisting of two following winglet pairs was used as the computational domain with periodic boundary conditions deployed in the streamwise and spanwise directions.

To validate the LES setup, experiments were conducted in a developed rectangular duct made to resemble the flow in a staggered arrangement of vortex generators. Laser Doppler Anemometry (LDA) was used to measure the streamwise velocities across a period and high accuracy measurements were achieved. A spanwise velocity profile was measured in two vertical (z) positions and compared to those of the LES simulations. The LDA measurements and the LES results showed an overall good correspondence for both velocity and turbulence intensity with a mean deviation of 4.9 % and 4.6 % for the two velocity profiles. The largest deviations in the experiments were observed in regions with high turbulence intensity, where local velocity bias, caused by the spatial velocity gradient across the LDA measuring volume, was considered to be the main reason for the higher discrepancy. Due to the overall good correspondence between experimental and numerical results, the LES setup was considered to resemble the flow phenomena in the channel.

The validated LES setup was used to conduct a parametric study to investigate the influence of longitudinal pitch distance and winglet height on the flow phenomena, heat transfer enhancements and pressure losses. The heat transfer enhancement and increase in pressures were compared to a channel without vortex generators. The results yielded the existence of three distinctive vortices generated by the winglets: corner vortices, main longitudinal vortices and induced vortices. The main longitudinal vortices showed to have the the highest influence on heat transfer enhancement due to a better mixing between the thermal boundary layer and core flow. The heat transfer enhancement increased with winglet height and decreased with longitudinal pitch distance. The pressure loss showed a similar trend with an increase with winglet height and a decrease with longitudinal pitch. Furthermore, for both parameters the dependency on longitudinal pitch distance increased with winglet height. In general, heat transfer enhancements of 2.2-4.5 times the reference case were achieved with an increase in pressure loss ranging from 3.3-32.6 times the reference case.

A performance parameter, based on equal pumping power, was used to evaluate the heat transfer enhancements relative to the pressure losses. An optimum solution was found for a lower winglet height and a larger longitudinal pitch distance. This indicated that the main longitudinal vortices generated by the lower winglets, despite being smaller in size and strength, caused a good boundary layer to core flow mixing at a reasonable pressure loss. However, as the heat transfer performance depends on the choice of performance parameter, it is suggested that the practical application is taken into account when evaluating the optimum configuration.

6.2 Suggestions for further work

In the literature, numerous studies have been made where the impacts of changing the various geometrical parameters are investigated. However, as mentioned in Chapter 1, most investigations where conducted for configurations with only a single vortex generator or for vortex generators in an in-line arrangement. This was the main motivation for studying vortex generators in a staggered arrangement. This implies that several investigations of the geometrical parameters as well as of a variation in Reynolds number are needed to enlarge the current knowledge about vortex generators in staggered arrangements.

In the present work the Nusselt number is used as a measure of the heat transfer capability and a loss coefficient is used as a measure of the pressure loss. The same or similar parameters are also used in most studies involving heat transfer. However, as measure of how well the flow field interacts with the temperature field, Guo et al. (1998) proposed the so-called field synergy principle. This principle focuses on the fact that the convection heat transfer does not only depend on magnitude of the velocity vector and the temperature gradient, but also on the angle between them, where a zero degree angle proves the highest heat transfer. An implementation of this parameter into the numerical code, would therefore provide an additional measure of the performance of the heat exchanger. Furthermore, it could be beneficial to implement the ability to extract local Nusselt numbers. This could indicate better or worse heat transfer zones in the domain which should be addressed to achieve a higher performance.

The focus of this project has been on improving heat transfer in gas flows since the gas-side accounts for the main thermal resistance in heat exchangers. However, it might be useful to investigate the impact of vortex generators inserted into other media such as water. This would be immediately applicable to for example electronic devices utilising water cooling.

APPENDIX A

LITERATURE REVIEW

In this Appendix a review of existing numerical and experimental investigations of heat transfer enhancement and flow phenomena using wing- and winglet-type vortex generators (VGs) is presented. The field of investigation, methods used and main findings are extracted from the different papers and presented in tables. The most common arrangement of vortex generators in a channel is shown in Figures A.1 and A.2.
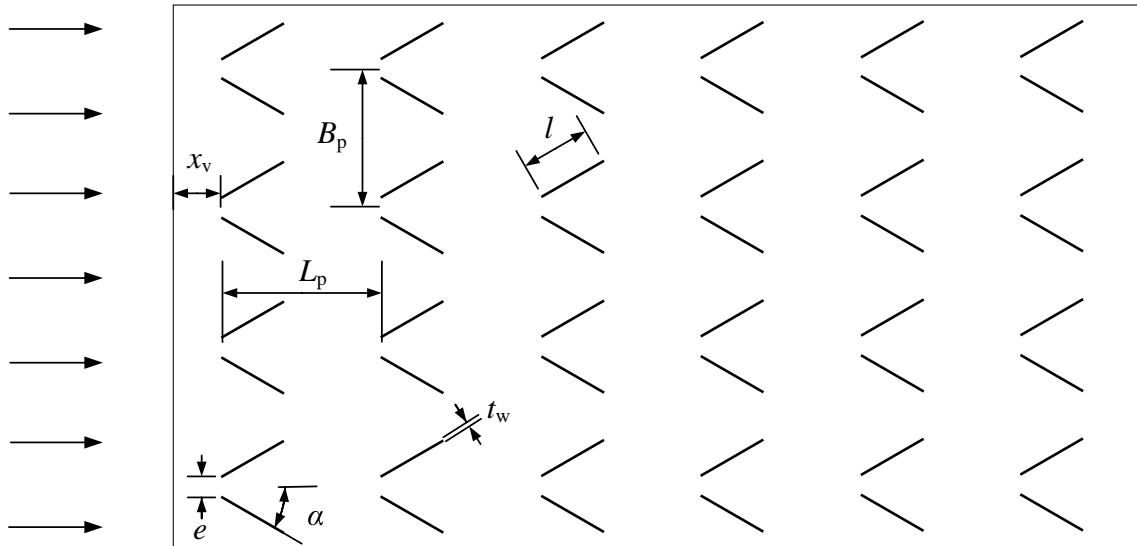

Figure A.1. Top view of a common flow down configuration of in-line rectangular winglet pairs in a channel. B_p = transverse pitch distance, e = winglet tip distance, L_p = longitudinal pitch distance, t_w = winglet thickness, x_v = distance from channel edge to winglet leading edge, l = winglet length and α = angle of attack.

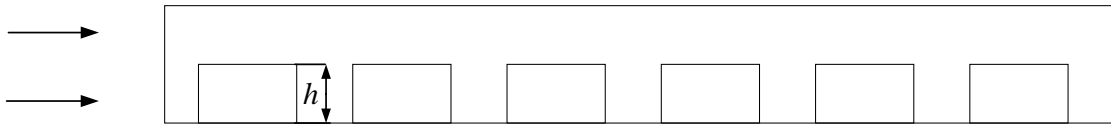Figure A.2. Side view of a common flow down configuration of in-line rectangular winglet pairs in a channel. h = winglet height.

It has to be noted that parameters such as the Re, Nu and f are calculated differently among the articles for which reason care has to be taken when comparing results across different articles. Furthermore, some parameters are article-specific and will be briefly explained below.

- Fin parameter, Fi: correlation between thermal conductivity, fin thickness and channel height given as $(k_f/k)/(\delta/H)$. k is the fluid thermal conductivity, k_f is the fin thermal conductivity, δ is the fin thickness and H is the channel height (Chen et al., 2000).
- Thermal performance parameter, JF: a measure for the amount of the heat transfer enhancement relative to the pressure loss, i.e. a correlation between Colburn J-factors and loss coefficients. The Colburn J-factor is given as $Nu/(Re\ Pr^{1/3})$ and the thermal performance factor JF is given as $(J/J^*)/(f/f^*)$, where f is the loss coefficient and $*$ denotes a reference value (Sohankar, 2007).

For more information on the different parameters, the reader is referred to the original articles which are stated in the tables below.

Field of investigation	Method	Findings	Ref.
• Experimental investigation of heat transfer enhancement by rows of delta winglets generating co- or counter-rotating vortices. • α was varied from 12.5° to 25°. • Re was kept at 61,500.	• Luminescent phosphor technique for temperature measurements.	• Heat transfer enhancement was better for higher α. • Maximum enhancement was 15 % for the co-rotating configuration and 40 % for the counter-rotating configuration. • Longitudinal vortices are long-lived and the counter-rotating delta winglet configurations proved more effective than co-rotating delta winglet configurations.	(Edwards and Alker, 1974)
• Experimental investigation of heat transfer enhancement in a plate-fin heat exchanger with staggered rectangular winglets producing counter-rotating vortices. • Punched and embossed rectangular winglets were investigated. • Re was varied between 500 and 2000.	-	• Vortices persisted well downstream of the VGs and results showed considerable heat transfer enhancement with a modest pressure loss. • Ratios of Colburn J-factor and ƒ above 0.5 in the given Re range were found.	(Russell et al., 1982)
• Experimental investigation of heat transfer enhancement of a row of counter-rotating rectangular winglet pairs on a flat plate in a laminar boundary layer. • α was kept at 20°, h was varied between 1.6 and 6.4 mm and the centre to centre spacing between pairs was varied between 19.1 and 102 mm.	• Temperature measurements were conducted using thermocouples. • Pressure and velocity measurements were conducted using Hot Wire Anemometry, pitot tubes and pressure tappings.	• The heat transfer of the undisturbed flat plate decreased faster than the disturbances generated by the VGs indicating that the velocity fluctuations persisted. • The heat transfer enhancement increased with an increasing ratio of winglet height to winglet pair spacing and with increasing ratio of winglet height to boundary layer thickness.	(Turk and Junkhan, 1986)
• Experimental investigation of the effect of longitudinal vortices on heat transfer from a flat plate in a laminar boundary layer. • Delta winglets and delta winglet pairs in common flow up, common flow down, co-rotating and counter-rotation configurations were investigated. • α was varied from 5° to 25° and h was varied from 6 mm to 25 mm, thereby increasing winglet frontal area.	• Hot Wire Anemometry was used to measure velocity and velocity fluctuations. • Thermocouples were used to determine the heat transfer coefficient.	• The main reason for heat transfer enhancement was found to be high velocity fluctuations and vortical motions indicating a transition from laminar to turbulent flow. • The common flow down pairs proved more effective than the common flow up pairs. No significant differences in heat transfer enhancement were found between the co- and counter-rotating delta winglet rows. • Heat transfer enhancement increased with increasing α and h. Furthermore, the highest heat transfer enhancement was found at minimal winglet tip spacing.	(Torii and Yanagihara, 1989)
• Experimental investigation of heat transfer enhancement on a flat plate in a turbulent boundary layer with single and rows of delta winglets and delta winglet pairs. • α was varied between 6° to 24°, h was varied between 10 mm and 30 mm and the centre to centre spacing between pairs was varied from 20 mm and 140 mm.	• Heat transfer measurements were conducted using embedded thermocouples and wire probes. • Velocities were measured using pressure probes and Hot Wire Anemometry.	• The results for the turbulent boundary layer showed similar tendencies to those with a laminar boundary layer mentioned in the earlier studies. • The maximum Stanton number enhancement was 20 %. • No significant differences were found between the co- and counter-rotating configurations which is in agreement with Torii and Yanagihara (1989) but in contrast to that found by Edwards and Alker (1974) and Russell et al. (1982).	(Eibeck and Eaton, 1985, 1986, 1987), (Pauley and Eaton, 1988, 1987, 1994), (Wroblewski and Eibeck, 1991) & (Subramanian et al., 1992)
• Numerical investigation of heat transfer enhancement using punched and mounted delta wings in a rectangular channel. • Re was varied between 500 and 1815. • α was varied between 20° and 26°. • A comparison was made at Re = 500 and α = 26°.	• Modified Marker and Cell algorithm.	• Heat transfer enhancement was evidenced and primarily due to the longitudinal vortices generated by the wing. • For the mounted wing, an increase in average Nu of 34 % and in ƒ of 79 % were found. • For the punched wing, an increase in average Nu of 10 % and in ƒ of 48 % were found.	(Biswas et al., 1989; Biswas and Chattopadhyay, 1992)

Field of investigation	Method	Findings	Ref.
• Numerical investigation of heat transfer enhancement in a developing forced convection laminar flow between flat plates with punched delta wings and delta winglet pairs.	• Modified Marker and Cell algorithm.	• The simulations showed an elliptic deformation of the counter-rotating vortices. Furthermore, the interaction with the wall produced vortex spreading leader to a larger region of boundary layer thinning and enhanced heat transfer. • Overall heat transfer enhancements of 84 % were predicted for a delta winglet pair at α = 30° and Re = 4000.	(Fiebig et al., 1989)
• Experimental investigation of flow structures and heat transfer enhancement for double rows of staggered and aligned punched delta winglet pairs in a channel flow. • Re was varied between 2000 and 8000 and α was varied between 45° and 65°.	• Heat transfer measurements were conducted with liquid-crystal thermography. • Flow visualisation was achieved using Particle Image Velocimetry.	• The development of flow structures were nearly independent of the oncoming flow of the VG. • Heat transfer enhancement increased with increasing Re. • α = 45° proved better for enhancing heat transfer. • The second row of VGs increased unsteadiness in the flow, therefore working as a booster for heat transfer enhancement. • Heat transfer enhancement of >300 % and 80 % locally and globally were found. • The optimum row spacing were 7-10 times h. • No significant disparities between the two configurations.	(Tiggelbeck et al., 1992, 1993)
• Numerical investigation of the influence of four different types of VGs on heat transfer and flow losses in turbulent channel flows. Delta wing, rectangular wing, rectangular winglet pair and delta winglet pair VGs were investigated. • Re was kept at 50,000. • α was kept at 25°.	• Modified Marker and Cell algorithm known as SOLA in combination with the k-ε turbulence model.	• The heat transfer enhancement was caused by an elevation in turbulent kinetic energy near the wall and the exchange of fluid between the near wall and core flow. • The mean heat transfer enhancement was 16-19 % with an increase in flow losses of 400-500 %. • The rectangular winglet pair and delta winglet pair proved superior of the four VG geometries.	(Zhu et al., 1993)
• Experimental investigation of heat transfer enhancement and flow losses for four different punched VGs in a channel flow. Delta wing, rectangular wing, rectangular winglet pair and delta winglet pair VGs were investigated. • Re was varied between 2000 and 8000. • α was varied between 30° and 90°.	• Heat transfer measurements were conducted with liquid-crystal thermography. • The drag were found by weighing the test configuration.	• Generally, winglets pairs performed better than wings. • The flow losses and average Nu increased monotonically with α and Re, respectively. • For the winglets, an optimum α for heat transfer enhancements lie between 45° and 65°. Global and local heat transfer enhancements of 220 % and 80 % were found, with the delta winglet pair performing slightly better.	(Tiggelbeck et al., 1994)
• Periodic numerical investigation of flow structures and heat transfer in a channel flow with a single delta winglet and delta winglet pair. • Re was kept at 1580. • α was varied between 15° and 45°. • Channel aspect ratio was varied between 3 and 5.	• Modified Marker and Cell algorithm.	• A main vortex, a corner vortex and induced vortices were found downstream of the winglet and it was evident that these lead to thinning of the velocity boundary layer. • For both channel aspect ratios, an α of 15° yielded the best results with a Colburn J-factor and f ratio of 0.95. • The single delta winglet proved better than the delta winglet pair at α = 15°.	(Biswas et al., 1994, 1996)

Field of investigation	Method	Findings	Ref.
• Numerical investigation of flow structures related to heat transfer enhancement in a channel with periodic transverse ribs and rectangular winglet pairs. • Transverse ribs generate transverse vortices and rectangular winglet pairs mainly generate longitudinal vortices. • α was kept at 45° for the rectangular winglet pairs. • Re was kept below 500. • Self-oscillatory and steady flow conditions were investigated.	• Finite volume code known as FIVO, developed by the authors.	• Longitudinal vortices are more effective than transverse vortices in steady flow because of their spiralling thermal energy transport in the streamwise direction. • Instability conditions i.e. self-sustained oscillations and turbulence are generated at lower Re by the transverse vortices compared to the longitudinal vortices. Therefore, the Reynolds averaged thermal transport is higher for transverse vortices when Re, VG area and all length ratios are the same. • At Re = 350 the heat transfer enhancement was almost the same for both configurations, but the longitudinal vortex configuration caused only half the flow losses compared to the transverse vortex configuration.	(Fiebig, 1997)
• Numerical investigation of punched delta winglets in staggered arrangements employed to enhance heat transfer in fin-oval-tube heat exchangers. • Configurations with two and four staggered delta winglets were studied and compared to three in-line delta winglets. • Re was kept at 300 and α was kept at 30°. • Fi was varied between 100 and 1000.	• Finite volume method based on (Patankar, 1980).	• The staggered arrangement of delta winglets was more effective than the in-line arrangement. • A configuration with two staggered delta winglets resulted in 20 % higher heat transfer enhancement and 14.5 % lower pressure loss compared to the in-line configuration. • At Fi = 500, two staggered delta winglets enhanced Nu by 50 % and four staggered delta winglets enhanced Nu by 87 %.	(Chen et al., 2000)
• Numerical investigation of flow phenomena and heat transfer in a channel with a mounted block like rectangular winglet pair in a common flow down configuration. • Re was varied between 400 and 1500. • α was varied between 10° and 30°. • The thickness of the VGs and distance from inlet to VGs were also investigated.	• Incompressible finite volume code based on a fractional step technique.	• Longitudinal vortices were generated downstream which enhanced heat transfer locally and globally. • At increasing Re the averaged Nu and f increased with α. • Thicker VGs form stronger and bigger streamwise vortices which gave rise to higher Nu. • Similar global results were found for thick VGs with lower α and thin VGs with higher α. • With a larger inlet to VG distance, the upstream Nu reached a lower level with a smaller peak at the beginning of the VGs.	(Sohankar and Davidson, 2001)
• Experimental investigation of the effect of varying the Reynolds number, wing aspect ratio and angle of attack of a delta wing mounted on the leading edge of a flat plate and in a channel. • α was varied between 15° and 55°. • Wing aspect ratio was varied between 0.5 and 2.0. • Re was varied between 300 and 2000.	• Heat transfer measurements were conducted using naphthalene sublimation. • Velocity was measured with an orifice plate. • Vortex strength was measured with a vane-type vortex meter and their location was visualised with ink.	• For both cases, vortex strength, convection enhancements and pressure losses increased with Re, α and wing aspect ratio. • Local convection enhancements of 300 % for the flat plate and 150 % for the channel were observed in locations where the vortex flow was toward the surface. • A maximum spatially averaged heat transfer enhancement of 55 % associated with a pressure drop of 110 % was found for the channel case.	(Gentry and Jacobi, 2002)

Field of investigation	Method	Findings	Ref.
• Experimental investigation of flow characteristics in a channel with a 4-row-4-column aligned configuration of embossed rectangular winglet pairs. • Re was varied between 1000 and 5000.	• The velocities were measured using Laser Doppler Anemometry. • Dye was used for visualisation.	• Strong longitudinal vortices were found behind each VG. • The size and strength of the vortices increased with Re. • A saturation of the vortex size and strength took place after the third row of VGs. • The turbulence development was accelerated by VGs and it was shown for Re≥2000 that the maximum turbulence level was reached after the first VG column.	(Dupont et al., 2003)
• Numerical investigation of in-line rows of punched rectangular winglet pairs and delta winglet pairs in a channel flow. • Re was varied between 2000 and 8000. • α was varied between 30° and 65°.	• Reynolds-Averaged Navier-Stokes. • Large Eddy Simulation.	• At α = 30° the VGs mainly produced longitudinal vortices and at α = 65° the VGs mainly produced transverse vortices. • The delta winglet pair proved best in terms of the compactness criterion which is a correlation between Nu and f. • Heat transfer and mixing efficiencies were found to be optimum at row distances of 7-10 times the channel height.	(Ferrouillat et al., 2006)
• Extension of Sohankar and Davidson (2001) by investigating the rectangular winglet pair for a larger Re range and using finer grids. • Re was varied between 200 and 2000. • α was varied between 10° and 30°.	• Direct Numerical Simulation. • Large Eddy Simulation.	• Nu, pressure coefficient, bulk temperature, f and Colburn J-factor changed with increasing Re and α. This was due to longitudinal vortices and horseshoe vortices with different strengths and circulation. • The vortex strength increased with Re and decayed in the streamwise direction. • JF increased with Re and JF≥1 for all cases signifying that the VGs augment heat transfer with a reasonable pressure penalty. • The levels of kinetic energy, pressure, velocity and temperature fluctuations were high in regions where the secondary flow or longitudinal vortices were more active. These regions were located around and downstream of the VGs.	(Sohankar, 2007)
• Numerical investigation of heat transfer in a rectangular channel with punched rectangular winglet pairs based on the field synergy principle. • Re was varied between 800 and 3000. • α was varied between 15° and 90°. • A parametric study of geometric sizes, shapes (delta winglet pairs) and the VGs location in the channel were also conducted.	• Commercial CFD code, FLUENT.	• α = 45° always provided better heat transfer enhancement, but the pressure drop increased with α due to increasing form drag. • The essence of heat transfer enhancement was due to an improvement in the field synergy between the velocity and temperature gradient. The longitudinal vortices improved the synergy locally and globally whereas the transverse vortices only improved the synergy locally. • The synergy angle decreased with Re. • Heat transfer enhancement decreased with increasing inlet to VG distance and decreasing rectangular winglet pair transverse spacing. • Increasing VG area increased pressure loss and heat transfer enhancement. At constant VG area, it was suggested to increase length and decrease height. • At equal VG area, delta winglet pairs proved more efficient than rectangular winglet pairs. Furthermore, a delta winglet pair with half the channel height proved more effective than a delta winglet pair with equal height to that of the channel.	(Wu and Tao, 2008b,a)

Field of investigation	Method	Findings	Ref.
• Experimental investigation of flow structures in a triangular channel with double rows of delta winglet pairs. • One configuration with both rows in common flow up and one configuration with the first row in common flow up and the second row in common flow down. The winglets were mounted on the upper sides of the channel. • Re was varied between 1000 and 8000. • α was kept at 30°.	• The flow field was visualised using Particle Image Velocimetry.	• Counter-rotating vortices were generated and these proved to be affected more by the location of the delta winglet pairs leading edge relative to the channel bottom corner rather than their configuration. • A larger vortex formation area and induced vorticity field as well as longer lasting vortices were observed for the second configuration, presumably yielding better heat transfer. • The size and strength of the vortices increased with Re.	(Akcayoglu, 2011)
• Numerical study on heat transfer enhancement in a channel using two rows of delta winglet pairs. • Five different configurations were tested: common flow up, common flow down, combined common flow down and common flow up, staggered and in-line. • Re was varied between 150 and 1580. • α was kept at 15°.	• Modified Marker and Cell algorithm.	• In terms of heat transfer enhancement, the common flow up configuration performed best followed by the common flow down and combined common flow down and common flow up. • In terms of the ratio of Colburn J-factor and f, the common flow up, common flow down and combined common flow down and common flow up showed similar performance while the staggered and in-line showed similar trends. This could be attributed to the fact that the first three configurations create counter-rotating vortices whereas the staggered and in-line create co-rotating vortices. • Overall, the common flow up configuration proved best in terms of reduction of heat exchanger depth.	(Sinha et al., 2013)
• Numerical investigation of heat transfer enhancement and flow behaviour in a channel with periodic rows of rectangular winglet pairs and delta winglet pairs. • Re was varied between 50 and 200. • α was kept at 45°. • For comparison purposes, the winglet areas and wall to winglet areas were kept equal.	• Modified Marker and Cell algorithm.	• The swirling motions generated by the VGs disrupt the thermal boundary layer, intensify mixing and bring about enhancement of heat transfer with a reasonable pressure penalty. • The rectangular winglet pair induced a higher pressure drop but had a sufficiently high heat transfer enhancement to prove superior to the delta winglet pair. • The common flow down configuration proved more beneficial than the common flow up configuration. • It was shown that locations with higher Nu were associated with smaller synergy angles.	(Saha et al., 2014)

APPENDIX B

GENERATION AND REFINEMENT OF COMPUTATIONAL MESH

In this Appendix, the process of generating the mesh used for the LES simulations is described. This comprises a description of how the MATLAB code is developed to generate the mesh followed by a description of the method used for the grid convergence study.

B.1   Mesh generation

As described in Chapter 3.2, the mesh is manually generated in MATLAB and then translated into the OpenFOAM utility called blockMesh, which is used to generate the mesh in OpenFoam (Greenshields, 2017). To utilise the blockMesh utility, the geometry is divided into a number of blocks. For each block, the following properties must be defined:

- Geometrical placement of vertices.
- Number of cells in each direction.
- Cell expansion ratio defining the ratio between the biggest and smallest cell along a direction.

For completion of the mesh, the boundary faces of the computational domain are defined. The procedure for generating the mesh in MATLAB is described in the following paragraphs.

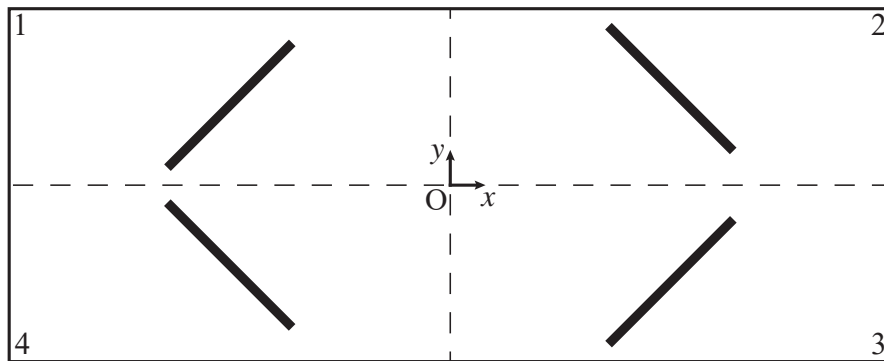The computational domain is shown in Figure 3.2.

Figure B.1. Computational domain illustrating the winglets, the quadrant numbers as well as the x- and y-planes used for mirroring.

In general, the mesh is generated by defining the different blockMesh properties in the first quadrant (upper left marked in Figure B.1). Then they are mirrored in the z-direction and then mirrored into the second, third and fourth octant. Due to the staggered arrangement of the winglets, the mirroring about the y-plane is done with a shift in the y-direction. The blocks of the first quadrant and their corresponding numbering are illustrated in Figure B.2. The blocks placed on the x- and y-mirroring-planes are computed after the mirroring.
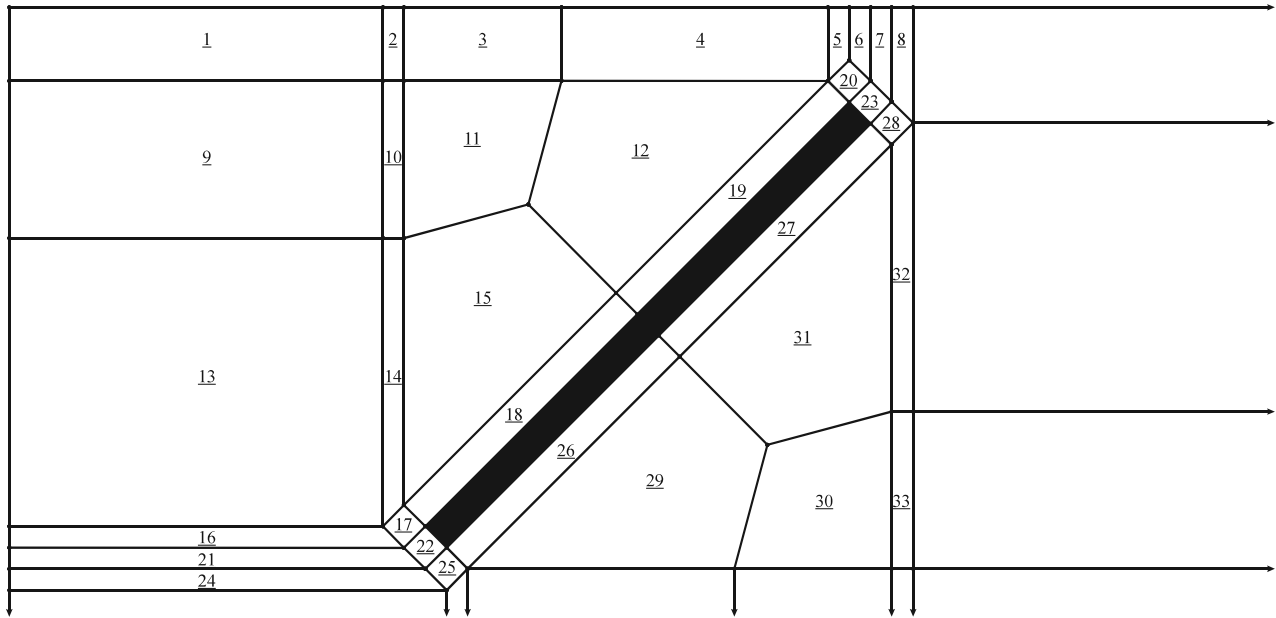

Figure B.2. Blocks of the first quadrant and their corresponding numbering. The blacked part is the winglet.

The geometrical placement of the vertices are computed from the parameters presented in Table B.1 by trigonometric relations.

Parameter	Description	Value
	Channel configuration	
H	Channel height	10 mm
L	Channel length	$62.5H$
B	Channel width	$28H$
	Winglet geometry	
α	Angle of attack	$45°$
h	Winglet height	$0.5H$
x_{v}	Distance from channel edge to winglet leading edge	$3H$
e	Winglet tip distance	$0.4H$
t_{w}	Winglet thickness	$0.1H$
l	Winglet length	$2H$
B_{p}	Transverse pitch distance	$4H$
L_{p}	Longitudinal pitch distance	$5H$
B_{o}	Staggered offset	$2H$

Table B.1. Geometrical dimensions of channel and winglets.

Beside the above-mentioned parameters a boundary layer width, BL, is specified, which dictates the width of of the blocks surrounding the winglet. When the vertices are computed in the first layer they are mirrored into the other layers of blocks from a specified distance in the z-direction. When mirroring the vertices about the y-axis the points placed on the inlet-, outlet-, and side-boundaries of the domain are not shifted in the y-direction.

This is due to the opposing boundaries being periodic and therefore the faces of the blocks must be located in the exact same points.

From the computed vertices, each block is defined by the eight vertice numbers constituting the specific block. Similar to the vertices, the blocks in the first layer are mirrored in the z-direction, including the blocks above the winglet. The blocks are then mirrored into the other octants.

For each block, the number of cells in the x-, y-, and z-direction are defined. This is done by setting a cell density which prescribes the number of cells per unit length. This parameter is then multiplied by the geometrical distance to give the total number of cells in the given direction. As the number of cells in each direction must be an integer number, the resulting number of cells is rounded to the nearest integer number. The cell density is different depending on the block. The blocks surrounding the winglets, for instance, have a higher cell density as more cells are needed to resolve the flow in the boundary layer.

The last block property is the cell expansion ratio. Two ways of defining this are possible; simple grading and edge grading. With edge grading, the expansion ratio of each edge of the blocks is defined. This allows for one block to be graded at one edge, without affecting the grading of all of the surrounding blocks. With simple grading, the grading is defined per x-, y- and z-direction, which means that any adjacent blocks must have the same grading. However, with simple grading, it is possible to divide the blocks into parts with different grading. This is an advantage if smaller cells are needed in each end of the block. Therefore, in the present work, both edge grading and simple grading are used.

Additional to the block properties, the boundaries of the domain must be specified. This is done by defining the faces constituting a boundary. Similar to the definition of blocks, the faces in the first layer in the first quadrant are defined, mirrored in the z-direction and then mirrored into the other octants.

The final result is a matrix for each of the blockMesh properties containing the information about the location of vertices, vertices constituting each block, number of cells for each block, grading for each block and faces constituting each boundary.

Also worth mentioning is, that when mirroring the properties about the x- and y-planes, the ordering of the vertices making up a definition of a block or a face must sustain certain restrictions given by the blockMesh utility. Therefore, the mirroring must be done with certain shifts in the entries of the matrices.

Finally, all of the matrices computed in MATLAB must be converted to a format which the blockMesh utility is able to read. This is done by setting up a MATLAB script that reads the matrices containing the blockMesh information and converts it into a single text-file, that is in a readable format to OpenFOAM.

B.2   Grid convergence

The grid convergence study is based on the general method proposed by Roache (1994), which is based on the use of Richardson's extrapolation. In this section, the resulting parameters presented in Table 3.5 in Chapter 3.2 are briefly described. Furthermore, the method for maintaining a constant wall adjacent cell size in the normal direction when refining the mesh is presented.

B.2.1   Grid parameters

In order to refine the grid a grid refinement ratio r is given, which is multiplied by the number of cells in each direction to increase the total number of cells. For the present study the mesh size is doubled for each mesh.

As the computational domain is three dimensional, the refinement ratio is given as:

$$r = \sqrt[3]{2}$$

Based on the change in solution when refining the mesh, the order of convergence p, can be obtained. The order of convergence is a measure of how fast the solution is converging and is given as:

$$p = \ln\left(\frac{f_3 - f_2}{f_2 - f_1}\right) / \ln(r) \tag{B.1}$$

where f_3, f_2 and f_1 are the global solution parameters for the coarse, medium and fine mesh, respectively. In the present work, these are the Nusselt number, Nu, and the loss coefficient, f. Based on the order of convergence, an estimate for the exact solution is obtained using Richardson extrapolation given as:

$$f_{h0} \cong f_1 + \frac{f_1 - f_2}{r^p - 1} \tag{B.2}$$

As a measure of how far away the computed value is from the asymptotic numerical value, a Grid Convergence Index (GCI) is used. The GCI should be close to zero, indicating that the solution is within asymptotic range. The GCI is given as:

$$GCI = \frac{F_s |\epsilon|}{r^p - 1} \tag{B.3}$$

where F_s is a factor of safety for which a value of 1.25 is recommended for comparison of three grids or more. ϵ is the relative error between the grids for which the GCI is calculated. It is then checked if the solutions are within the asymptotic range of convergence by:

$$C = \frac{GCI_{\text{coarse}}}{r^p \cdot GCI_{\text{fine}}} \tag{B.4}$$

where GCI_{coarse} is the GCI between the coarse and the medium mesh and GCI_{fine} is the GCI between the medium and fine mesh. A value of 1 indicates that the solutions are within asymptotic range of convergence.

B.2.2 Maintaining wall adjacent cell size

As it is important to keep the y^+-value in required range (1-2), the wall normal size of the first cell Δy_1 must be kept constant when refining the mesh. Due to expansion of cells G normal to the wall, an expression for the cell expansion ratio as function of refinement ratio, r, is developed. All dimensions are given in the wall normal direction. These are illustrated in Figure B.3.
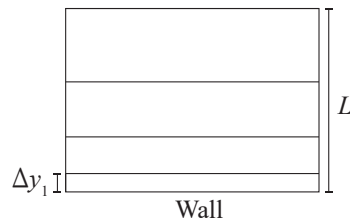

Figure B.3. Dimensions for the wall adjacent block. L is the length of the block and Δy_1 is the size of the wall adjacent cell.

Based on the length of a block, L, and the number of cells, N, an average cell size is given as:

$$<\Delta y> = \frac{L}{N} \tag{B.5}$$

From this, the size of the wall adjacent cell is given as:

$$\Delta y_1 = \frac{1}{G/2} <\Delta y> = \frac{2}{G}\frac{L}{N} \tag{B.6}$$

Replacing L/N with the inverse of the cell density $1/N_{\mathrm{cl}}$ and solving for G yields:

$$G = \frac{2}{\Delta y_1}\frac{1}{N_{\mathrm{cl}}} \tag{B.7}$$

The cell density for the i'th mesh size as function of refinement ratio, with $i = 0$ being the reference mesh and $i = 2$ being the fine mesh, is given as:

$$N_{\mathrm{cl}}(i) = r^i \cdot N_{\mathrm{cl0}} \tag{B.8}$$

where N_{cl0} is the cell density for the reference mesh. Inserting this into equation (B.7) yields an expression for the cell expansion ratio as function of the mesh size number:

$$G(i) = \frac{2}{\Delta y_1}\frac{1}{r^i \cdot N_{\mathrm{cl0}}} \tag{B.9}$$

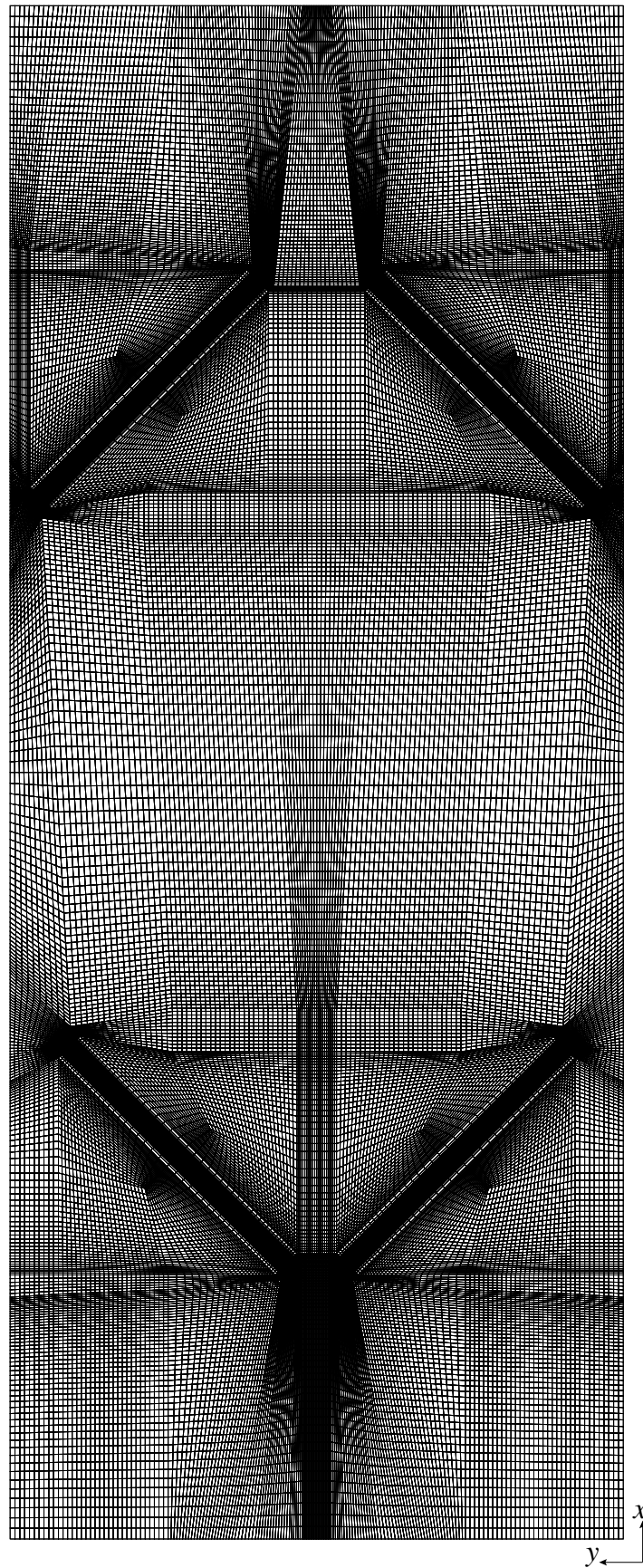The final mesh is shown in Figure B.4.

B.3 Mesh

Figure B.4. Final mesh.

APPENDIX C

PRELIMINARY EXPERIMENTS

This Appendix contains descriptions of the preliminary experiments conducted to determine the lowest possible stable velocity in the wind tunnel, a coherent set of LDA settings and to adjust the position of the laser probe measuring volume.

C.1 Determination of freestream velocity and LDA settings

The LDA system offers a wide range of settings for which reason preliminary experiments are made to find a set of settings yielding reasonable results. Furthermore, a stable freestream velocity in the wind tunnel test section is to be determined. Measurements are conducted starting from the inside of the front window and traversing further into the channel meaning that the boundary layer of the test section is measured. The measurements are conducted in *burst mode* and with a measurement interval of 30 seconds. The results are presented in Figure C.1.
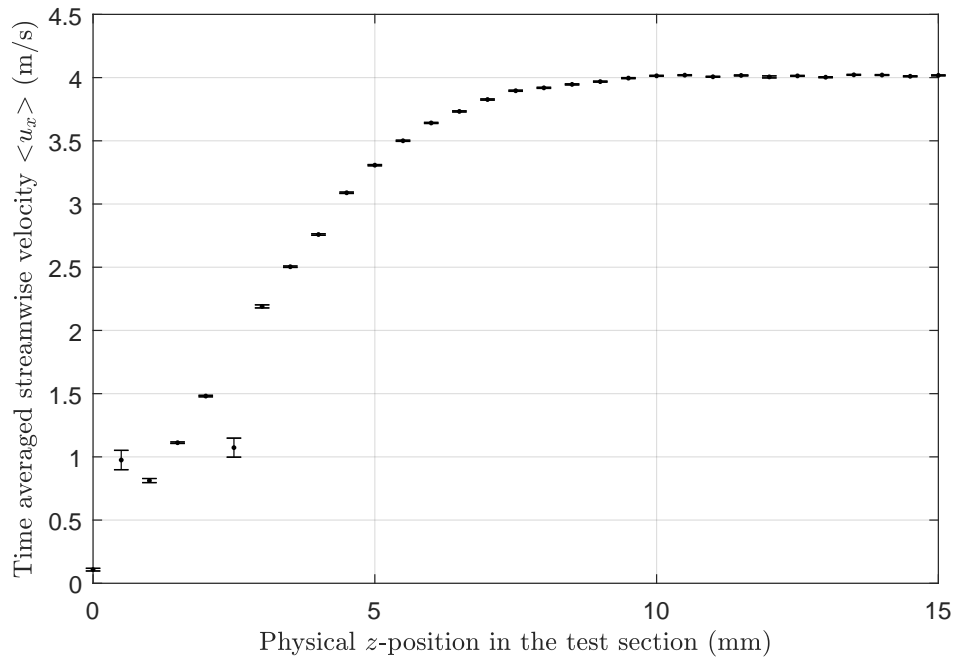

Figure C.1. Development of the time averaged streamwise velocity from the front window and 15 mm into the wind tunnel test section. The two diverging points with larger error bars are considered to be affected by noise. The error bars are based on a 95 % confidence interval.

Beside the two diverging points in Figure C.1, which are considered to be affected by noise, the development of the velocity profile into the wind tunnel test section appear reasonable keeping in mind that the flow should be laminar. The limits on the mean values are low implying a low dispersion of the velocities in each point for which reason the measurements and the associated settings presented in Table C.1 are considered reasonable for further use. During the measurements the wind tunnel was set on the lowest speed setting and according to Figure C.1 a stable free stream velocity is $\sim$4 m/s.

Settings	Value
High voltage	On, 1500 V
Signal-to-noise validation	On, -3 dB
Burst detector bandwidth	80,000 Hz
Transit time resolution	7 µs/bit
Range/Gain of velocity 1. Bandwidth 2. Frequency shift 3. Signal Gain	1. 4.00 MHz 2. 40 MHz 3. High
Laser intensity	High

Table C.1. LDA specific settings used in the experiments.

C.2 Adjustment of LDA probe position

When conducting the experiments in the test channel it is necessary to determine the location of the LDA measuring volume. The edges of the test channel are used as references when adjusting the position of the laser probe. Since it is a 2D probe, four small dots are visible behind the measuring volume as illustrated in Figure C.2.
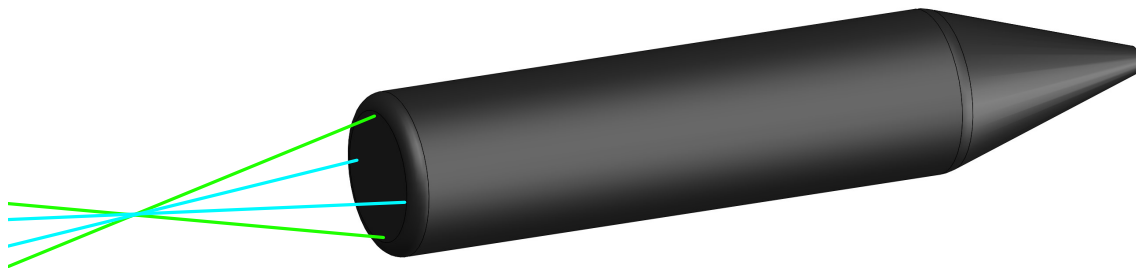

Figure C.2. Illustration of the small dot pattern behind the LDA measuring volume used to adjust the position of the LDA probe.

The green beams form a straight vertical line and the blue beams form a straight horizontal line. The green beams are aligned with the side edge of the test channel and the blue beams are aligned with the inlet edge of the channel. From these positions the probe can be moved to a desired test location based on the dimensions of the channel. Now, the position in the channel's z-direction needs to be determined. This is done by adjusting the position of the LDA measuring volume by rule of thumb and then conduct measurements by traversing through a range of z-values to determine where the velocity is 0 which should be at the wall. However, these measurements showed very high noise in both directions i.e. when traversing towards the top and bottom panel, yielding no clear results and thereby rendering the measurements unusable. This is also the case for the side panels and inlet which is why the probe positions in the x- and y-direction are adjusted as mentioned above. The noise is most likely due to reflections for which reason a small part of the bottom panel is painted black as seen in Figure C.3.
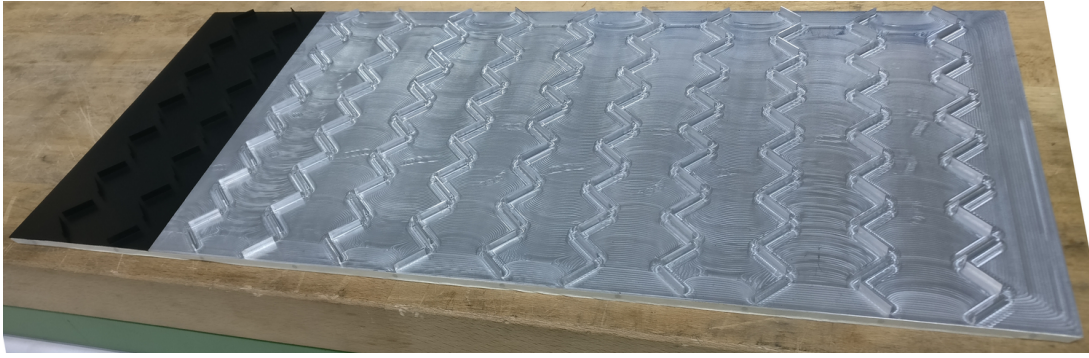
Figure C.3. The bottom panel of the test channel with a small part painted black to decrease noise.

Measurements traversing in the z-direction are conducted in the painted part of the test channel and it shows a lower level of noise which enables the determination of the z-position. The final results from the measurements are shown in Figure C.4.
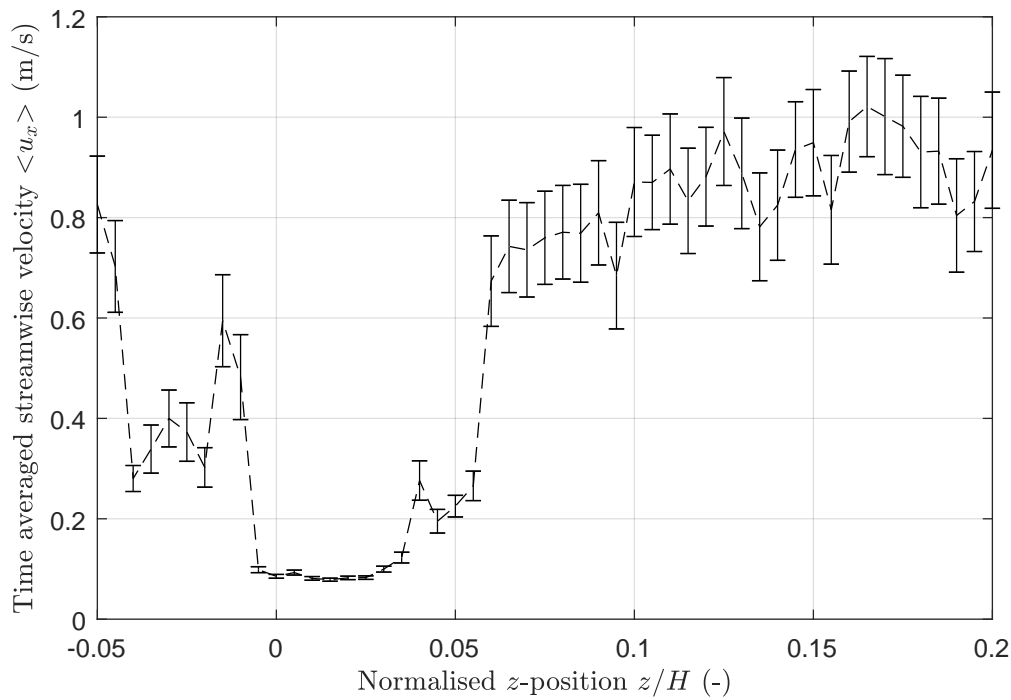

Figure C.4. Time averaged streamwise velocity as function of normalised z-position. The error bars are based on a 95 % confidence interval.

The velocity approaches zero as $z/H \to 0$. The dimensions of the LDA measuring volume are 0.076 mm in diameter and 0.64 mm in length (Dantec Measurement Technology, 1994). It means that at some point the measuring volume is forced into the wall of the bottom panel which is expected to induce a significant amount of noise as stated by Romano (1992). This is evident from the $z/H < 0$ part of Figure C.4 where it seems that the velocity rises again after $<u_x> \to 0$ for $z/H \to 0$. This is considered to be noise due to more and more of measuring volume being moved into the wall. This is backed up by the fact that the probe currents rise significantly as the measuring volume is approaching the wall, because the solid wall scatters significantly more light than the particles. Therefore, the wall is considered to be in the range of $0 \leq z/H \leq 0.03$. This means that the reference z-coordinate is within 6 % of the actual mid point of the channel which is considered reasonable. Furthermore, the remaining part of the channel is painted black.

Appendix D

Simulation Properties from Parametric Study

#	h/H	L_p	Cells (mil)	Period time (s)	Time to periodic (s)	Simulation time (s)	Nu/Nu$_0$	f/f_0	η
1	0.3	3	1.65	0.057	0.342	0.626	2.473	5.044	1.442
2	0.3	4	1.97	0.076	0.456	0.835	2.451	4.528	1.482
3	0.3	5	2.22	0.095	0.570	1.044	2.421	4.086	1.514
4	0.3	6	2.57	0.114	0.683	1.253	2.361	3.708	1.526
5	0.3	7	2.9	0.133	0.797	1.462	2.241	3.367	1.495
6	0.4	3	1.63	0.057	0.342	0.626	3.022	8.504	1.481
7	0.4	4	1.96	0.076	0.456	0.835	2.909	7.333	1.497
8	0.4	5	2.21	0.095	0.570	1.044	2.849	6.425	1.532
9	0.4	6	2.56	0.114	0.683	1.253	2.759	5.646	1.549
10	0.4	7	2.89	0.133	0.797	1.462	2.665	5.048	1.553
11	0.5	3	1.62	0.057	0.342	0.626	3.543	13.896	1.474
12	0.5	4	1.95	0.076	0.456	0.835	3.354	11.321	1.494
13	0.5	5	2.2	0.095	0.570	1.044	3.173	9.550	1.495
14	0.5	6	2.55	0.114	0.683	1.253	3.042	8.203	1.508
15	0.5	7	2.88	0.133	0.797	1.462	2.894	7.246	1.496
16	0.6	3	1.61	0.057	0.342	0.626	4.142	22.770	1.461
17	0.6	4	1.94	0.076	0.456	0.835	3.842	17.263	1.487
18	0.6	5	2.19	0.095	0.570	1.044	3.523	14.117	1.458
19	0.6	6	2.54	0.114	0.683	1.253	3.381	11.911	1.480
20	0.6	7	2.87	0.133	0.797	1.462	3.261	10.465	1.491
21	0.7	3	1.6	0.057	0.342	0.626	4.481	32.973	1.397
22	0.7	4	1.93	0.076	0.456	0.835	4.236	25.441	1.440
23	0.7	5	2.18	0.095	0.570	1.044	3.903	20.680	1.422
24	0.7	6	2.53	0.114	0.683	1.253	3.692	17.611	1.419
25	0.7	7	2.86	0.133	0.797	1.462	3.580	15.341	1.441

Table D.1. Simulation properties for parametric study showing (by column) simulation number, normalised winglet height, normalised longitudinal pitch distance, number of cells, time for a single flow through, time until the flow is periodic, total simulation time, Nusselt number enhancement, increase in loss coefficient and performance factor.

APPENDIX E

OPENFOAM HEAT TRANSFER CODE

```
1   {
2   volScalarField alphaEff("alphaEff",turbulence->nu()/Pr + turbulence->nut()/Prt);
3
4   fvScalarMatrix TEqn
5   (
6   fvm::ddt(T)
7   + fvm::div(phi, T)
8   - fvm::laplacian(alphaEff, T)
9   + U.component(0)*gamma
10  );
11
12  TEqn.solve();
13  }
```

```
1   label wallsID = mesh.boundaryMesh().findPatchID("walls");
2   label inletID = mesh.boundaryMesh().findPatchID("inlet");
3
4   dimensionedScalar num
5   (
6       "num",
7       dimensionSet(0, 2, -1, 1, 0, 0, 0),
8
9       gSum(T.boundaryField()[inletID]*U.boundaryField()[inletID].component(0)*mesh.magSf
        ().boundaryField()[inletID])
10  );
11
12  dimensionedScalar den
13  (
14      "den",
15      dimensionSet(0, 2, -1, 0, 0, 0, 0),
16
17      gSum(U.boundaryField()[inletID].component(0)*mesh.magSf().boundaryField()[inletID]
        )
18  );
19
20  dimensionedScalar Tbulk
21  (
22      num/den
23  );
24
25  dimensionedScalar dTdn
26  (
27      "dTdn",
28      dimensionSet(0, -1, 0, 1, 0, 0, 0),
29
30      gSum(T.boundaryField()[wallsID].snGrad()*mesh.magSf().boundaryField()[wallsID])/gS
        um(mesh.magSf().boundaryField()[wallsID])
31  );
32
    Nu = dTdn*H/(Twall-Tbulk);

    Info << "Nu = " << Nu.value() << endl;
```

APPENDIX F

STREAMLINE CONTOURS IN LARGE FORMAT

$x/L_d = -0.50$

$x/L_d = -0.40$
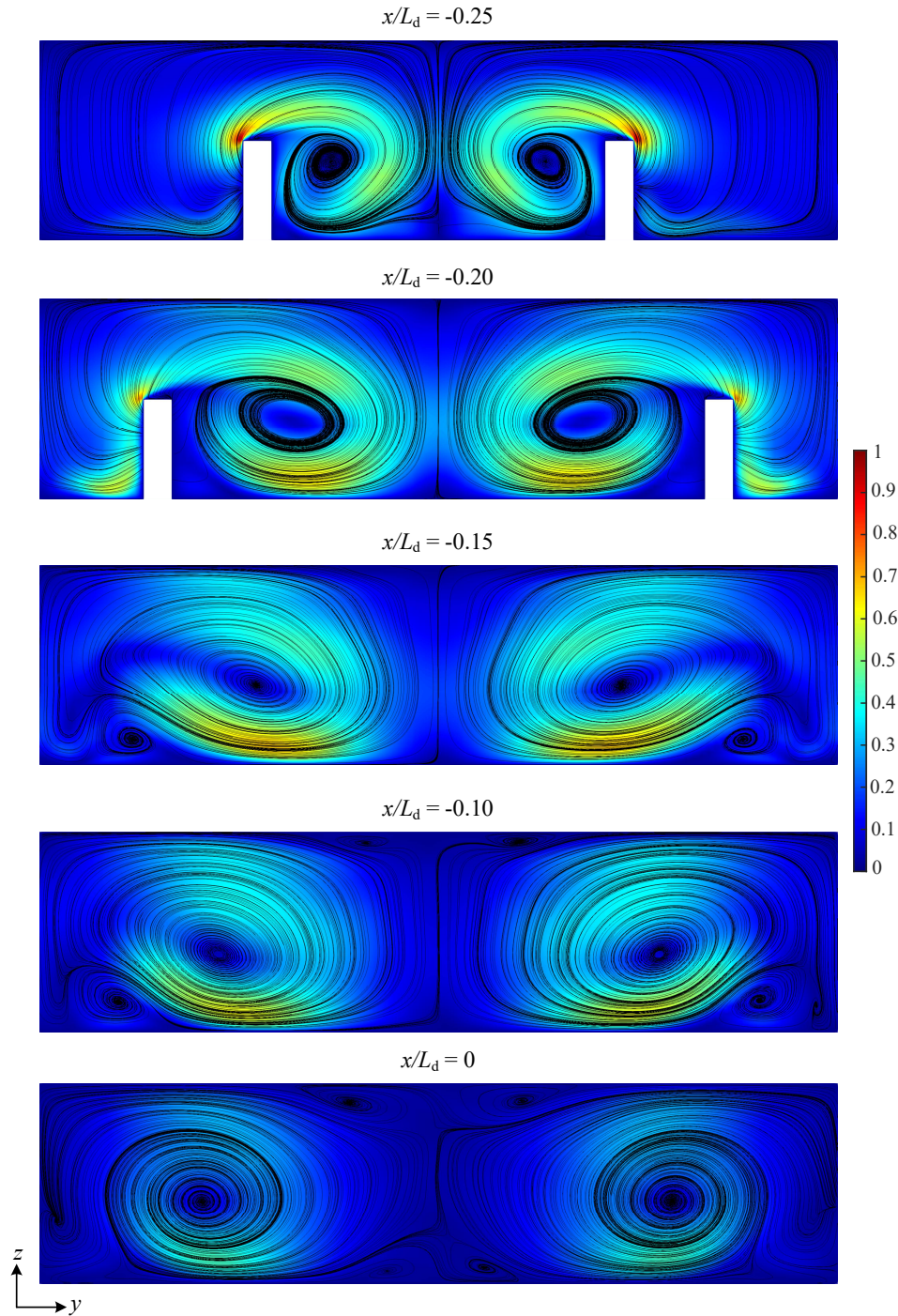
$x/L_d = -0.35$

$x/L_d = -0.30$
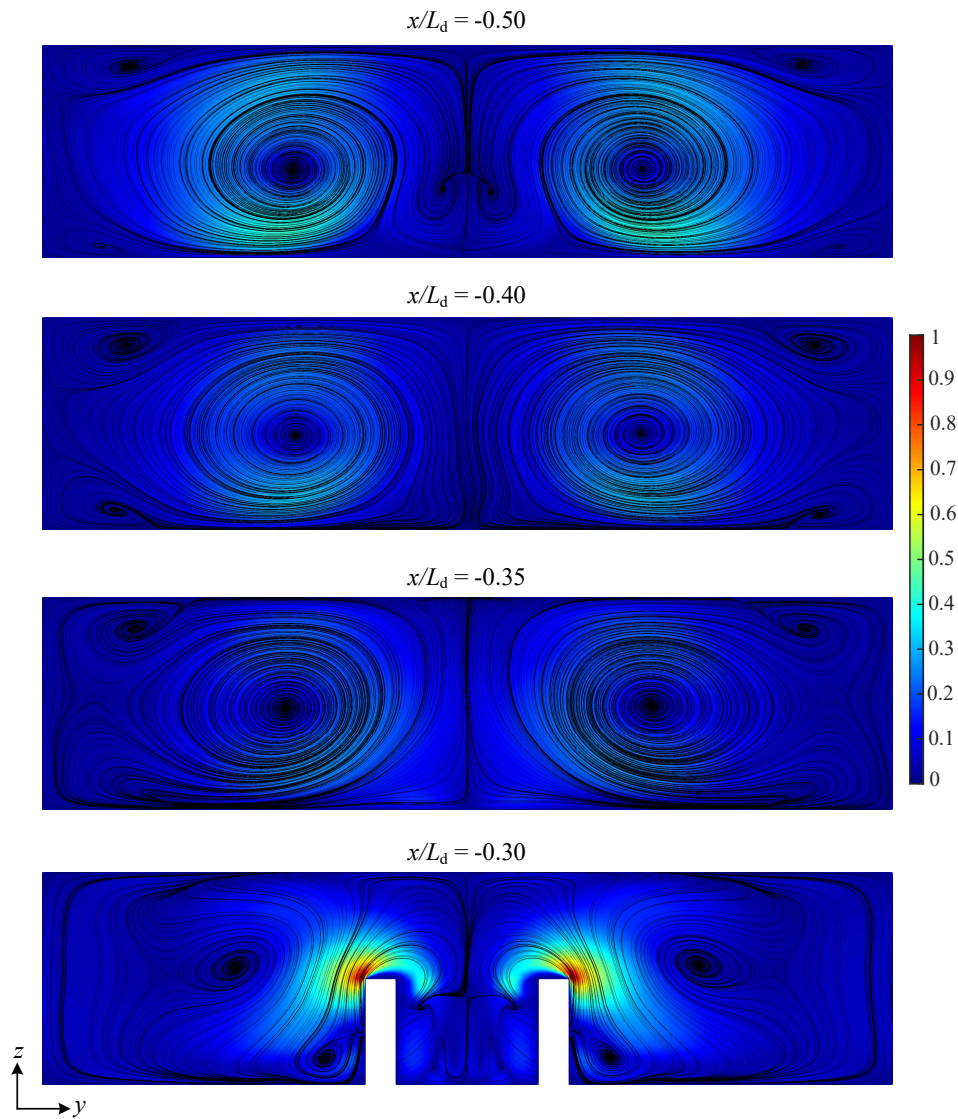
Figure F.1. Normalised time averaged y-z velocity streamlines showing the development of the flow going from the inlet of the domain down to the middle of the domain. The domain configuration is with a normalised winglet height of $z/H = 0.5$ and a normalised longitudinal pitch distance of $L_p/H = 5$. The cross sections are coloured with the magnitude of the normalised time averaged y-z velocities. The normalisation is made relative to the maximum value in the domain as $<|u_y+u_z|>/\max<|u_y+u_z|>$.

References

D. Admiraal and C. Bullard. Experimental Validation of Heat Exchanger Models for Refrigerator/Freezers. In *American Society of Heating, Refrigerating and Air-Conditioning Engineers (ASHRAE) Transactions*, volume 101, pages 34–44, 1995.

R. J. Adrian, K. T. Christensen, and Z.-C. Liu. Analysis and interpretation of instantaneous turbulent velocity fields. *Experiments in Fluids*, 29(3):275–290, 2000. ISSN 1432-1114. doi: 10.1007/s003489900087.

A. Akcayoglu. Flow past confined delta-wing type vortex generators. *Experimental Thermal and Fluid Science*, 35(1):112–120, 2011. ISSN 0894-1777. doi: 10.1016/j.expthermflusci.2010.08.012.

T. Alam and M.-H. Kim. A comprehensive review on single phase heat transfer enhancement techniques in heat exchanger applications. *Renewable and Sustainable Energy Reviews*, 81(1):813 – 839, 2018. ISSN 1364-0321. doi: 10.1016/j.rser.2017.08.060.

I. ANSYS. *ANSYS Fluent Theory Guide*, 2018.

M. Awais and A. A. Bhuiyan. Heat transfer enhancement using different types of vortex generators (VGs): A review on experimental and numerical activities. *Thermal Science and Engineering Progress*, 5:524–545, 2018. ISSN 2451-9049. doi: 10.1016/j.tsep.2018.02.007.

G. Biswas and H. Chattopadhyay. Heat transfer in a channel with built-in wing-type vortex generators. *International Journal of Heat and Mass Transfer*, 35(4):803–814, 1992. ISSN 0017-9310. doi: 10.1016/0017-9310(92)90248-Q.

G. Biswas, N. K. Mitra, and M. Fiebig. Computation of Laminar Mixed Convection Flow in a Channel with Wing Type Built-in Obstacles. *Journal of Thermophysics and Heat Transfer*, 3(4):447–453, 1989. doi: 10.2514/3.28769.

G. Biswas, P. Deb, and S. Biswas. Generation of Longitudinal Streamwise Vortices–A Device for Improving Heat Exchanger Design. *Journal of Heat Transfer*, 116(3):588–597, 1994. ISSN 0022-1481. doi: 10.1115/1.2910910.

G. Biswas, K. Torii, D. Fujii, and K. Nishino. Numerical and experimental determination of flow structure and heat transfer effects of longitudinal vortices in a channel flow. *International Journal of Heat and Mass Transfer*, 39(16):3441–3451, 1996. ISSN 0017-9310. doi: 10.1016/0017-9310(95)00398-3.

Y. A. Cengel, J. M. Cimbala, R. H. Turner, and M. Kanoglu. *Fundamentals of Thermal-Fluid Sciences*. McGraw-Hill, 4 edition, 2012. ISBN 978-007-132511-0.

Y. Chen, M. Fiebig, and N. Mitra. Heat transfer enhancement of finned oval tubes with staggered punched longitudinal vortex generators. *International Journal of Heat and Mass Transfer*, 43(3):417–435, 2000. ISSN 0017-9310. doi: 10.1016/S0017-9310(99)00157-X.

Dantec Measurement Technology. *FiberFlow Installation & User's guide*. Dantec Measurement Technology, 1994.

Dantec Measurement Technology. *BSA/FVA Flow Software: Installation & User's Guide*. Dantec Measurement Technology, Tonsbakken 18, DK-2740 Skovlunde, Denmark, 4th edition, 2000.

M. Dues and F. Neuer. Laser Doppler Velocimetry - Laser Optical Measurements Applications for Fluids, 2016. Lecture notes from Summer School "Flow Measurement Methods", Technische Universität Berlin, October 2016.

F. Dupont, C. Gabillet, and P. Bot. Experimental Study of the Flow in a Compact Heat Exchanger Channel With Embossed-Type Vortex Generators. *Journal of Fluids Engineering*, 125(4):701–709, 2003. ISSN 0098-2202. doi: 10.1115/1.1595675.

F. Edwards and G. Alker. The Improvement of Forced Convection Surface Heat Transfer Using Surface Protrusions in the Form of (A) Cubes and (B) Vortex Generators. In *Proceedings of the Fifth International Heat Transfer Conference in Tokyo*, volume 2, pages 2244–2248, 1974.

P. Eibeck and J. Eaton. An experimental investigation of the heat-transfer effects of a longitudinal vortex embedded in a turbulent boundary layer. *Report MD-48, Thermosciences Division, Department of Mechanical Engineering, Stanford University*, 1985.

P. Eibeck and J. Eaton. The effects of longitudinal vortices embedded in a turbulent boundary layer on momentum and thermal transport. In *Proceedings of the Eighth International Heat Transfer Conference in San Fransisco*, volume 3, pages 1115–1120, 1986.

P. A. Eibeck and J. K. Eaton. Heat Transfer Effects of a Longitudinal Vortex Embedded in a Turbulent Boundary Layer. *Journal of Heat Transfer*, 109(1):16–24, 1987. ISSN 0022-1481. doi: 10.1115/1.3248039.

ERCOFTAC. *Best Practice Guidelines*. European Research Community On Flow, Turbulence And Combustion, 2000. Ed. Michael Casey and Torsten Wintergerste.

A. Esmaeilzadeh, N. Amanifard, and H. Deylami. Comparison of simple and curved trapezoidal longitudinal vortex generators for optimum flow characteristics and heat transfer augmentation in a heat exchanger. *Applied Thermal Engineering*, 125:1414 – 1425, 2017. ISSN 1359-4311. doi: 10.1016/j.applthermaleng.2017.07.115.

S. Ferrouillat, P. Tochon, C. Garnier, and H. Peerhossaini. Intensification of heat-transfer and mixing in multifunctional heat exchangers by artificially generated streamwise vorticity. *Applied Thermal Engineering*, 26(16):1820–1829, 2006. ISSN 1359-4311. doi: 10.1016/j.applthermaleng.2006.02.002.

M. Fiebig. Vortices and Heat Transfer. *Journal of Applied Mathematics and Mechanics*, 77(1):3–18, 1997. doi: 10.1002/zamm.19970770103.

M. Fiebig. Vortices, Generators and Heat Transfer. *Chemical Engineering Research and Design*, 76(2): 108–123, 1998. ISSN 0263-8762. doi: 10.1205/026387698524686. 5th UK National Heat Transfer Conference.

M. Fiebig, U. Brockmeier, N. K. Mitra, and T. Güntermann. Structure of velocity and temperature fields in laminar channel flows with longitudinal vortex generators. *Numerical Heat Transfer, Part A: Applications*, 15(3):281–302, 1989. doi: 10.1080/10407788908944689.

M. C. Gentry and A. M. Jacobi. Heat Transfer Enhancement by Delta-Wing-Generated Tip Vortices in Flat-Plate and Developing Channel Flows. *Journal of Heat Transfer*, 124(6):1158–1168, 2002. ISSN 0022-1481. doi: 10.1115/1.1513578.

C. Greated, J. Cosgrove, and J. Buick. *Optical Methods for Data Processing in Heat and Fluid Flow*. Professional Engineering Publishing, 1st edition, 2002. ISBN 1-86058-281-8.

C. J. Greenshields. *OpenFOAM userguide v. 5.0*. OpenFOAM Foundation Ltd., 2017. Ed. CFD Direct Ltd.

Z. Y. Guo, D. Y. Li, and B. X. Wang. A novel concept for convective heat transfer enhancement. *International Journal of Heat and Mass Transfer*, 41(14):2221–2225, 1998. ISSN 0017-9310. doi: 10.1016/S0017-9310(97)00272-X.

J. Hærvig. cyclicTemperatureFoam - An OpenFOAM solver for cyclic heat transfer., 2018. GitHub repository. doi: 10.5281/zenodo.1254574.

A. Jacobi and R. Shah. Heat transfer surface enhancement through the use of longitudinal vortices: A review of recent progress. *Experimental Thermal and Fluid Science*, 11(3):295–309, 1995. ISSN 0894-1777. doi: 10.1016/0894-1777(95)00066-U.

A. M. Jacobi and R. K. Shah. Air-Side Flow and Heat Transfer in Compact Heat Exchangers: A Discussion of Enhancement Mechanisms. *Heat Transfer Engineering*, 19(4):29–41, 1998. doi: https://doi.org/10.1080/01457639808939934.

A. S. Jebakumar, K. N. Premnath, and J. Abraham. Lattice Boltzmann method simulations of Stokes number effects on particle trajectories in a wall-bounded flow. *Computers & Fluids*, 124:208–219, 2016. ISSN 0045-7930. doi: 10.1016/j.compfluid.2015.07.020. Special Issue for ICMMES-2014.

K. D. Jensen. Flow measurements. *Journal of the Brazilian Society of Mechanical Sciences and Engineering*, 26(4):400–419, 2004. ISSN 1678-5878. doi: 10.1590/S1678-58782004000400006.

A. Melling. Tracer particles and seeding for particle image velocimetry. *Measurement Science and Technology*, 8(12):1406–1416, 1997. doi: 10.1088/0957-0233/8/12/005.

E. E. Michaelides, C. T. Crowe, and J. D. Schwarzkopf. *Multiphase Flow Handbook*. Taylor & Francis, CRC Press, 2nd edition, 2016. ISBN 978-1498701006.

M. Mirzaei, A. Sohankar, L. Davidson, and F. Innings. Large Eddy Simulation of the flow and heat transfer in a half-corrugated channel with various wave amplitudes. *International Journal of Heat and Mass Transfer*, 76:432–446, 2014. ISSN 0017-9310. doi: 10.1016/j.ijheatmasstransfer.2014.04.018.

F. Nicoud and F. Ducros. Subgrid-scale stress modelling based on the square of the velocity gradient tensor. *Flow, Turbulence and Combustion*, 62(3):183–200, 1999. doi: 10.1023/A:1009995426001.

J. Novotný and L. Manoch. The Criterion of Choosing the Proper Seeding Particles. In *Engineering Mechanics 2012 Conference Proceedings*, pages 945–954, 2012. Ed. J. Náprstek and C. Fischer.

S. V. Patankar. *Numerical Heat Transfer and Fluid Flow*. Hemisphere Publishing Corporation, 1980. ISBN 0891165223.

S. V. Patankar, C. H. Liu, and E. M. Sparrow. Fully Developed Flow and Heat Transfer in Ducts Having Streamwise-Periodic Variations of Cross-Sectional Area. *Journal of Heat Transfer*, 99(2):180–186, 1977. ISSN 0022-1481. doi: 10.1115/1.3450666.

W. R. Pauley and J. K. Eaton. Experimental study of the development of longitudinal vortex pairs embedded in a turbulent boundary layer. *AIAA Journal*, 26(7):816–823, 1987. doi: 10.2514/3.9974.

W. R. Pauley and J. K. Eaton. *Fluid Dynamics and Heat Transfer Effects of Streamwise Vortices Embedded in a Turbulent Boundary Layer*. UMI, 1988.

W. R. Pauley and J. K. Eaton. The Effect of Embedded Longitudinal Vortex Arrays on Turbulent Boundary Layer Heat Transfer. *Journal of Heat Transfer*, 116(4):871–879, 1994. ISSN 0022-1481. doi: 10.1115/1.2911461.

S. B. Pope. *Turbulent Flows*. Cambridge University Press, 1st edition, 2000. ISBN 978-0-521-59886-6.

M. Quadrio and P. Luchini. Integral space–time scales in turbulent wall flows. *Physics of Fluids*, 15(8): 2219–2227, 2003. doi: 10.1063/1.1586273.

M. Raffel, C. E. Willert, S. T. Wereley, and J. Kompenhans. *Particle Image Velociemtry - A Practical Guide*. Springer Berlin Heidelberg New York, 2nd edition, 2007. ISBN 978-3-540-72307-3.

P. J. Roache. Perspective: A Method for Uniform Reporting of Grid Refinement Studies. *Journal of Fluids Engineering*, 116(3):405–413, 1994. ISSN 0098-2202. doi: 10.1115/1.2910291.

G. Romano. PIV and LDA velocity measurements near walls and in the wake of a delta wing. *Optics and Lasers in Engineering*, 16(4):293–309, 1992. ISSN 0143-8166. doi: 10.1016/0143-8166(92)90094-N.

C. M. B. Russell, T. V. Jones, and G. H. Lee. Heat transfer enhancement using vortex generators. In *Proceedings of the Seventh International Heat Transfer Conference*, volume 3, pages 283–288, 1982.

P. Saha, G. Biswas, and S. Sarkar. Comparison of winglet-type vortex generators periodically deployed in a plate-fin heat exchanger – A synergy based analysis. *International Journal of Heat and Mass Transfer*, 74: 292–305, 2014. ISSN 0017-9310. doi: 10.1016/j.ijheatmasstransfer.2014.03.015.

A. Sinha, K. A. Raman, H. Chattopadhyay, and G. Biswas. Effects of different orientations of winglet arrays on the performance of plate-fin heat exchangers. *International Journal of Heat and Mass Transfer*, 57(1): 202–214, 2013. ISSN 0017-9310. doi: 10.1016/j.ijheatmasstransfer.2012.10.034.

A. Sohankar. Heat transfer augmentation in a rectangular channel with a vee-shaped vortex generator. *International Journal of Heat and Fluid Flow*, 28(2):306–317, 2007. ISSN 0142-727X. doi: 10.1016/j.ijheatfluidflow.2006.03.002.

A. Sohankar and L. Davidson. Effect of inclined vortex generators on heat transfer enhancement in a three-dimensional channel. *Numerical Heat Transfer, Part A: Applications*, 39(5):433–448, 2001. doi: https://doi.org/10.1080/10407780121572.

C. S. Subramanian, P. M. Ligrani, and M. F. Tuzzolo. Surface heat transfer and flow properties of vortex arrays induced artificially and from centrifugal instabilities. *International Journal of Heat and Fluid Flow*, 13(3):210–223, 1992. ISSN 0142-727X. doi: 10.1016/0142-727X(92)90034-7.

S. Tiggelbeck, N. Mitra, and M. Fiebig. Flow structure and heat transfer in a channel with multiple longitudinal vortex generators. *Experimental Thermal and Fluid Science*, 5(4):425–436, 1992. ISSN 0894-1777. doi: 10.1016/0894-1777(92)90029-5.

S. Tiggelbeck, N. Mitra, and M. Fiebig. Experimental investigations of heat transfer enhancement and flow losses in a channel with double rows of longitudinal vortex generators. *International Journal of Heat and Mass Transfer*, 36(9):2327–2337, 1993. ISSN 0017-9310. doi: 10.1016/S0017-9310(05)80117-6.

S. Tiggelbeck, N. K. Mitra, and M. Fiebig. Comparison of Wing-Type Vortex Generators for Heat Transfer Enhancement in Channel Flows. *Journal of Heat Transfer*, 116(4):880–885, 1994. ISSN 0022-1481. doi: 10.1115/1.2911462.

K. Torii and J. Yanagihara. The Effects of Longitudinal Vortices on Heat Transfer of Laminar Boundary Layers. *JSME international journal*, 32(3):395–402, 1989. doi: 10.1299/jsmeb1988.32.3_395.

A. Y. Turk and G. H. Junkhan. Heat transfer enhancement downstream of vortex generators on a flat plate. In *Proceedings of the Eighth International Heat Transfer Conference*, volume 6, pages 2903–2908, 1986.

H. K. Versteeg and W. Malalasekera. *An Introduction to Computational Fluid Dynamics: The Finite Volume Method*. Pearson Education Limited, 2nd edition, 2007. ISBN 978-0131274983.

S. Vestøl, W. A. S. Kumara, and M. C. Melaaen. Particle Image Velocimetry Measurements of Stratified Gas-Liquid Flow in Horizontal and Inclined Pipes. *International Journal of Computational Methods and Experimental Measurements*, 6(2):411–422, 2018. doi: 10.2495/CMEM-V6-N2-411-422.

E. D. Villiers. *The Potential of Large Eddy Simulation for the Modeling of Wall Bounded Flows*. PhD thesis, Department of Mechanical Engineering, Imperial College London, 2006.

R. E. Walpole, R. H. Myers, S. L. Myers, and K. Ye. *Probability and Statistics for Engineers and Scientists*. Pearson Education Limited, 9th edition, 2014. ISBN 978-1292023922.

R. L. Webb and E. R. G. Eckert. Application of rough surfaces to heat exchanger design. *International Journal of Heat and Mass Transfer*, 15(9):1647–1658, 1972. ISSN 0017-9310. doi: 10.1016/0017-9310(72)90095-6.

D. E. Wroblewski and P. A. Eibeck. Measurements of turbulent heat transport in a boundary layer with an embedded streamwise vortex. *International Journal of Heat and Mass Transfer*, 34(7):1617–1631, 1991. ISSN 0017-9310. doi: 10.1016/0017-9310(91)90141-Z.

J. M. Wu and W. Q. Tao. Numerical study on laminar convection heat transfer in a rectangular channel with longitudinal vortex generator. Part A: Verification of field synergy principle. *International Journal of Heat and Mass Transfer*, 51(5):1179–1191, 2008a. ISSN 0017-9310. doi: 10.1016/j.ijheatmasstransfer.2007.03.032.

J. M. Wu and W. Q. Tao. Numerical study on laminar convection heat transfer in a channel with longitudinal vortex generator. Part B: Parametric study of major influence factors. *International Journal of Heat and Mass Transfer*, 51(13):3683–3692, 2008b. ISSN 0017-9310. doi: 10.1016/j.ijheatmasstransfer.2007.03.031.

Z. Zhang. *LDA Application Methods: Laser Doppler Anemometry for Fluid Dynamics*. Springer-Verlag Berlin Heidelberg, 2010. ISBN 978-3642135132. Ed. Wolfgang Merzkirch and Donald Rockwell and Cameron Tropea.

J. X. Zhu, N. K. Mitra, and M. Fiebig. Effects of longitudinal vortex generators on heat transfer and flow loss in turbulent channel flows. *International Journal of Heat and Mass Transfer*, 36(9):2339–2347, 1993. ISSN 0017-9310. doi: 10.1016/S0017-9310(05)80118-8.